NANOMECHANICAL CHARACTERIZATION OF MATERIALS BY ENHANCED HIGHER HARMONICS OF A TAPPING CANTILEVER

A DISSERTATION SUBMITTED TO
THE DEPARTMENT OF ELECTRICAL AND ELECTRONICS ENGINEERING
AND THE INSTITUTE OF ENGINEERING AND SCIENCE
OF BILKENT UNIVERSITY
IN PARTIAL FULFILLMENT OF THE REQUIREMENTS
FOR THE DEGREE OF
DOCTOR OF PHILOSOPHY

By
Müjdat Balantekin
May, 2005

I certify that I have read this thesis and that in my opinion it is fully adequate, in scope and in quality, as a dissertation for the degree of doctor of philosophy.

Prof. Dr. Abdullah Atalar (Supervisor)

I certify that I have read this thesis and that in my opinion it is fully adequate, in scope and in quality, as a dissertation for the degree of doctor of philosophy.

Prof. Dr. Hayrettin Köymen

I certify that I have read this thesis and that in my opinion it is fully adequate, in scope and in quality, as a dissertation for the degree of doctor of philosophy.

Prof. Dr. Ekmel Özbay

I certify that I have read this thesis and that in my opinion it is fully adequate, in scope and in quality, as a dissertation for the degree of doctor of philosophy.

Prof. Dr. Yusuf Ziya İder

I certify that I have read this thesis and that in my opinion it is fully adequate, in scope and in quality, as a dissertation for the degree of doctor of philosophy.

Prof. Dr. Tayfun Akın

Approved for the Institute of Engineering and Science:

Prof. Dr. Mehmet B. Baray
Director of the Institute

ABSTRACT

NANOMECHANICAL CHARACTERIZATION OF MATERIALS BY ENHANCED HIGHER HARMONICS OF A TAPPING CANTILEVER

Müjdat Balantekin
Ph.D. in Electrical and Electronics Engineering
Supervisor: Prof. Dr. Abdullah Atalar
May, 2005

In a tapping-mode atomic force microscope, the periodic interaction of the tip with the sample surface creates a tip-sample interaction force, and the pure sinusoidal motion of the cantilever is disturbed. Hence, the frequency spectrum of the oscillating cantilever contains higher harmonics at integer multiples of the excitation frequency. In this thesis, we utilize one of the higher harmonics of a vibrating cantilever to investigate the material properties at the nanoscale. We show analytically that the amplitudes of the higher harmonics increase monotonically for a range of sample stiffness, if the interaction is dominated by elastic force. We propose a method in which the cantilever is excited at a submultiple of its resonant frequency (w_1/n) to enhance the nth harmonic. The numerical simulations are performed to obtain the response of the tip-sample system for the proposed method. The proposed method is modified to eliminate the chaotic system response observed in the very high harmonic distortion case. The experiments are carried out to see if the enhanced higher harmonic can discriminate the material variations in heterogeneous samples and to find how it is related to the topography changes on the homogeneous sample surfaces. We show that the enhanced higher harmonic can be utilized to map material heterogeneity in polymer blends with a very high signal-to-noise ratio. The surface features ca. 100 nm in size are clearly resolved. A comparison is also made to conventional tapping-mode topography and phase imaging.

Keywords: Atomic force microscope, tapping-mode, vibrating cantilever, enhanced higher harmonics, nanomechanical material properties.

ÖZET

TİTREŞEN KALDIRACIN GELİŞTİRİLMİŞ YÜKSEK HARMONİKLERİ VASITAŞIYLA MADDELERİN NANOMEKANİKSEL NİTELENDİRİLMESİ

Müjdat Balantekin
Elektrik Mühendisliği, Doktora
Tez Yöneticisi: Prof. Dr. Abdullah Atalar
Mayıs, 2005

Atomik kuvvet mikroskobunun vurma-modu'nda, kaldıraç ucunun denek yüzeyiyle periyodik etkileşimi uç-denek etkileşim kuvvetini doğurur ve kaldıracın saf sinüsoidal devinimi bozulur. Bu nedenle, titreşen kaldıracın tayfı uyarma frekansının tam katlarında yüksek harmonikler ihtiva eder. Bu tezde, nano ölçekteki materyal özelliklerini araştırmak için titreşen kaldıracın yüksek harmoniklerinin bir tanesininden faydalanıyoruz. Eğer etkileşime elastik kuvvet egemense, yüksek harmoniklerin genliğinin belirli bir denek sertliği aralığında monoton bir şekilde arttığını analitik olarak gösterdik. n'inci harmoniği geliştirmek için, kaldıracın kendi rezonans frekansının tam böleninde (w_1/n) uyarıldığı bir yöntem önerdik. Uç-denek sisteminin önerilen yönteme tepkisini elde etmek için sayısal benzetimler icra edildi. Çok yüksek harmonik bozunumu durumunda gözlenen düzensiz sistem tepkisini bertaraf etmek için önerilen yöntem biraz değiştirildi. Geliştirilmiş yüksek harmoniğin çoktürel deneklerdeki madde değişimlerini ayırt edebilirliğini görmek ve tektürel deneklerin yüzeyindeki topografya değişimlerine nasıl bağlı olduğunu bulmak amacıyla deneyler yapıldı. Geliştirilmiş yüksek harmoniğin polimer karışımlarındaki materyal çoktürelliğinin çok yüksek bir sinyal/gürültü oranı ile resimlenmesi için kullanılabileceğini gösterdik. Takriben 100 nm boyutundaki yüzey yapıları net bir şekilde görüntülendi. Ayrıca geleneksel vurma-modu'nun topografya ve faz görüntülemesine karşılaştırma yapıldı.

Anahtar sözcükler: Atomik kuvvet mikroskobu, vurma modu, titreşen kaldıraç, geliştirilmiş yüksek harmonikler, nanomekanik madde özellikleri.

Acknowledgement

There are many people who contributed to this research work. But, first of all, I would like to express my sincere gratitude to Prof. Abdullah Atalar who gave me a chance to work with him during the past few years. Without his invaluable guidance and endless support, I could not finish this study.

I would like to thank the members of the thesis committee, Prof. Hayrettin Köymen, Prof. Ekmel Özbay, Prof. Yusuf Ziya İder, and Prof. Tayfun Akın for reading and commenting on the thesis.

I would like to thank Dr. Ahmet Oral who provided the part of the experimental setup and helped me a lot in his laboratory.

Many thanks to Özgür Şahin for sending the tipholder.

It is a pleasure to thank Prof. Salim Çıracı for providing a conference support.

Special thanks to Ergün Hırlakoğlu for providing the laboratory equipment.

Special thanks to Dr. Soner Kılıç for the polymer samples. I would like to thank Dr. Ahmet Oral one more time for the suggestion of analyzing a block copolymer sample.

It is an obligation for me to thank Dr. Necmi Bıyıklı for the excellent preparation of many samples. I also thank Bayram Bütün for the test samples.

Special thanks to Murat Güre for SEM micrographs.

I would like to thank all the friends, Muharrem, Koray, Münir, Fatih, and Göksel, in the physics department.

I would also like to thank Dr. Levent Değertekin and his students Güçlü Onaran and Zehra Parlak who conducted some experiments for us.

Finally, I thank my family for everything.

Contents

1 Introduction **1**

1.1 Atomic Force Microscopy 1

1.1.1 Contact Mode 3

1.1.2 Hopping Mode 3

1.1.3 Tapping Mode 3

1.1.4 Non-contact Mode 4

1.2 Organization of the Thesis 4

2 Nanomechanical Surface Characterization Techniques **6**

2.1 Nanoindentation 6

2.2 Force Modulation Microscopy 7

2.3 Atomic Force Acoustic Microscopy 7

2.4 Pulsed Force Mode 8

2.5 Dynamic Force Spectroscopy 8

2.6 Phase Imaging 8

2.7 Higher Harmonic Imaging 9

3 Analytical Evaluation of Higher Harmonics 10

3.1 Interaction Modeling 11

3.2 Tip-sample Interaction Forces 13

3.2.1 Conservative Forces 13

3.2.2 Dissipative Forces 17

3.3 Amplitude Damping, Maximum Force and Contact Time 18

3.4 Results and Discussion 23

4 Numerical Analysis for Enhanced Higher Harmonics 27

4.1 Higher Harmonic Enhancement 28

4.2 Simulation Details 30

4.3 Simulation Results 31

4.4 Comparison to Analytical Solution 40

5 Experimental Setup 50

5.1 Instruments 50

5.2 Measurement Cantilever 52

5.3 Noise 52

5.4 Experimental Problems 56

6 Experimental Results 59

6.1 Test Samples 60

6.1.1 A Square-patterned GaAs Substrate 60

6.1.2 A Square-patterned Photoresist on GaAs Substrate 68

6.2 Heterogeneous Polymers 78

6.2.1 20:80 Polystyrene/Polyisoprene Blend 82

6.2.2 80:20 Polystyrene/Polyisoprene Blend 91

6.2.3 50:50 Polystyrene/Polyisoprene Blend 99

6.2.4 Polystyrene-*block*-Polyisoprene-*block*-Polystyrene Copolymer 106

6.3 A Scratched Square-patterned GaAs Substrate 117

6.4 Summary and Discussion 128

7 Conclusions 133

A Experimental Setup 150

B Cantilever Specifications 154

C Detector Calibration 157

List of Figures

3.1 (a) Flexural-beam model. (b) Point-mass model. 12

3.2 van der Waals forces. The tip oscillates above the sample surface. 14

3.3 Elastic contact force. The tip touches the sample in a fraction of its oscillation period. 16

3.4 Normalized maximum repulsive force $F_{max}/(\beta A_1^{\alpha} E)$ (thin lines) and F_{max}/f (thick lines) are plotted as a function of normalized mean tip-surface distance γ for varying values of E^* and f_1 for a cylindrical tip. 21

3.5 Normalized maximum repulsive force $F_{max}/(\beta A_1^{\alpha} E)$ (thin lines) and F_{max}/f (thick lines) are plotted as a function of normalized mean tip-surface distance γ for varying values of E^* and f_1 for a conical tip. 22

3.6 A variation of the first four normalized harmonic amplitudes $|\Lambda(\gamma)|$ as a function of normalized effective tip-sample elasticity $\lambda^{-1}(\gamma)$ for a cylindrical tip. It is assumed that $A_n \ll A_1$. The vertical dashed line marks the $\gamma = 0$ location. 24

3.7 A variation of the first four normalized harmonic amplitudes $|\Lambda(\gamma)|$ as a function of normalized effective tip-sample elasticity $\lambda^{-1}(\gamma)$ for a conical tip. It is assumed that $A_n \ll A_1$. Vertical dashed and dotted lines mark the $\gamma = 0$ and $\gamma = -1$ locations. 25

4.1 Higher harmonic enhancement by matching to a flexural resonance. 29

4.2 Electrical equivalent of mechanical point-mass model. 31

4.3 Simulation results for the second and third harmonics when the cantilever is driven at $w = w_1/2$ and $w = w_1/3$, respectively. A_2/A_0 (stars) and A_3/A_0 (asterisks) are plotted for a paraboloidal tip with a radius of curvature $R = 10$ nm. The simulation parameters are $A_0 = 100$ nm, $A_1/A_0 = 0.99$, $Q = 100$, and $k = 1$ N/m. A vertical dashed line separates the region I ($\gamma < 0$) and region II ($\gamma > 0$), whereas the dotted line indicates the beginning of chaotic region for the third harmonic. Those locations for the second harmonic are very close to these lines and not shown for clarity. . . . 32

4.4 Phase diagrams for four different elastic samples with $w = w_{12}$ and $w_1 = 2\pi\times 120$ krad/s. (a) Free, (b) $E^* = 1$ MPa, (c) $E^* = 1$ GPa, and (d) $E^* = 6$ GPa. Ten oscillation cycles are plotted in each graph. 34

4.5 Tip motions taken from simulations for three different elastic samples when the cantilever is excited at $w = w_1/2$. The position of the undeformed sample surface is indicated by the horizontal line. 35

4.6 Left-hand axis: Simulation results for A_2 ($w = 0.98w_1/2$) marked by stars and A_3 ($w = 0.97w_1/3$) marked by asterisks in the percentage of A_0 with the same parameters of Figure 4.3. The vertical dashed line indicates the $\gamma = 0$ location. Right-hand axis: Simulation results for the conventional case ($w = w_1$). A_2 is marked by circles and A_3 is marked by rectangles in the percentage of A_0 at $A_1/A_0 = 0.6$. The other parameters are the same. 37

4.7 Phase diagrams for the same cases of Fig. 4.4 at $w = 0.98w_{12}$. (a) Free, (b) $E^* = 1$ MPa, (c) $E^* = 1$ GPa, and (d) $E^* = 6$ GPa. Ten oscillation cycles are plotted in each graph. 38

4.8 (a) Fundamental component of interaction force as a function of normalized frequency w/w_1 for two different set points. (b) A close looking around the resonance frequency for $A_1/A_0 = 0.99$. 39

4.9 The variation of the second harmonic amplitude A_2 as a function of effective tip-sample elasticity E^* at $w = 0.95w_1/2$ and $A_1/A_0 = 0.99$. 40

4.10 Tip position and 10×Force in one oscillation cycle. Simulation results are shown by thick dashed lines and analytical solutions are shown by thin solid lines at $w = 0.95w_1/2$ and $A_1/A_0 = 0.99$. (a) $E^* = 50$ GPa, (b) $E^* = 0.5$ GPa, (c) $E^* = 5$ MPa, (d) $E^* = 0.5$ MPa, and (e) $E^* = 0.1$ MPa. 42

4.11 Maximum applied force versus normalized mean tip-surface distance. Analytical solutions (the intersection points of solid lines) and the simulation results (circles) at $w = 0.95w_1/2$ and $A_1/A_0 = 0.99$ for different samples. 43

4.12 The variation of the second harmonic amplitude A_2 as a function of effective tip-sample elasticity E^* at $w = 0.98w_1/2$ and $A_1/A_0 = 0.99$. 44

4.13 Tip position and 10×Force in one oscillation cycle. Simulation results are shown by thick dashed lines and analytical solutions are shown by thin solid lines at $w = 0.98w_1/2$ and $A_1/A_0 = 0.99$. (a) $E^* = 50$ GPa, (b) $E^* = 0.5$ GPa, (c) $E^* = 5$ MPa, (d) $E^* = 0.5$ MPa, and (e) $E^* = 0.1$ MPa. 45

4.14 Maximum applied force versus normalized mean tip-surface distance. Analytical solutions (the intersection points of solid lines) and the simulation results (circles) at $w = 0.98w_1/2$ and $A_1/A_0 = 0.99$ for different samples. 46

4.15 The variation of the second harmonic amplitude A_2 as a function of effective tip-sample elasticity E^* at $w = w_1$ and $A_1/A_0 = 0.8$. . 47

4.16 Tip position and 10×Force in one oscillation cycle. Simulation results are shown by thick dashed lines and analytical solutions are shown by thin solid lines at $w = w_1$ and $A_1/A_0 = 0.8$. (a) $E^* = 50$ GPa, (b) $E^* = 0.5$ GPa, (c) $E^* = 5$ MPa, (d) $E^* = 0.5$ MPa, and (e) $E^* = 0.1$ MPa. 48

4.17 Maximum applied force versus normalized mean tip-surface distance. Analytical solutions (the intersection points of solid lines) and the simulation results (circles) at $w = w_1$ and $A_1/A_0 = 0.8$ for different samples. 49

5.1 Schematic experimental setup. 51

5.2 SEM micrograph of the cantilever showing both the sensor and actuator parts. (a) Top view. (b) Side view. 53

5.3 SEM micrograph of the sensor. (a) Top view. (b) Side view. . . . 54

5.4 SEM micrograph of the tip in (a) and the tip end in (b). 55

5.5 Amplitude and phase variations of the coupled voltage. 58

6.1 Optical micrographs of a square-patterned GaAs substrate at ×50 magnification in (a) and ×100 magnification in (b) and (c). . . . 61

6.2 Enhanced third harmonic imaging of a square-patterned GaAs substrate. (a) Error, (b) Topography, (c) Third harmonic amplitude, (d) Topography (median filtered), and (e) Third harmonic amplitude (image contrast is reversed). The variation from black to white is 2.7 nm in (a), 340 nm in (b), 0.54 nm in (c), and 290 nm in (d). Image parameters: Scan size = 10×10 μm, Pixel size = 256×256, Scan speed = 0.8 μm/s. Operating parameters: $A_0 \approx 1.6$ nm, $A_1/A_0 = 1.2$, $w = 0.97w_{13}$. 62

6.3 Three-dimensional views of the sample in Fig. 6.2. (a) Error, (b) Topography, and (c) Third harmonic amplitude (inverted colors). 63

6.4 Third harmonic amplitude (green), surface topography (blue), and error amplitude (divided by -10 to fit) (black) variations across the line indicated in Fig. 6.2 (b). 64

6.5 Histograms of (a) Error, (b) Surface height, and (c) Third harmonic. 65

6.6 Conventional tapping-mode imaging of a square-patterned GaAs substrate. (a) Error, (b) Topography, (c) Phase, (d) Topography (median filtered), and (e) Phase (image contrast is reversed). The variation from black to white is 9.4 nm in (a), 300 nm in (b), 30° in (c), and 270 nm in (d). Image parameters: Scan size = 10×10 μm, Pixel size = 256×256, Scan speed = 0.8 μm/s. Operating parameters: $A_0 \approx 12.9$ nm, $A_1/A_0 = 0.78$, $w = w_1$. 66

6.7 Three-dimensional views of the sample in Fig. 6.6. (a) Error, (b) Topography, and (c) Phase (inverted colors). 67

6.8 Surface topography (blue), error amplitude (multiplied by 10 to fit) (black), and phase (shifted arbitrarily) (red) variations across the line indicated in Fig. 6.6 (b). 68

6.9 Histograms of (a) Error, (b) Surface height, and (c) Phase. . . . 69

6.10 Optical micrographs of a square-patterned PR on GaAs substrate at ×50 magnification in (a) and ×100 magnification in (b) and (c). 70

6.11 Enhanced third harmonic imaging of a square-patterned PR on GaAs substrate. (a) Error, (b) Topography, and (c) Third harmonic amplitude (image contrast is enhanced). The variation from black to white is 5.2 nm in (a), 700 nm in (b), and 0.9 nm in (c). Image parameters: Scan size = 10×10 μm, Pixel size = 256×256, Scan speed = 0.8 μm/s. Operating parameters: $A_0 \approx 1.6$ nm, $A_1/A_0 = 1.3$, $w = 0.97w_{13}$. 71

6.12 Third harmonic amplitude (green), surface topography (blue), and error amplitude (divided by -10 to fit) (black) variations across the line indicated in Fig. 6.11 (b). 72

6.13 Histograms of (a) Error, (b) Surface height, and (c) Third harmonic. 73

6.14 Enhanced third harmonic imaging of a square-patterned PR on GaAs substrate. (a) Error (image contrast is reversed), (b) Topography, (c) Third harmonic amplitude, and (d) Third harmonic amplitude (image contrast is enhanced). The variation from black to white is 3 nm in (a), 810 nm in (b), and 0.24 nm in (c). Image parameters: Scan size = 10×10 μm, Pixel size = 128×128, Scan speed = 0.5 μm/s. Operating parameters: $A_0 \approx 1.6$ nm, $A_1/A_0 = 1.2$, $w = 0.97w_{13}$. 74

6.15 Three-dimensional views of the sample in Fig. 6.14. (a) Error, (b) Topography, and (c) Third harmonic amplitude (enhanced contrast). 75

6.16 Third harmonic amplitude (green), surface topography (blue), and error amplitude (divided by -10 to fit) (black) variations across the line indicated in Fig. 6.14 (b). 76

6.17 Histograms of (a) Error, (b) Surface height, and (c) Third harmonic. 77

6.18 Conventional tapping-mode imaging of a square-patterned PR on GaAs substrate. (a) Error, (b) Topography, (c) Phase (image contrast is reversed), (d) Topography (median filtered), and (e) Three-dimensional view of topography. The variation from black to white is 10.9 nm in (a), 910 nm in (b), 120° in (c), and 770 nm in (d). Image parameters: Scan size = 10×10 μm, Pixel size = 256×256, Scan speed = 0.8 μm/s. Operating parameters: $A_0 \approx 14.3$ nm, $A_1/A_0 = 0.82$, $w = w_1$. 79

6.19 Surface topography (blue), error amplitude (multiplied by 10 to fit) (black), and phase (shifted arbitrarily) (red) variations across the line indicated in Fig. 6.18 (b). 80

6.20 Histograms of (a) Error, (b) Surface height, and (c) Phase. . . . 81

6.21 Optical micrographs of a 20:80 PS/PI blend at ×50 magnification in (a) and ×100 magnification in (b) and (c). 83

6.22 Enhanced third harmonic imaging of a 20:80 PS/PI blend. (a) Error, (b) Topography, (c) Third harmonic amplitude, and (d) Topography (median filtered). The variation from blue to red is 0.66 nm in (a), 150 nm in (b), 0.2 nm in (c), and 130 nm in (d). Image parameters: Scan size = 10×10 μm, Pixel size = 256×256, Scan speed = 1 μm/s. Operating parameters: $A_0 \approx 2.4$ nm, $A_1/A_0 = 1.2$, $w = 0.97w_{13}$. 84

6.23 Three-dimensional views of the sample in Fig. 6.22. (a) Error, (b) Topography, (c) Third harmonic amplitude, and (d) Topography (median filtered). 85

6.24 Third harmonic amplitude (green), surface topography (blue), and error amplitude (divided by -10 to fit) (black) variations across the dashed line indicated in Fig. 6.22 (d). 86

6.25 Third harmonic amplitude (green), surface topography (blue), and error amplitude (divided by -10 to fit) (black) variations across the dotted line indicated in Fig. 6.22 (d). 87

6.26 Histograms of (a) Error, (b) Surface height, and (c) Third harmonic. 88

6.27 Conventional tapping-mode imaging of of a 20:80 PS/PI blend. (a) Error, (b) Topography, (c) Phase, and (d) Error (image contrast is reversed). The variation from blue to red is 1 nm in (a), 150 nm in (b), and 12° in (c). Image parameters: Scan size = 10×10 μm, Pixel size = 256×256, Scan speed = 1 μm/s. Operating parameters: $A_0 \approx 10$ nm, $A_1/A_0 = 0.9$, $w = w_1$. 89

6.28 Three-dimensional views of the sample in Fig. 6.27. (a) Error, (b) Topography, (c) Phase, and (d) Error (inverted colors). 90

6.29 Surface topography (blue), error amplitude (multiplied by 10 to fit) (black), and phase (shifted arbitrarily) (red) variations across the line indicated in Fig. 6.27 (b). 91

6.30 Histograms of (a) Error, (b) Surface height, and (c) Phase. . . . 92

6.31 Optical micrographs of a 80:20 PS/PI blend at $\times50$ magnification in (a) and $\times100$ magnification in (b) and (c). 93

6.32 Enhanced third harmonic imaging of a 80:20 PS/PI blend. (a) Error, (b) Topography, and (c) Third harmonic amplitude. The variation from blue to red is 0.28 nm in (a), 230 nm in (b), and 0.07 nm in (c). Image parameters: Scan size = 10×10 μm, Pixel size = 256×256, Scan speed = 0.6 μm/s. Operating parameters: $A_0 \approx 2.4$ nm, $A_1/A_0 = 1.2$, $w = 0.97w_{13}$. 94

6.33 Three-dimensional views of the sample in Fig. 6.32. (a) Error, (b) Topography, and (c) Third harmonic amplitude. 95

6.34 Third harmonic amplitude (divided by 10 to fit) (green), surface topography (blue), and error amplitude (divided by 10 to fit) (black) variations across the line indicated in Fig. 6.32 (b). 96

6.35 Histograms of (a) Error, (b) Surface height, and (c) Third harmonic. 97

6.36 Conventional tapping-mode imaging of of a 80:20 PS/PI blend. (a) Error, (b) Topography, and (c) Phase. The variation from black to white is 1.7 nm in (a), 80 nm in (b), and 17° in (c). Image parameters: Scan size = 10×10 μm, Pixel size = 256×256, Scan speed = 0.6 μm/s. Operating parameters: $A_0 \approx 12.7$ nm, $A_1/A_0 = 0.84$, $w = w_1$. 98

6.37 Surface topography (blue), error amplitude (black), and phase (shifted arbitrarily) (red) variations across the line indicated in Fig. 6.36 (b). 99

6.38 Histograms of (a) Error, (b) Surface height, and (c) Phase. . . . 100

6.39 Optical micrographs of a 50:50 PS/PI blend at ×50 magnification in (a) and ×100 magnification in (b) and (c). 101

6.40 Enhanced third harmonic imaging of a 50:50 PS/PI blend. (a) Error, (b) Topography, (c) Third harmonic amplitude, and (d) Third harmonic amplitude (median filtered). The variation from blue to red is 1.2 nm in (a), 200 nm in (b), 0.28 nm in (c), and 0.2 nm in (d). Image parameters: Scan size = 10×10 μm, Pixel size = 256×256, Scan speed = 1 μm/s. Operating parameters: $A_0 \approx 2.4$ nm, $A_1/A_0 = 1.2$, $w = 0.97w_{13}$. 102

6.41 Reverse scan of the sample in Fig. 6.40. (a) Error, (b) Topography, (c) Third harmonic amplitude, and (d) Third harmonic amplitude (median filtered). The variation from black to white is 1.3 nm in (a), 200 nm in (b), 0.3 nm in (c), and 0.2 nm in (d). 103

6.42 Third harmonic amplitude (green), surface topography (blue), and error amplitude (divided by -10 to fit) (black) variations across the line indicated in Fig. 6.40 (b). 104

6.43 Histograms of (a) Error, (b) Surface height, and (c) Third harmonic. 105

6.44 Conventional tapping-mode imaging of of a 50:50 PS/PI blend. (a) Error, (b) Phase, (c) Topography, (d) Topography (image contrast is enhanced), and (e) Three-dimensional view of topography (enhanced contrast). The variation from blue to red is 6 nm in (a), 98° in (b), and 500 nm in (c). Image parameters: Scan size = 10×10 μm, Pixel size = 256×256, Scan speed = 0.6 μm/s. Operating parameters: $A_0 \approx 8.7$ nm, $A_1/A_0 = 0.6$, $w = w_1$. 107

6.45 Surface topography (blue), error amplitude (multiplied by 10 to fit) (black), and phase (shifted arbitrarily) (red) variations across the vertical line indicated in Fig. 6.44 (c). 108

6.46 Surface topography (blue), error amplitude (multiplied by 10 to fit) (black), and phase (shifted arbitrarily) (red) variations across the horizontal line indicated in Fig. 6.44 (c). 109

6.47 Histograms of (a) Error, (b) Surface height, and (c) Phase. . . . 110

6.48 Optical micrographs of a SIS copolymer at ×50 magnification in (a) and ×100 magnification in (b) and (c). 111

6.49 Enhanced third harmonic imaging of a SIS copolymer. (a) Error, (b) Topography, and (c) Third harmonic amplitude. The variation from blue to red is 0.65 nm in (a), 190 nm in (b), and 0.2 nm in (c). Image parameters: Scan size = 10×10 μm, Pixel size = 256×256, Scan speed = 1 μm/s. Operating parameters: $A_0 \approx$ 2.4 nm, $A_1/A_0 = 1.2$, $w = 0.97w_{13}$. 112

6.50 Three-dimensional views of the sample in Fig. 6.49. (a) Error, (b) Topography, and (c) Third harmonic amplitude. 113

6.51 Third harmonic amplitude (green), surface topography (blue), and error amplitude (divided by -10 to fit) (black) variations across the vertical line indicated in Fig. 6.49 (b). 114

6.52 Third harmonic amplitude (green), surface topography (blue), and error amplitude (divided by -10 to fit) (black) variations across the dotted line indicated in Fig. 6.49 (b). 115

6.53 Histograms of (a) Error, (b) Surface height, and (c) Third harmonic. 116

6.54 Conventional tapping-mode imaging of of a SIS copolymer. (a) Error, (b) Topography, (c) Phase, (d) Error (image contrast is reversed). The contrast of the images in (a)-(d) are enhanced by the software and the contrast enhanced images are shown in (e)-(h). The variation from black to white is 2.8 nm in (a), 160 nm in (b), and 56° in (c). Image parameters: Scan size = 10×10 μm, Pixel size = 256×256, Scan speed = 0.6 μm/s. Operating parameters: $A_0 \approx 10.5$ nm, $A_1/A_0 = 0.75$, $w = w_1$. 118

6.55 Three-dimensional views of the sample in Fig. 6.54. (a) Error, (b) Topography, and (c) Phase. The contrast in the images is enhanced. 119

6.56 Surface topography (blue), error amplitude (multiplied by 10 to fit) (black), and phase (shifted arbitrarily) (red) variations across the line indicated in Fig. 6.54 (b). 120

6.57 Histograms of (a) Error, (b) Surface height, and (c) Phase. . . . 121

6.58 Optical micrographs of a scratched square-patterned GaAs substrate at $\times50$ magnification in (a) and $\times100$ magnification in (b) and (c). 122

6.59 Previously taken topography image of the square-patterned GaAs substrate. 123

6.60 Enhanced third harmonic imaging of a scratched square-patterned GaAs substrate. (a) Error, (b) Topography, (c) Third harmonic amplitude, and (d) Third harmonic amplitude (image contrast is enhanced). The variation from black to white is 0.36 nm in (a), 320 nm in (b), and 0.91 nm in (c). Image parameters: Scan size = 15×15 μm, Pixel size = 256×256, Scan speed = 0.4 μm/s. Operating parameters: $A_0 \approx 2.1$ nm, $A_1/A_0 = 1.03$, $w = 0.97 w_{13}$. . . 124

6.61 Three-dimensional views of the sample in Fig. 6.59. (a) Error, (b) Topography, (c) Third harmonic amplitude, and (d) Third harmonic amplitude (enhanced contrast). 125

6.62 Third harmonic amplitude (green), surface topography (blue), and error amplitude (reversed) (black) variations across the line indicated in Fig. 6.59 (b). 126

6.63 Histograms of (a) Error, (b) Surface height, and (c) Third harmonic. 127

6.64 Enhanced fourth harmonic imaging of a scratched square-patterned GaAs substrate. (a) Error (low pass filtered), (b) Topography, and (c) Fourth harmonic amplitude (low pass filtered). The variation from black to white is 1.1 nm in (a), 340 nm in (b), and 0.09 nm in (c). Image parameters: Scan size = 15×15 μm, Pixel size = 128×128, Scan speed = 0.4 μm/s. Operating parameters: $A_0 \approx 3.8$ nm, $A_1/A_0 = 0.9$, $w = 0.97 w_{14}$. 128

6.65 Three-dimensional views of the sample in Fig. 6.64. (a) Topography and (b) Fourth harmonic amplitude. The contrast in the images is enhanced. 129

A.1 The experimental setup. 151

A.2 Instruments in the setup. 152

A.3 Optical AFM head. 153

B.1 (a) SEM micrograph of the cantilever. (b) Probe dimensions. 155

List of Tables

6.1 Properties of polystyrene and polyisoprene. 80

B.1 Cantilever specifications. 155

Chapter 1

Introduction

Nanoscale science is an interesting research field that will shape the future of the technology. Characterization at the nanoscale becomes increasingly important as the device dimensions shrink. Furthermore, there are many fields, like molecular biology, genetics, polymer science, that require effective characterization tools to understand the nature of the materials. Atomic force microscope (AFM) is a kind of scanning probe microscope and it can be used to characterize the nanomechanical properties of materials.

1.1 Atomic Force Microscopy

Since its invention in 1986, the atomic force microscope [1] has been utilized in such diverse fields as materials science, physics, chemistry and biology. It is a powerful tool used for high resolution imaging, manipulating and characterizing a wide range of materials like metals, polymers, ceramics, semiconductors, and biomolecules [2–6]. The three dimensional images have allowed the scientists to see atoms (even subatomic features), molecules and other nanoscale topographical features with excellent accuracy and precision in air, liquid and vacuum environments [7–9].

After its commercialization, the AFM has been used in many research centers for different purposes. It is a so versatile instrument that can be used for the manipulation of single atoms [6], measurement of solution viscosity [10], determination of the elastic modulus of nanotubes [11], analysis of human chromosomes [12], thin film characterization [13], investigation of capillary forces [14], monitoring the cellular processes in real time [15], characterization of polymers [16], nanolithography [17], data storage [18], mechanical characterization [19], and so on at very high resolution.

The main component of an AFM is a flexible cantilever which has a very sharp tip at its free end. The cantilever is usually microfabricated from silicon or silicon nitride in a rectangular geometry with typical dimensions that are 100-300 μm in length, 10-30 μm in width and 0.5-3 μm in thickness, resulting in a spring constant between 0.01 and 100 N/m. Generally, the cantilever tips have pyramidal or conical shapes [20].

The cantilever deflection is measured by a sensitive detector. The detector used to measure the deflection of the cantilever is crucial in determining the performance of the microscope. There are several deflection detection methods used in AFM systems. Most widely used detectors are based on optical lever [21, 22], interferometry [23, 24], piezoresistivity [25], and piezoelectricity [26].

The vertical resolution of the instrument is dependent on the detector sensitivity and the noise. The lateral resolution depends on the sharpness of the probe and the applied force. The originators of the microscope reported a lateral resolution of 30 Å and a vertical resolution less than 1 Å.

There are four operating modes of AFM discussed below. The first two are the quasi-static modes and the last two are the dynamic modes in which the cantilever is oscillated at or near its resonance frequency.

1.1.1 Contact Mode

This is the original operating mode of AFM [1]. In the presence of tip-sample forces, the cantilever deflects. This deflection is kept constant during the scan by a feedback controller. The output of the controller gives the surface topography. The lateral forces are very significant in this mode. Therefore very soft cantilevers are employed to reduce the tip and surface damage. Atomic resolution images of both conducting and nonconducting surfaces were obtained by Albrecht and Quate [27, 28] in contact mode. The contact mode is preferred if the scan speed is the primary consideration.

1.1.2 Hopping Mode

This technique is developed to reduce the lateral forces during the scan [29]. It is named as jumping mode [30] and digital probing mode [31] by other research groups. In this operation, surface topography is obtained under a constant repulsive force at each measurement point. The probing tip is then withdrawn from the surface and moved to the next measurement point. This is a more precise and gentle method than the contact mode at the expense of lower scan speed.

1.1.3 Tapping Mode

Tapping-mode [32] (also called intermittent contact mode) is the most widely used operating mode in which the cantilever tip can experience both attractive and repulsive forces intermittently. In this mode, the cantilever is oscillated at or near its free resonant frequency. Hence, the force sensitivity of the measurement is increased by the quality factor of the cantilever. In tapping-mode operation, the amplitude of the cantilever vibration is used in feedback circuitry, i.e., the oscillation amplitude is kept constant during imaging. Therefore it is also referred as amplitude modulation AFM (AM-AFM). The primary advantage of tapping mode is that the lateral forces between the tip and the sample can be eliminated, which greatly improves the image resolution. Tapping mode experiments are

done generally in air or liquid. Amplitude modulation is not suitable for vacuum environment since the Q-factor of the cantilever is very high (up to 10^5) and this means a very slow feedback response.

1.1.4 Non-contact Mode

Non-contact mode of operation is generally employed under ultrahigh vacuum conditions for atomic resolution imaging [33]. The cantilever quality factors reach to very high values in vacuum, and imaging process with AM detection method can be very long depending on the resonant frequency. To overcome this problem, a frequency modulation (FM) detection method was developed by Albrecht *et al.* [34]. In this method, the cantilever is kept oscillating at its resonant frequency by applying a positive feedback. The measurement bandwidth can be set independent of quality factor. Hence the operation speed can be increased. This mode has two submodes, namely, the constant-vibration mode and the constant excitation mode. In the former, amplitude regulator maintains the vibration amplitude at a constant level. The frequency shift regulates the tip-surface separation. It was found that the constant-excitation mode is more stable and gentle compared to the constant-vibration mode [35].

1.2 Organization of the Thesis

Chapter 2 summarizes several surface characterization techniques related to the AFM. We discuss very briefly their operating principles, advantages, and disadvantages.

Chapter 3 gives the interaction models. We summarize the tip-sample forces. The relation between the interaction force parameters is derived by relating the amplitude damping to the fundamental component of interaction force. The higher harmonic amplitudes are plotted as a function of effective tip-sample elasticity by applying the Hertzian contact mechanics.

We propose a new method to enhance the higher harmonics in Chapter 4. The proposed method is tested by numerical simulations. The problematic behaviors observed in the simulations are eliminated by slightly modifying the method. We also compared the numerical results to the analytical solution of Chapter 2 for different cases.

Chapter 5 describes the experimental setup. We also discuss several problems observed in the experiments and their possible solutions.

The results of enhanced higher harmonic imaging experiments on several samples are presented in Chapter 6. In this chapter, we also show the results obtained with conventional tapping-mode experiments to make a comparison.

Chapter 2

Nanomechanical Surface Characterization Techniques

The atomic force microscope was originally invented to obtain atomic resolution images of sample surfaces. The methods discussed below have been developed to measure the surface mechanical properties at a high local resolution provided by the AFM.

2.1 Nanoindentation

The nanoindentation (also known as force curve method) technique has long been utilized to measure the Young's modulus, the elastic and plastic behavior, and hardness [36]. It can also be used in surface manipulation [6]. Elastic properties of aerogel powder particles [37], cells [38, 39], hydrogels [40], polymers [41, 42], and a Langmuir-Blodgett film [43] had been investigated with this method.

Basically, the lever deflection is measured during the loading and unloading cycles. By using the force versus distance curve, the information about the sample elasticity, surface forces, and maximum adhesion force can be obtained. Since the measurement is done at a single point, acquiring an image of a surface is a very

time consuming process depending on the required resolution and image size.

2.2 Force Modulation Microscopy

Force modulation microscopy (FMM) [44] has a very simple operating principle. A small low-frequency modulation is introduced vertically while the tip is in contact with the sample surface. By measuring the cantilever deflection resulting from this modulation, sample stiffness is found. Thereafter, by using the Hertzian contact theory, the surface elasticity can be obtained. If the cantilever stiffness is much less than the tip-sample contact stiffness, the variations in sample stiffness can not be detected easily. Therefore FMM requires a cantilever much stiffer than the tip-sample contact stiffness. The effect of capillary forces on the measurements was observed [45]. In this method, the applied static load degrades the lateral resolution.

2.3 Atomic Force Acoustic Microscopy

Another method, known as atomic force acoustic microscopy [46] or ultrasonic force microscopy [47], has been in use to determine the contact stiffness by measuring the cantilever contact resonance frequencies. Applying the Hertzian contact theory, the sample elasticity can be extracted. Since the sample or the cantilever is vibrated at ultrasonic frequencies, the compliance of stiff materials can be mapped with soft cantilevers. However, uncertainties in the cantilever geometry introduce significant errors and tip wearing degrades the reproducibility of the measurements [48, 49]. The lateral resolution is degraded by the applied static load. Moreover, the experimental setup is different from conventional imaging setups and requires extra equipment [50].

2.4 Pulsed Force Mode

This method is developed to image elastic and adhesive properties of the sample simultaneously with topography [51]. In principle, it is the same as the adhesion mode [52]. It can be considered as a combination FMM and nanoindentation methods. A sinusoidal modulation is applied to the piezotube. The modulation frequency is chosen to be well below the resonance frequency of the cantilever. The modulation amplitude is much larger than that applied in FMM such that the tip jumps in and out of contact during each cycle. Hence a force versus time curve can be recorded. By analyzing this curve, mechanical properties of the sample can be obtained. The scan speed is determined by the modulation frequency. The method is found to be problematic in liquid [53]. It also requires additional electronics.

2.5 Dynamic Force Spectroscopy

A force spectroscopy curve is obtained by varying the distance between the tip and the sample while measuring the oscillation frequency, amplitude or phase. In the FM-AFM, the tip-sample interaction force can be determined from experimentally obtained frequency shifts [54–58]. This can be a very time consuming process for imaging applications.

2.6 Phase Imaging

The two variables of tapping-mode operation are the amplitude and the phase shift (relative to drive signal) of the cantilever oscillation. The phase shift depends on the energy dissipation [59–61]. The contrast in the phase images is related to the attractive-repulsive state transition [62], in-plane structural and mechanical properties [63], viscoelastic properties and adhesion forces [64]. The phase can not be used to differentiate the compliance of purely elastic samples [65]. If the

energy dissipation is constant, then the phase depends only on the oscillation amplitude.

2.7 Higher Harmonic Imaging

It was recently found that the anharmonic oscillations of the cantilever contain information about the material nanomechanical properties [66–69]. Hillenbrand *et al.* used the 13th harmonic signal to increase the image contrast [67]. Some authors used second and third harmonic amplitudes to map the surface charge density of DNA molecules [70]. Dürig realized that the higher harmonic amplitudes can be utilized for the reconstruction of the interaction force [71]. Numerical analysis by Rodriguez and Garcia showed that phase of the second mode can be utilized to map the Hamaker constant [72].

Since the tip-sample interaction is periodic, the frequency spectrum of the detected signal has components (harmonics) at integer multiples of the driving frequency. These harmonics depend on the interaction force and hence the material properties. The effect of higher harmonics cannot be neglected if the quality factor of the cantilever is low [73].

Chapter 3

Analytical Evaluation of Higher Harmonics

The aim of this chapter is to obtain an analytic expression of higher harmonic amplitudes as a function of the sample elasticity. This will give us an insight on the relation between the higher harmonics and tip-sample force. It will also enlighten us on how a sample property (the sample stiffness in this case) can be extracted from a harmonic amplitude measurement. To do that we assumed a very low harmonic distortion and we utilized the Hertzian contact mechanics.

We first give a model of the tip-sample system. Thereafter we discuss briefly the interaction forces which can take place in a typical tapping-mode experiment. By utilizing amplitude damping, the relation between the maximum force and the contact time is established. Finally, we derive the relation between the harmonic amplitude and the sample elasticity by using the contact time (or mean tip-sample distance) as an independent parameter.

3.1 Interaction Modeling

There are two models used in the literature to analyze the cantilever dynamics. One of them, the flexural-beam model shown in Fig. 3.1 (a), considers a rectangular cantilever as a multiple-degrees-of-freedom (MDOF) system. It takes the higher-order vibration modes into account and therefore should be employed if one requires the response of the cantilever above the first resonance. In this model, the transverse displacement of an undamped cantilever having uniform cross section and mass density can be obtained as a function of the longitudinal direction by solving the one dimensional Euler-Bernoulli equation. Boundary conditions at the cantilever end are constrained by the spring (k^*) and dashpot (γ^*). The sample spring constant k^* is equated to the negative derivative of the tip-sample force in the equilibrium position. For this reason, the model is considered to be valid only for very small vibration amplitudes. The damper accounts for the energy dissipation due to tip-sample interaction. A through discussion on this model and its application can be found in Ref. [46].

The point-mass model, on the other hand, is neglecting the higher-order flexural modes, which simplifies the analysis considerably. It was shown that the point-mass model can usually be applied instead of beam model to analyze the tip-sample system if the cantilever is driven at its fundamental resonant frequency and the quality factor is high [74]. But, the two methods yield significantly different results if the excitation is above the fundamental resonant frequency [75], like in atomic force acoustic microscopy.

In the point-mass model [Fig. 3.1 (b)], the cantilever is represented by a point mass attached to a spring and a dashpot. The effective mass m^* is chosen such that the resonance frequency of the system is equal to the first flexural vibration frequency w_1. Hence the effective mass is approximately equal to one-fourth of the real mass. The dashpot represents the air damping which results in a finite Q-factor. The spring constant k depends on the cantilever dimensions and material properties. The dimensions A_1 (oscillation amplitude), z_r (rest position of the tip), and z (instantaneous position of the tip) are shown to visualize the

(a)

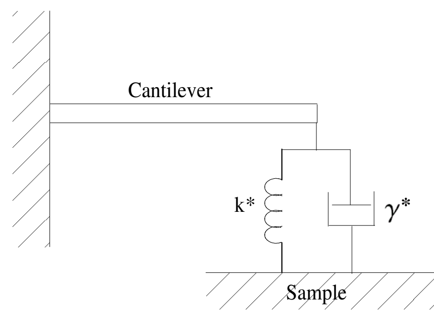

(b)

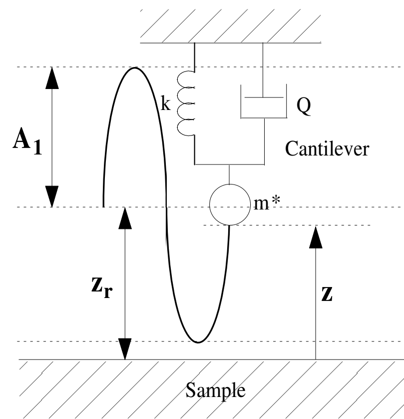

Figure 3.1: (a) Flexural-beam model. (b) Point-mass model.

interaction. The tip motion is described by the following differential equation:

$$m^*\ddot{z} + \frac{m^* w_1}{Q}\dot{z} + k(z - z_r) = F_0\cos(wt) + f_{\mathbf{TS}}(t)\ . \tag{3.1}$$

F_0 is the driving force which determines the free oscillation amplitude and w is the excitation frequency. $f_{\mathbf{TS}}$ is the tip-sample force which causes amplitude damping, phase shift and produces higher harmonics.

3.2 Tip-sample Interaction Forces

In a tapping-mode operation, the cantilever tip may experience both conservative and dissipative forces. These forces are highly nonlinear and due to nonlinear interaction the higher harmonics are produced. In order to relate the higher harmonics to the sample properties, we must know their dependencies on tip-sample distance for a given tip shape. In the following summary, neither we consider the electrostatic and magnetic forces nor the short-ranged forces due to chemical bonding.

3.2.1 Conservative Forces

The conservative forces do not cause energy dissipation, meaning that the phase of the cantilever oscillation is dependent only on the oscillation amplitude. Nevertheless, their effect can be observed in the reduction of free oscillation amplitude or in the emerging higher harmonics.

3.2.1.1 van der Waals Forces

van der Waals (vdW) forces are the surface forces that affect the tip motion when the tip approaches the sample. They encompass three different forces, namely the London force (also called the dispersion force), the Keesom force, and the Debye force. The dispersion force is the dominant component of the vdW forces.

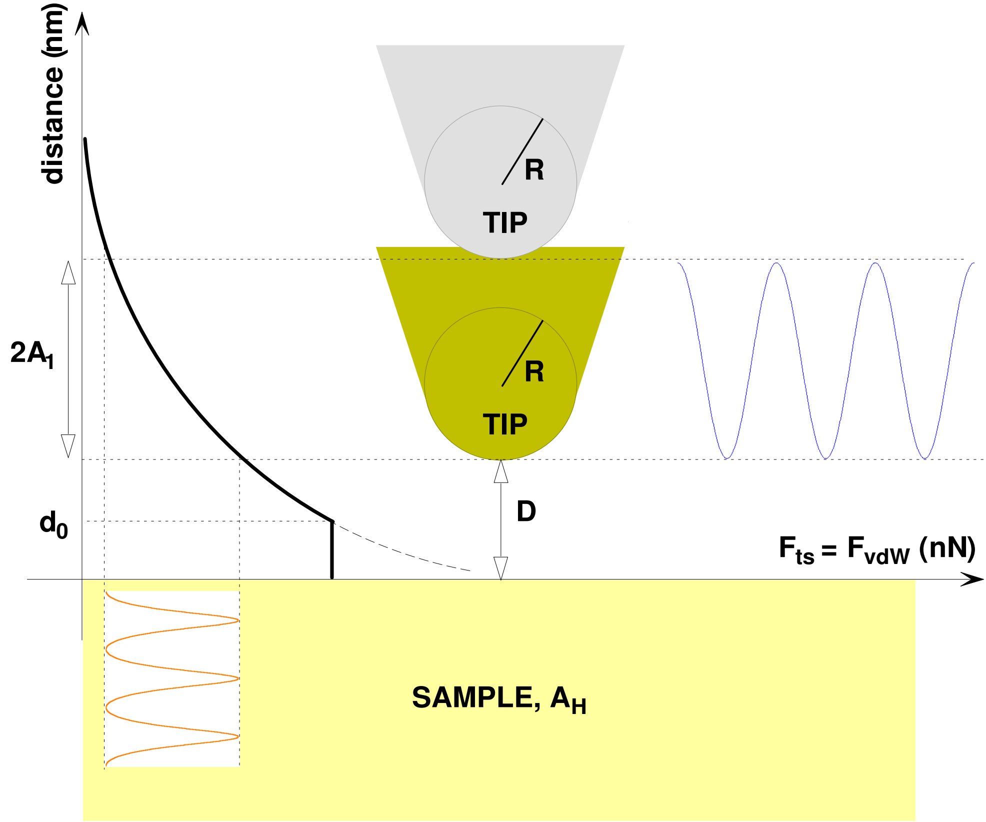

Figure 3.2: van der Waals forces. The tip oscillates above the sample surface.

The vdW forces for a sphere (tip) with a radius of R and flat (sample) geometry can be obtained from Derjaguin approximation as a function of distance D as

$$F_{vdW} = \frac{-A_H R}{6D^2} \; . \tag{3.2}$$

This equation is valid for $D \ll R$ [76]. The Hamaker constant (A_H) reflects the strength of the vdW forces. A_H is a function of the permittivities and refraction indices of tip, sample and the medium in which the interaction takes place. F_{vdW} can be attractive or repulsive depending on the choice of the medium. Hartmann suggested to immerse the tip and sample into a liquid so that the repulsive vdW forces prevent the tip from jumping into contact with the sample [77]. Typically, A_H is on the order of 10^{-19} J in air or vacuum.

In Fig. 3.2 we show how the vdW forces will change as the tip oscillates near

a surface. Since the forces are nonlinear, they produce higher harmonics which can be utilized to determine the Hamaker constant. Notice that as $D \rightarrow 0$, $F_{vdW} \rightarrow \infty$. Therefore below the intermolecular distance d_0, the vdW forces are replaced by the adhesion force in the numerical simulations (see next section).

3.2.1.2 Contact Forces

Contact forces include the elastic force and the adhesion force. The elastic force depends on the effective tip-sample elasticity and the adhesion force depends on the work of adhesion. There are several continuum contact theories which relate the applied force to the indentation depth.

- **Hertzian mechanics:**

This is the simplest theory which does not take the adhesion force into account. According to the Hertzian contact mechanics, the normal load F_H is related to the indentation depth D for any kind of indenter as follows [37]

$$F_H = \beta E^* D^{\alpha} , \tag{3.3}$$

where E^* is the effective Young's modulus, β and α are the constants dependent on the tip geometry. E^* is related to the Young's modulus (E) and Poisson ratio (ν) of the tip and sample:

$$E^* = \left(\frac{1 - \nu^2{}_{tip}}{E_{tip}} + \frac{1 - \nu^2{}_{sample}}{E_{sample}} \right)^{-1} . \tag{3.4}$$

Mostly, the silicon cantilevers are employed in tapping-mode experiments. Silicon has a high Young's modulus and the first term in the parenthesis is usually ignored.

Figure 3.3 shows that as the tip hits to the sample, elastic force (pulses) is created. This force and hence its harmonics depend on the sample elasticity. In the case of small harmonic distortion, the tip motion can still be assumed to be sinusoidal.

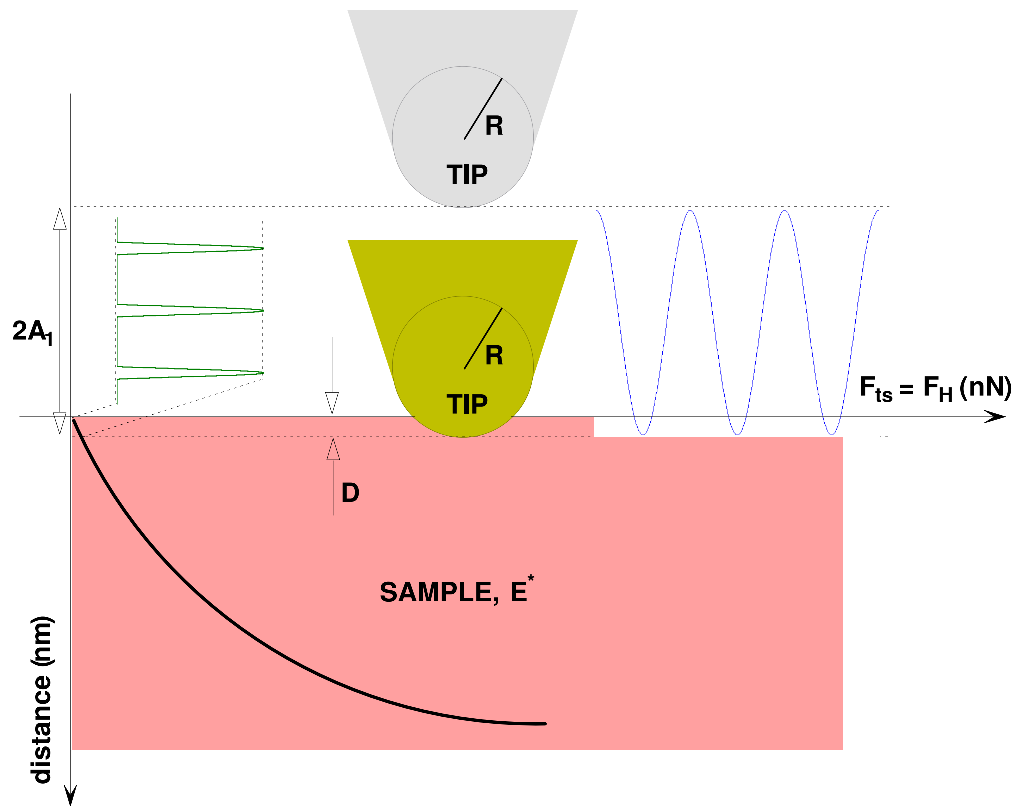

Figure 3.3: Elastic contact force. The tip touches the sample in a fraction of its oscillation period.

- **DMT mechanics:**

Unlike the Hertzian theory, DMT (Derjaguin-Muller-Toporov) mechanics includes the adhesion force. For a sphere-plane geometry, the load is related to the indentation depth as

$$F_{DMT} = \frac{4}{3}E^{*}\sqrt{R}D^{3/2} - 4\pi R\varpi \ . \tag{3.5}$$

ϖ is the adhesion energy per unit area. In the simulations of tapping-mode AFM, generally the DMT mechanics is employed [78–80]. In that case, the adhesion force is equated to the van der Waals forces at the point of contact. Then the interaction force as a function of tip position z can be written as

$$F_{ts} = \begin{cases} \frac{-A_H R}{6z^2} & \text{for} \quad z \geq d_0 \\ \\ \frac{-A_H R}{6{d_0}^2} + \frac{4}{3}E^{*}\sqrt{R}(d_0 - z)^{3/2} & \text{for} \quad z \leq d_0 \end{cases} \tag{3.6}$$

where d_0 is equal to $\sqrt{H/(24\pi\varpi)}$. Note that the slope of the force at d_0 is not continuous.

There are other approaches [81, 82] formulating the load in terms of indentation, like BCP (Burnham-Colton-Pollock), JKRS (Johnson-Kendall-Roberts-Sperling), and Maugis mechanics. They are more complex, but they have less deficiencies. In BCP mechanics, e.g., the slope at the point of contact is continuous. JKRS and Maugis mechanics include adhesion hysteresis. Since our aim is to show the importance of the higher harmonic imaging in a lucid manner, we will use the Hertzian mechanics in our analysis.

3.2.2 Dissipative Forces

Although not taken into account, it is worth to mention about the dissipative forces which may take place in an experiment. The dissipative forces are the cause of energy dissipation which can be mapped to obtain a material specific image contrast [61].

3.2.2.1 Capillary Forces

The tapping-mode experiments are usually done in air. The ambient humidity leads to a thin film of water which covers the tip and sample. As the tip approaches the surface, a meniscus forms upon contact of the adsorbed water layers. When the tip retracts, the capillary neck breaks at a larger distance. This hysteretic behavior results in energy dissipation in each oscillation cycle. The capillary forces can be large enough to obscure vdW forces. Their effect is more sensible on hydrophilic samples than on hydrophobic samples [83].

3.2.2.2 Viscous Forces

Compliant samples, like polymers and biological materials, show viscoelastic behavior rather than pure elastic or viscous response. Their mechanical behaviors are usually modeled with a parallel combination of a spring and a dashpot (the Voigt model) [84]. The viscous force is proportional to the sample viscosity, radius of the contact area, and tip velocity. Dubourg *et al.* used tapping-mode AFM to determine quantitatively the viscosity of a triblock copolymer [85].

In addition to capillary and viscous forces, there may be other processes like plastic deformation of the sample, adhesion hysteresis, and mechanical instability of the cantilever which cause energy dissipation.

3.3 Amplitude Damping, Maximum Force and Contact Time

In tapping-mode operation, as the tip taps on an elastic sample, it indents periodically into the sample during the contact. If we assume that the sinusoidal nature of the tip motion is preserved (low harmonic distortion), then the indentation depth is also sinusoidal in the contact duration τ. For a given set point amplitude A_1, mean tip to surface separation z_r and excitation frequency w, we

can express the time dependent interaction force $f_{\mathbf{TS}}(t)$ in one period if $|z_r| \leq A_1$ as

$$f_{\mathbf{TS}}(t) = \begin{cases} \beta E^*[A_1 \cos(wt) - z_r]^\alpha & \text{for} \quad |t| \leq \cos^{-1}(z_r/A_1)/w \\ \\ 0 & \text{otherwise} \end{cases} \tag{3.7}$$

If $z_r > A_1$ then $f_{\mathbf{TS}}(t) = 0$ and if $z_r < -A_1$ then $f_{\mathbf{TS}}(t) = \beta E^*[A_1 \cos(wt) - z_r]^\alpha$.

For a cylindrical tip of radius R ($\beta = 2R$, $\alpha = 1$), $f_{\mathbf{TS}}(t)$ is a clipped cosine function for $|z_r| \leq A_1$. Defining a normalized mean tip to surface distance, γ, as $\gamma = z_r/A_1$, the maximum repulsive force applied to the sample is found to be

$$F_{max} = 2RE^* A_1(1 - \gamma) \; . \tag{3.8}$$

In the steady-state, the interaction force can be expanded in a Fourier series [66, 86] as $f_{\mathbf{TS}}(t) = f_0 + \sum_{n \geq 1} f_n \cos(nwt)$. For $|\gamma| \leq 1$, the average force f_0 is given by

$$f_0 = F_{max} \xi \frac{\text{sinc}(\xi) - \gamma}{1 - \gamma} \; , \tag{3.9}$$

where $\text{sinc}(x) \triangleq \sin(\pi x)/(\pi x)$. $\xi = \cos^{-1}(\gamma)/\pi$ is the normalized contact time, i.e. contact time divided by one period ($w\tau/2\pi$). The nth component of the interaction force f_n is

$$f_n = F_{max} \xi g_n(\gamma)/(1 - \gamma) \; , \tag{3.10}$$

where $g_n(\gamma)$ is given by

$$g_n(\gamma) = \text{sinc}[(1 + n)\xi] + \text{sinc}[(1 - n)\xi] - 2\gamma \text{sinc}(n\xi) \; . \tag{3.11}$$

For $n = 1$ we get the fundamental component of $f_{\mathbf{TS}}(t)$

$$f_1 = F_{max} \xi \frac{1 - \text{sinc}(2\xi)}{1 - \gamma} \; . \tag{3.12}$$

f_1 causes an amplitude damping [87] and can be related to oscillation amplitude and cantilever parameters under the assumption of low harmonic distortion as follows

$$f_1 = A_1 \varsigma(w) |H(w)|^{-1} \; , \tag{3.13}$$

where

$$\varsigma(w) = \{(A_0/A_1)^2 - \sin^2[\angle H(w)]\}^{1/2} - \cos[\angle H(w)] \ , \tag{3.14}$$

and the transfer function of a fundamental flexural eigenmode of the cantilever is

$$H(w) = \frac{Q}{k} \frac{(1 - w^2/w_1^2)\, Q - iw/w_1}{(1 - w^2/w_1^2)^2\, Q^2 + w^2/w_1^2} \ , \tag{3.15}$$

here k, Q, A_0 and w_1 are the cantilever stiffness, quality factor, free oscillation amplitude and fundamental resonant frequency, respectively. Equations (3.12) and (3.13) tell us that for any given set of cantilever parameters and a set point amplitude, F_{max} and ξ are almost inversely proportional.

A typical tip can be approximated to have a conical shape. In this case, the parameter defining the tip geometry is the semivertical angle θ ($\beta = 2\tan(\theta)/\pi$, $\alpha = 2$). The maximum force applied to the sample is found to be

$$F_{max} = 2\tan(\theta) E^* A_1^2 (1-\gamma)^2/\pi \ . \tag{3.16}$$

The average of the interaction force is

$$f_0 = F_{max}\xi \frac{0.5 + \gamma^2 + 0.5\mathrm{sinc}(2\xi) - 2\gamma\mathrm{sinc}(\xi)}{(1-\gamma)^2} \ . \tag{3.17}$$

The fundamental and higher order force components are found using

$$f_n = 2F_{max}\xi \frac{h_n(\gamma)}{(1-\gamma)^2} \ , \tag{3.18}$$

where

$$h_n(\gamma) = -\gamma\{\mathrm{sinc}[(1+n)\xi] + \mathrm{sinc}[(1-n)\xi]\} + (0.5+\gamma^2)\mathrm{sinc}(n\xi) \\ +0.25\{\mathrm{sinc}[(2+n)\xi] + \mathrm{sinc}[(2-n)\xi]\} \ . \tag{3.19}$$

Equations (3.8) and Eq. (3.12) must be satisfied simultaneously for a cylindrical tip. Similarly, Eq. (3.16) and Eq. (3.18) must be satisfied for a conical tip. We plot $F_{max}/(\beta A_1^\alpha E)$ and F_{max}/f as a function of γ for differing values of E^* and f_1 in Figs. 3.4 and 3.5 for a cylindrical tip and a conical tip. Here, E and $f = \beta A_1^\alpha E$ are the arbitrary values of E^* and f_1. An intersection of the curves gives the solution for γ and F_{max} values for a specific sample and a cantilever.

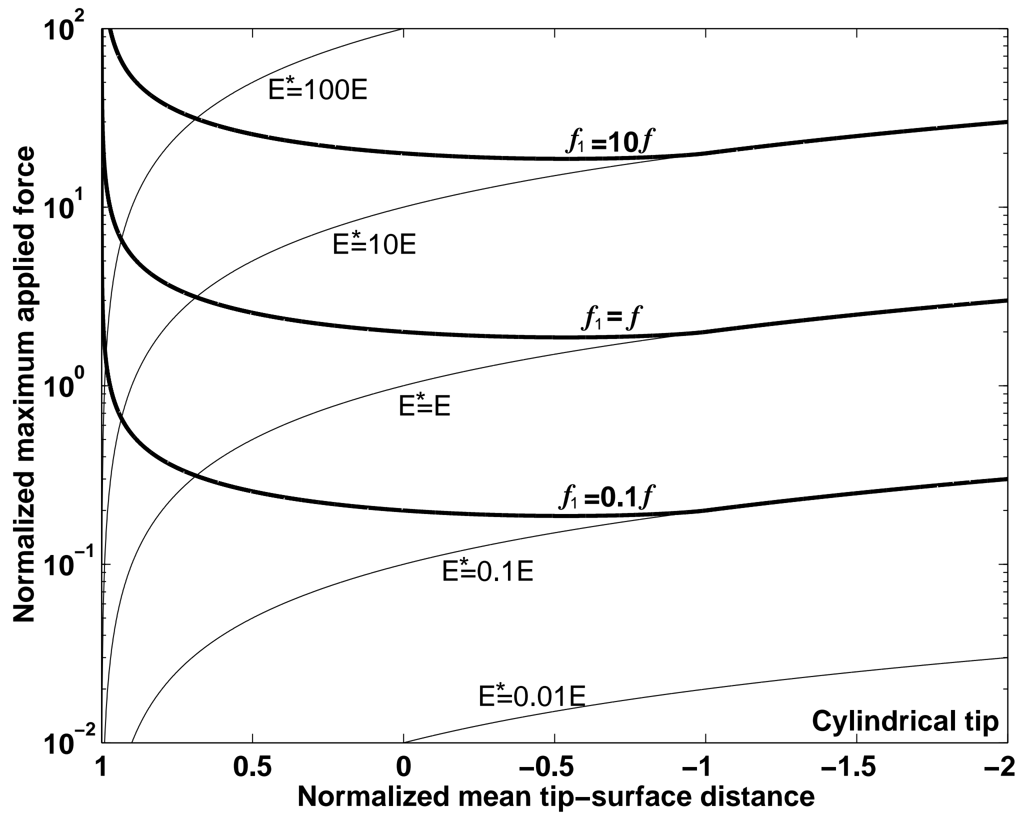

Figure 3.4: Normalized maximum repulsive force $F_{max}/(\beta A_1^{\alpha} E)$ (thin lines) and F_{max}/f (thick lines) are plotted as a function of normalized mean tip-surface distance γ for varying values of E^* and f_1 for a cylindrical tip.

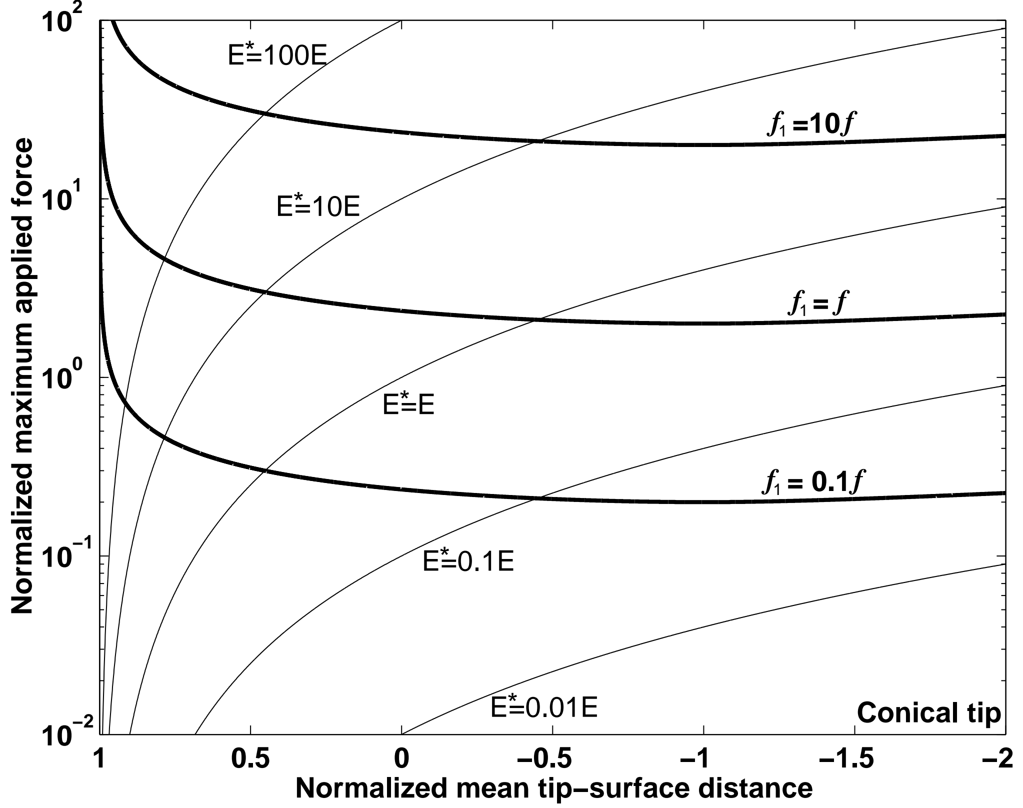

Figure 3.5: Normalized maximum repulsive force $F_{max}/(\beta A_1^{\alpha} E)$ (thin lines) and F_{max}/f (thick lines) are plotted as a function of normalized mean tip-surface distance γ for varying values of E^* and f_1 for a conical tip.

No intersection means that there is no solution for the chosen cantilever. When $\gamma < -1$, it is found that $f_0 = F_{max}\gamma/(\gamma - 1)$, $f_1 = F_{max}/(1-\gamma)$, $f_{n\geq 2} = 0$ for a cylindrical tip and $f_0 = F_{max}(0.5 + \gamma^2)/(1-\gamma)^2$, $f_1 = -2F_{max}\gamma/(1-\gamma)^2$, $f_2 = 0.5F_{max}/(1-\gamma)^2$, $f_{n\geq 3} = 0$ for a conical tip. For a cylindrical tip f_1 is actually equal to $2RE^*A_1$, independent of γ. Therefore, there would not be a damping in the oscillation amplitude as we indent the tip further inside the sample. The only possible solution exists for the sample which gives the effective tip-sample elasticity of $f_1/2RA_1$ as Fig. 3.4 shows. For all other samples, there is an intersection point, unless the tip shape is an infinitely long cylinder. For a conical tip, $f_1 = -4\tan(\theta)E^*A_1^2\gamma/\pi$ increases for decreasing γ and hence there is always an intersection point as Fig. 3.5 shows.

In any case, different sample elastic properties give rise to significantly different F_{max} and γ values. Although we are not able to measure any one of these parameters directly [88], we can extract the sample elasticity by measuring the harmonic amplitudes. Notice that the constant term in Eq. (3.7) depends on γ, but the feedback signal contains information on the height variations of the sample surface also.

3.4 Results and Discussion

We can relate the effective tip-sample elasticity to the nth harmonic amplitude for a cylindrical or conical tip by combining Eqs. (3.8),(3.10) or Eqs. (3.16),(3.18) and utilizing $A_{n\geq 2} = |H(nw)f_n|$ as follows

$$A_n = \begin{cases} |2RA_1H(nw)\xi g_n(\gamma)E^*| & \text{for a cylindrical tip} \\ \\ |(4/\pi)\tan(\theta)A_1^2H(nw)\xi h_n(\gamma)E^*| & \text{for a conical tip} \end{cases} \tag{3.20}$$

There is no direct relation between A_n and E^* in Eq. (3.20). However, ξ or γ can be used as an independent parameter to find respective A_n and E^* values. We can express A_n and E^* in terms of γ only

$$A_n = \left| H(nw)A_1\varsigma(w)|H(w)|^{-1}\Lambda(\gamma) \right| \ , \tag{3.21}$$

where $\Lambda(\gamma)$ is equal to $g_n(\gamma)/[1 - \text{sinc}(2\xi)]$ for a cylindrical tip and $h_n(\gamma)/h_1(\gamma)$ for a conical tip. Also $E^* = f_1/[\beta A_1^\alpha \lambda(\gamma)]$, where $\lambda(\gamma)$ is equal to $\xi[1 - \text{sinc}(2\xi)]$ or $2\xi h_1(\gamma)$ for a cylindrical or conical tip. Notice that as $\xi \to 0$, $\Lambda(\gamma) \to 1$ for which A_n reaches its maximum value $[max(A_n)]$ and $\lambda(\gamma) \to 0$ for which E^* goes to infinity. In Figs. 3.6 and 3.7 we plot first four normalized harmonic amplitudes $[A_n/max(A_n) = |\Lambda(\gamma)|]$ for cylindrical and conical tips as a function of normalized effective tip-sample elasticity $[E^*\beta A_1^\alpha/f_1 = \lambda^{-1}(\gamma)]$ under the assumption of a very small harmonic distortion ($A_n \ll A_1$). In these figures, the dashed vertical line marks the location of a $\gamma = 0$ point.

In region I ($\gamma < 0$), the tip stays in contact more than a half period. Although we are interested in the solution for region II ($\gamma > 0$), we also considered the

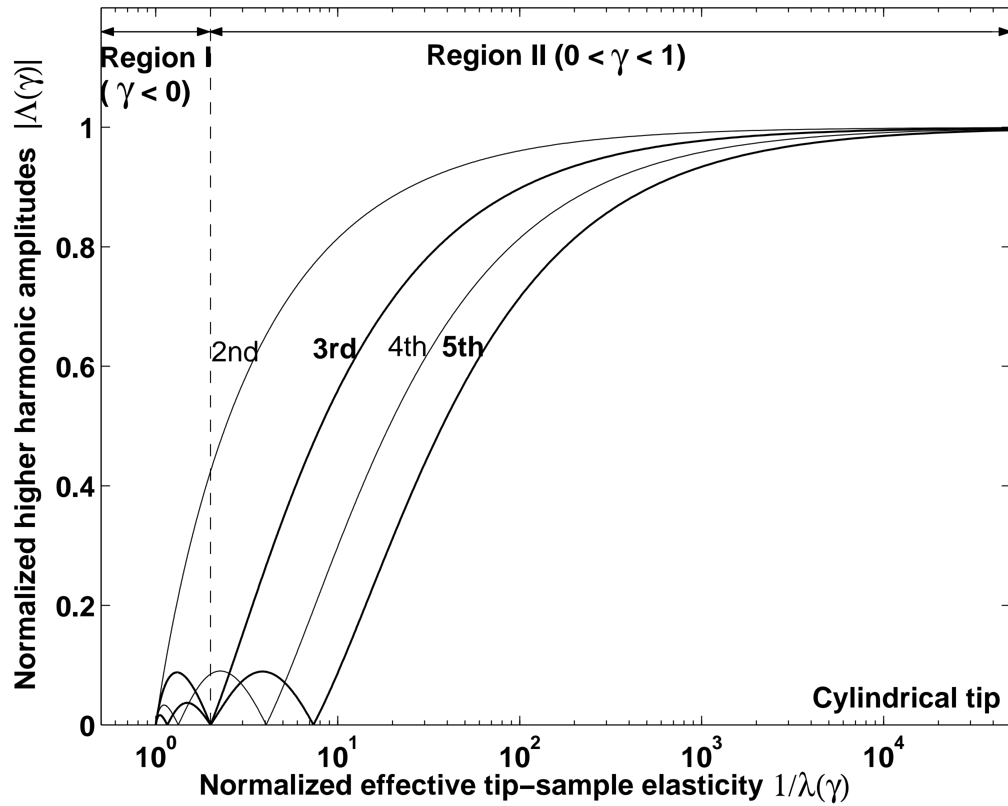

Figure 3.6: A variation of the first four normalized harmonic amplitudes $|\Lambda(\gamma)|$ as a function of normalized effective tip-sample elasticity $\lambda^{-1}(\gamma)$ for a cylindrical tip. It is assumed that $A_n \ll A_1$. The vertical dashed line marks the $\gamma = 0$ location.

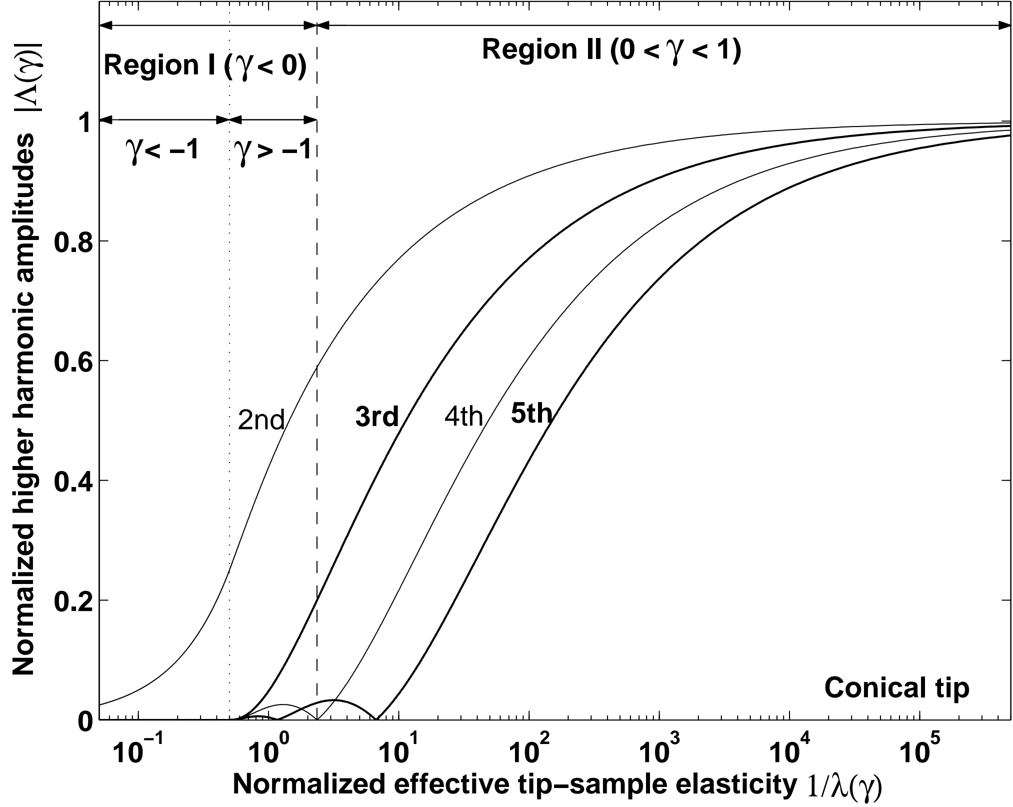

Figure 3.7: A variation of the first four normalized harmonic amplitudes $|\Lambda(\gamma)|$ as a function of normalized effective tip-sample elasticity $\lambda^{-1}(\gamma)$ for a conical tip. It is assumed that $A_n \ll A_1$. Vertical dashed and dotted lines mark the $\gamma = 0$ and $\gamma = -1$ locations.

$\gamma < 0$ case for the completeness. Region I is further decomposed into two parts as $\gamma < -1$ and $\gamma > -1$ in Fig. 3.7. Note that the tip can oscillate even if it is fully indented into the sample [89].

The higher harmonic amplitudes show a monotonic increase in a wide range of sample compliance. Notice that the steeply increasing part of the amplitude curves shift towards high Young's moduli region as the harmonic number increases. This makes one of the higher harmonics more preferable than the other ones depending on the sample. As the sample gets stiffer, A_n saturates since the variation of the contact time (and the penetration depth) gets smaller. This imposes an upper limit for measurable sample elasticity as reported earlier [44].

There is also a lower limit of E^* for which $\gamma > 0$. Both limits can be shifted to the lower side of elasticity by softening the lever, by increasing the set point A_1/A_0 or oscillation amplitude [1], or by using a dull tip. The use of a dull tip is not preferable since it decreases the lateral image resolution. There is a practical maximum value of A_1/A_0 as determined by the precision of the feedback electronics. The oscillation amplitude can have an upper limit. Hence, the cantilever stiffness is the most suitable parameter to adjust the measurement region. The reverse procedure can be applied to shift the operation range to the high elasticity side. Note that changing these parameters also affects the maximum force applied to the surface F_{max}. We recall that the surface forces are assumed to be very small (zero) compared to F_{max} and increasing F_{max} too much can destroy the tip and/or the sample.

[1] This is not applicable for a cylindrical indenter.

Chapter 4

Numerical Analysis for Enhanced Higher Harmonics

Our analytical analysis proves that the harmonic amplitudes can be utilized for mapping sample elasticity. More generally, it can be used to extract a characteristic of the tip-sample force which may be dominated by any type of interaction. In conventional tapping-mode experiments, on the other hand, the higher harmonics are generally ignored and in fact, their amplitudes are two or three orders of magnitude smaller than the fundamental component of oscillation as both numerical [74] and experimental [60] results indicate. The nth harmonic amplitude is related to the nth harmonic of the interaction force f_n via the transfer gain $|H(nw)|$ as follows

$$A_n = |H(nw)f_n| \quad \text{for} \quad n \geq 2 \; , \tag{4.1}$$

The transfer function of a rectangular cantilever including higher flexural eigenmodes was obtained by Stark and Heckl [66].

To increase the nth harmonic amplitude A_n and hence the measurement sensitivity, we must increase either f_n or $|H(nw)|$. Notice that increasing f_n may mean an additional damage to the sample, and therefore it may not be desirable for all kind of samples. The transfer gains for the higher harmonics in conventional tapping-mode operation ($w = w_1$, where w_1 is the resonant frequency of the first

mode) are very small unless the higher harmonic frequencies are coincident with the resonant frequencies of the higher eigenmodes. If we consider only the fundamental eigenmode of a cantilever with stiffness of k, the transfer gain for the nth harmonic will be $[k(n^2 - 1)]^{-1}$. This yields a very small value for increasing n. The use of higher harmonics close to the higher transverse resonances can enhance the measurement sensitivity [90]. However, to increase the amplitudes of higher harmonics in this case, one may need to increase the free oscillation amplitude or decrease the set point (damped) amplitude which in turn increases the tip-sample forces.

Most cantilevers do not have eigenmodes at integer multiples of each other. But, it is possible to fabricate special cantilevers, called "harmonic cantilevers", in such a way that one of the eigenmodes is at an integer multiple of fundamental mode [91]. The recent study by Sahin *et al.* showed that these cantilevers can be used to enhance one of the higher harmonics [92].

Indeed, measuring the higher harmonic signal sensitively would give an opportunity to researchers in examining the material properties at the nanoscale more effectively. To enhance the quality of the measured harmonic signal, we propose a new method which can easily be employed in conventional tapping-mode systems.

4.1 Higher Harmonic Enhancement

Considering the fundamental eigenmode, the transfer gain reaches its maximum value (Q/k, where Q is the quality factor) at the first resonance frequency w_1. If we drive the cantilever at a submultiple of w_1, i.e. at $w = w_{1n} = w_1/n$ (n is an integer number), then, due to the high transfer gain at $nw_{1n} = w_1$, the nth harmonic amplitude is expected to be much larger than the conventional case. This allows us to detect the harmonic signal with a good signal-to-noise ratio and to inspect the tip-sample interaction effectively. The concept of harmonic enhancement is shown in Fig. 4.1, where the third harmonic is matched to a flexural eigenmode of the cantilever.

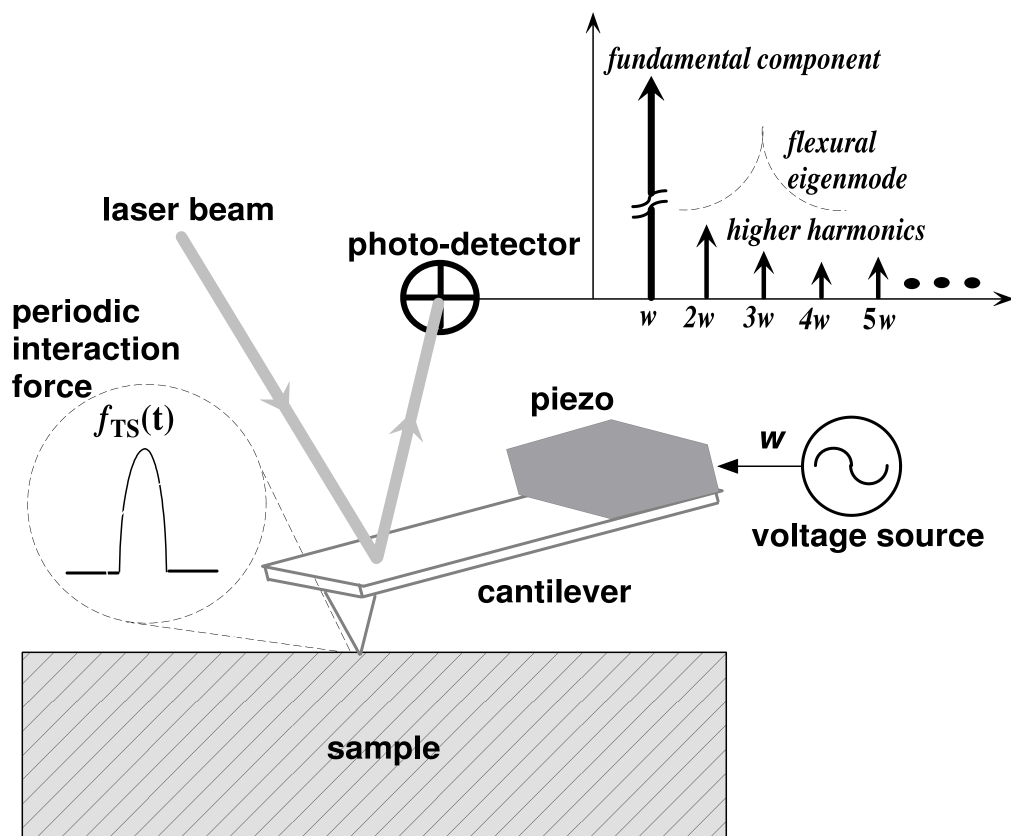

Figure 4.1: Higher harmonic enhancement by matching to a flexural resonance.

To vibrate the cantilever at w_{1n} with a reasonable amplitude, a higher driving force must be applied since there is no Q enhancement for the fundamental component of the oscillation. In order to investigate if the proposed method can be helpful for differentiating the stiffness of materials and to analyze the effect of the method on the dynamics of tip-sample system, we performed numerical simulations.

4.2 Simulation Details

The simulations are done by converting the mechanical point-mass model into an equivalent electrical circuit [93] containing nonlinear elements. The equivalent circuit is simulated with SPICE, a powerful and easily available circuit simulator. The simulation setup and the relation between electrical and mechanical model parameters are shown in Fig. 4.2. The tip position is subtracted from the sample position to obtain the tip-surface separation. The tip-sample force $f_{\mathbf{TS}}$ is obtained by introducing the parameters of tip shape and effective tip-sample elasticity.

The simulations are done in time domain with a step size of one thousandth of one period. To make sure that the steady state is reached, $10Q$ oscillation cycles are simulated. We choose a typical cantilever with a stiffness of $k = 1$ N/m, a quality factor of $Q = 100$, and a fundamental resonance frequency of $w_1 = 2\pi\times 120$ krad/s. The free oscillation amplitude A_0 and set point amplitude A_1 are chosen to be $A_0 = 100$ nm and $A_1 = 0.99A_0$.

We considered the Hertzian contact mechanics in our simulations to find how the enhanced higher harmonics change with sample elasticity. The tip end is approximated with a paraboloidal (spherical) shape having a radius of curvature R. Hence, the parameters defining the tip geometry will be $\beta = 4\sqrt{R}/3$ and $\alpha = 3/2$. In the simulations R is selected to have a typical value of 10 nm.

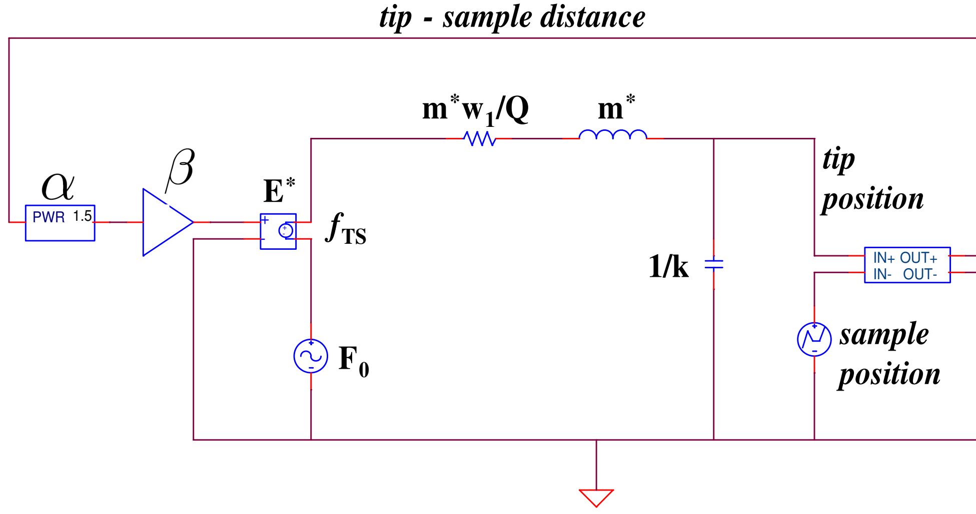

Figure 4.2: Electrical equivalent of mechanical point-mass model.

4.3 Simulation Results

We analyzed in detail the response of the enhanced second and third harmonic signals as a function of the effective tip-sample elasticity E^*, when the cantilever is driven at the submultiple frequencies of $w = w_{12} = w_1/2$ and $w = w_{13} = w_1/3$. Figure 4.3 shows the variation of normalized second (A_2/A_0) and third (A_3/A_0) harmonic amplitudes with E^*. This figure is divided into two regions by a dashed vertical line. In region I, the tip stays in contact with sample more than a half oscillation period, whereas in region II the contact time is less than a half period. The first observation is that the magnitude of the second harmonic signal can reach almost 40 % of the fundamental component. Secondly, it is seen that the higher harmonic amplitudes are increasing monotonically in a certain range of sample stiffness. The second harmonic amplitude is larger than the third harmonic amplitude and the steeply increasing part of the second harmonic amplitude is at a lower elasticity region compared to the third harmonic. Finally, we find that the tip motion can show chaotic behavior at a relatively high elasticity region (marked by a dotted line).

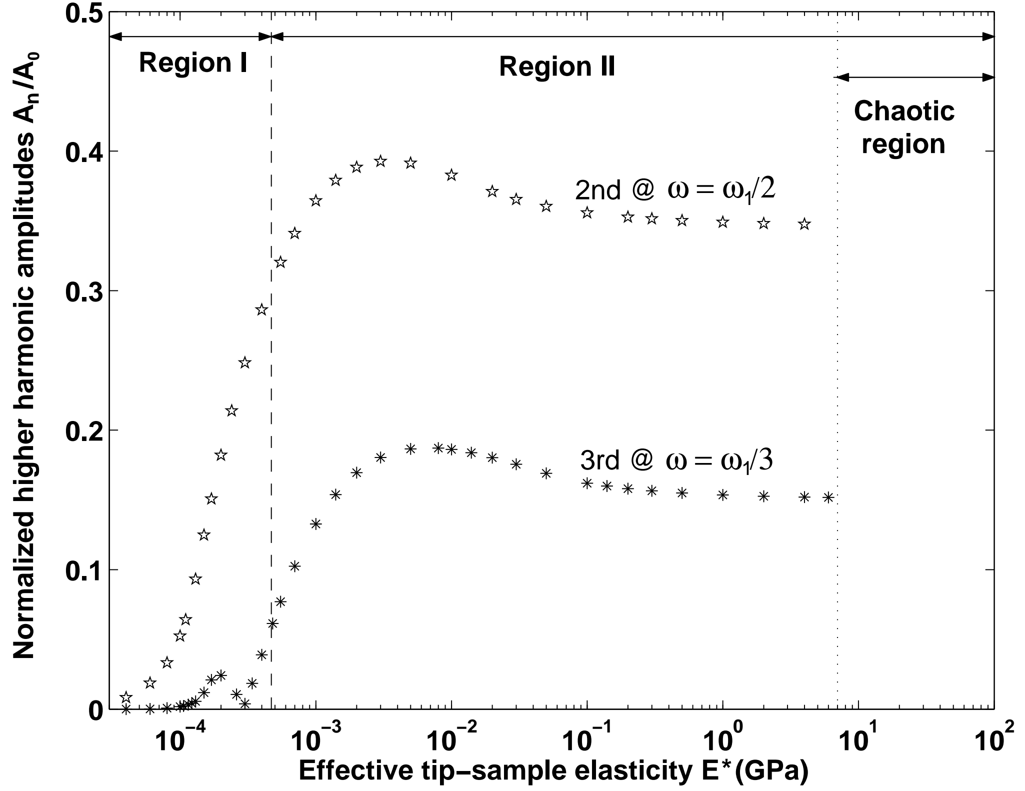

Figure 4.3: Simulation results for the second and third harmonics when the cantilever is driven at $w = w_1/2$ and $w = w_1/3$, respectively. A_2/A_0 (stars) and A_3/A_0 (asterisks) are plotted for a paraboloidal tip with a radius of curvature $R = 10$ nm. The simulation parameters are $A_0 = 100$ nm, $A_1/A_0 = 0.99$, $Q = 100$, and $k = 1$ N/m. A vertical dashed line separates the region I ($\gamma < 0$) and region II ($\gamma > 0$), whereas the dotted line indicates the beginning of chaotic region for the third harmonic. Those locations for the second harmonic are very close to these lines and not shown for clarity.

The phase of the cantilever oscillation can be used to map energy dissipation [59–61]. On the other hand, it can not be used to differentiate the compliance of purely elastic samples [65]. In such a case, the enhanced harmonic signal can be useful to increase the image contrast. To map the sample elasticity, the harmonic amplitude variations should be monotonic in a range which covers Young's moduli of the materials under investigation. If we consider region II, it is seen that the samples which have different compliance may not be differentiated and the contrast in the images can not be interpreted uniquely because of the nonmonotonic variations. Furthermore, there are no steady-state values of harmonic amplitudes for relatively stiff samples due to chaotic system response.

We used a time series analysis software TISEAN [94] to find the largest Lyapunov exponent which indicates whether the system is chaotic or not [95]. The possibility of chaotic system behavior in conventional tapping-mode AFM was predicted by Hunt and Sarid [96]. The numerical analysis by Stark [97] also showed that chaos can occur depending on the tip-sample gap as the higher harmonics are enhanced by the higher eigenmodes. We provided the phase portraits for different cases below. The chaotic behavior is seen in Figure 4.4 (d).

To gain further insight on the dynamics of the system response, we provided one cycle of tip position graph as obtained from the simulations for three different samples in Fig. 4.5. It is seen that as the sample gets stiffer, the tip motion deviates heavily from the sinusoidal shape. We can also write the power balance equation to find the relation between A_n and the system variables. The power input to the system is [61] $kw_{1n}A_dA_1\sin(\phi)/2$, where A_d and ϕ are the drive amplitude and the phase shift between the drive and displacement signals. This power is dissipated partly by the fundamental component of tip oscillation $[kw_{1n}^2A_1^2/(2Qw_1)]$ and partly by the enhanced higher harmonic $[kw_1^2A_n^2/(2Qw_1)]$. Because, we assumed that there is no energy dissipation in the sample and the other (unmatched) higher harmonics are negligible (as obtained from simulations) since A_1/A_0 is set very close to 1. From this balance one can find A_n in terms of ϕ as

$$A_n = (A_1/n)[Q(n - 1/n)(A_0/A_1)\sin(\phi) - 1]^{1/2} \,. \tag{4.2}$$

In this formulation, we used $A_d \cong (1 - w^2/w_1^2)A_0$ which is valid for a high-Q

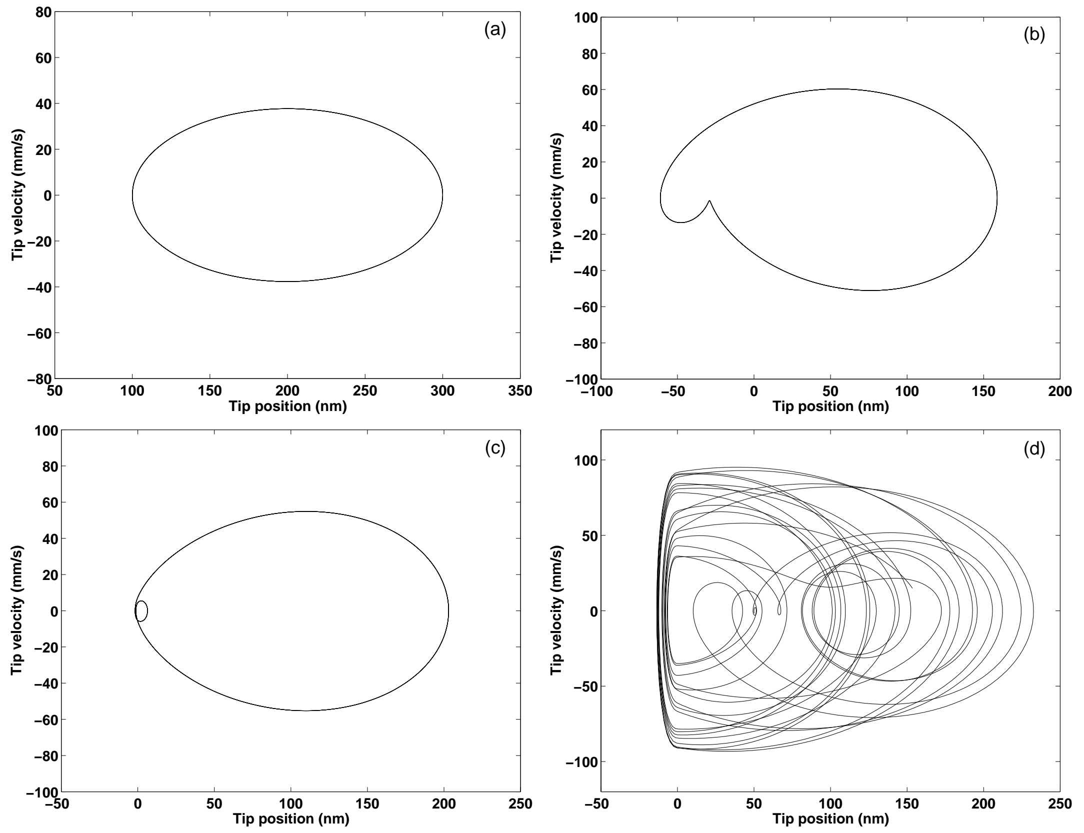

Figure 4.4: Phase diagrams for four different elastic samples with $w = w_{12}$ and $w_1 = 2\pi\times 120$ krad/s. (a) Free, (b) $E^* = 1$ MPa, (c) $E^* = 1$ GPa, and (d) $E^* = 6$ GPa. Ten oscillation cycles are plotted in each graph.

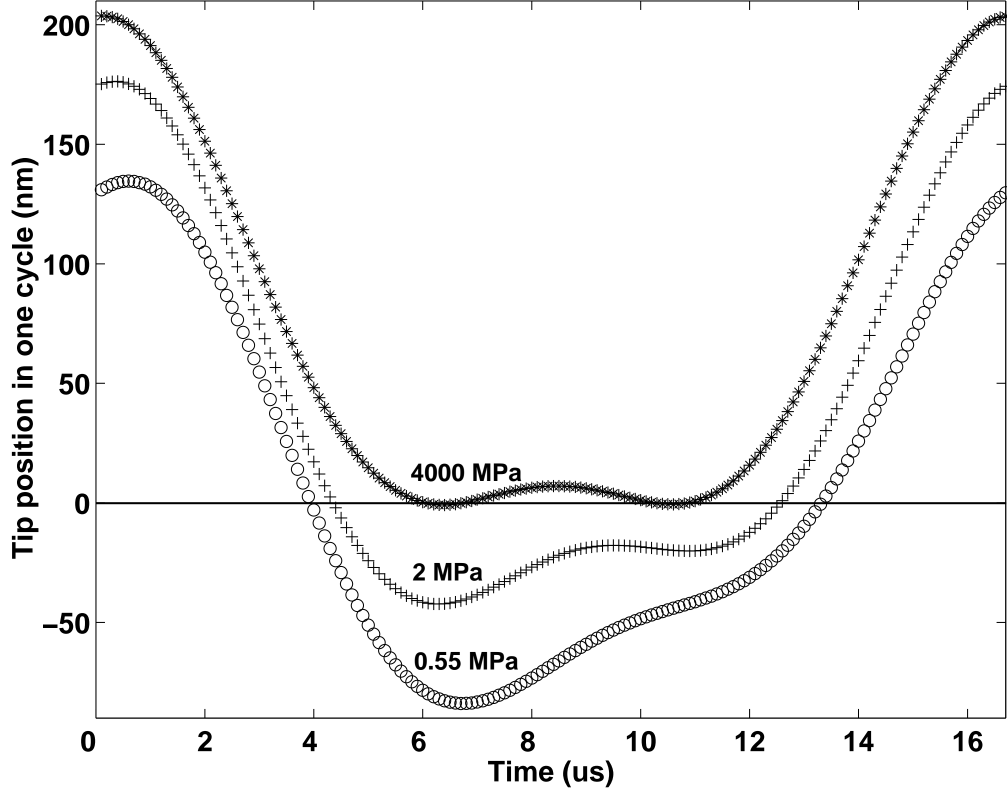

Figure 4.5: Tip motions taken from simulations for three different elastic samples when the cantilever is excited at $w = w_1/2$. The position of the undeformed sample surface is indicated by the horizontal line.

cantilever excited at $w \leq w_1/2$. It is found that A_n and ϕ depends on each other. We observed in simulations that ϕ initially increases and after a peak value it decreases as the sample gets stiffer. This explains the nonmonotonic behavior seen in Fig. 4.3. Equation (4.2) also helps to explain the observed amplitude differences in second and third harmonics. For a given w_1, as n increases the energy input decreases which in turn limits the amplitude of the nth harmonic.

If the higher harmonic signal A_n becomes a significant fraction of A_0, the relation between A_n and the sample stiffness is no longer monotonic. Moreover, cantilever can get into chaotic motion if the sample stiffness is very high. To avoid these problems, the enhancement can be reduced by choosing an excitation frequency that is slightly different than the submultiple frequency.

We performed the simulations at slightly shifted excitation frequencies and plotted the results in Fig. 4.6. For the second harmonic we drive the cantilever at $w = 0.98w_{12}$ and for the third harmonic we selected $w = 0.97w_{13}$. It is seen that the variations become monotonic in region II and the chaotic behavior is eliminated (see Fig. 4.7). The amplitudes saturate for increasing sample stiffness. The saturated amplitudes of second and third harmonics are still more than 15% of A_0 which gives a very good sensitivity. To make a comparison between the harmonic amplitudes of the conventional mode of operation, where the cantilever is excited at $w = w_1$, we performed more simulations and plotted the results in the same figure. We find that the second and third harmonic amplitudes in the conventional case are not more than 0.3% of A_0.

The force applied by the tip on the surface must be carefully chosen for imaging delicate samples. For the same cantilever and tip shape, the parameters that affect the interaction force are the driving frequency [98, 99] w, free oscillation amplitude A_0, and the set point ratio A_1/A_0. The effect of A_1/A_0 is shown in Figure 4.8. The fundamental component of the tip-sample interaction force f_1 reaches its minimum value at a frequency slightly less than the resonance frequency [32]. To enhance the second harmonic, we excite the cantilever at $0.98w_{12}$. A_0 and A_1/A_0 are selected to be 100 nm and 0.99. For the selected parameters, we found that the maximum value of the interaction force is less than 18 nN for the elasticity of samples less than 10 GPa. As a comparison, the maximum applied force is found to be less than 17.6 nN in conventional tapping mode operation ($w = w_1$) with the parameters of $A_0 = 100$ nm and $A_1/A_0 = 0.6$ and for the same range of sample elasticity. Note that the force applied to the surface in conventional case will be less than 5.5 nN if we select $A_1/A_0 = 0.99$, in which case the higher harmonic amplitudes will be less than 0.05% of A_0. Here, we selected A_1/A_0 to be 0.6 to make a fair comparison between the higher harmonic amplitudes of two cases. Hence, we conclude that higher harmonic amplitudes of the proposed method are much larger than that of conventional case even though the same forces are applied to the surface.

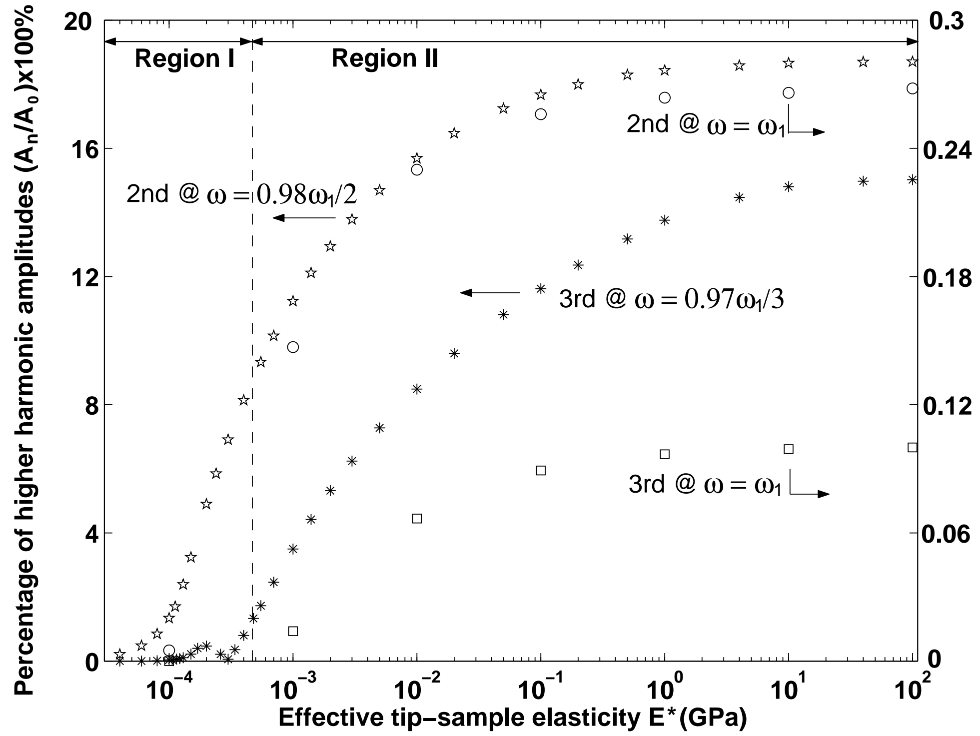

Figure 4.6: Left-hand axis: Simulation results for A_2 ($w = 0.98w_1/2$) marked by stars and A_3 ($w = 0.97w_1/3$) marked by asterisks in the percentage of A_0 with the same parameters of Figure 4.3. The vertical dashed line indicates the $\gamma = 0$ location. Right-hand axis: Simulation results for the conventional case ($w = w_1$). A_2 is marked by circles and A_3 is marked by rectangles in the percentage of A_0 at $A_1/A_0 = 0.6$. The other parameters are the same.

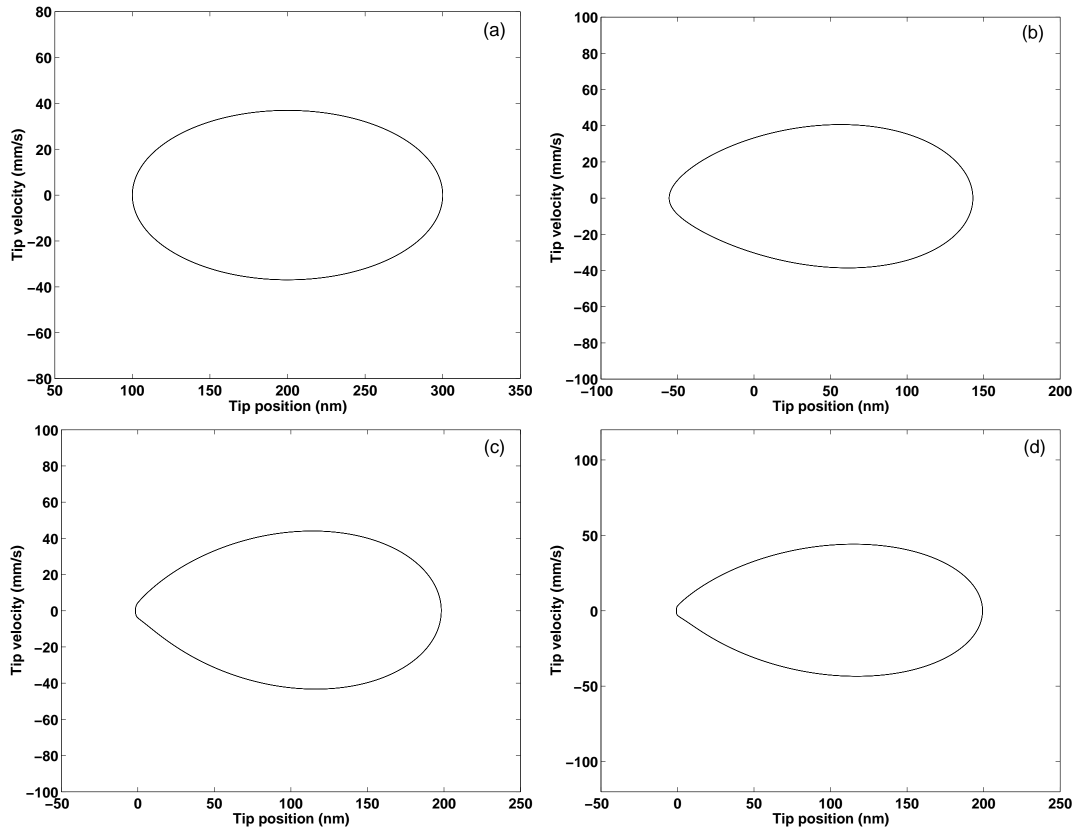

Figure 4.7: Phase diagrams for the same cases of Fig. 4.4 at $w = 0.98w_{12}$. (a) Free, (b) $E^* = 1$ MPa, (c) $E^* = 1$ GPa, and (d) $E^* = 6$ GPa. Ten oscillation cycles are plotted in each graph.

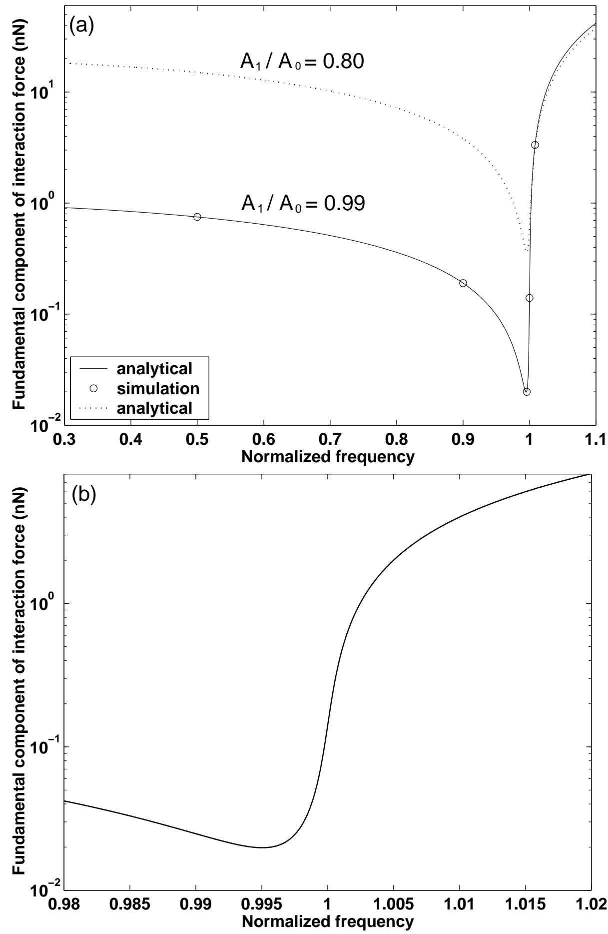

Figure 4.8: (a) Fundamental component of interaction force as a function of normalized frequency w/w_1 for two different set points. (b) A close looking around the resonance frequency for $A_1/A_0 = 0.99$.

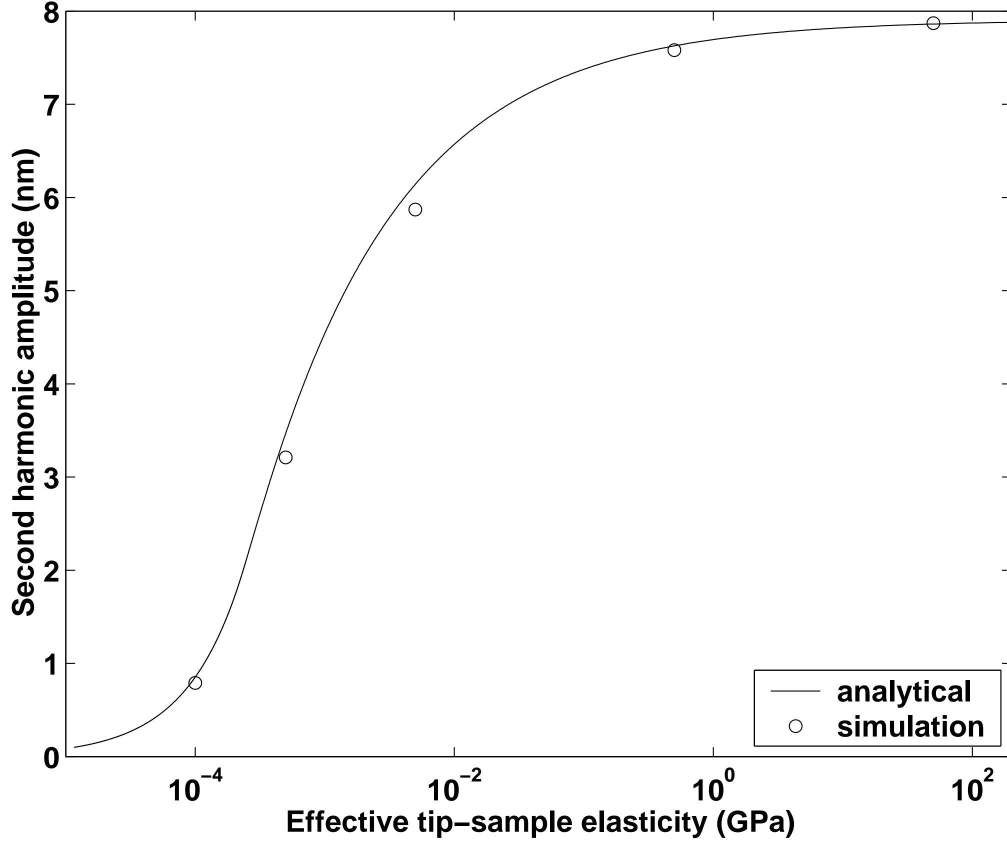

Figure 4.9: The variation of the second harmonic amplitude A_2 as a function of effective tip-sample elasticity E^* at $w = 0.95w_1/2$ and $A_1/A_0 = 0.99$.

4.4 Comparison to Analytical Solution

We compared our analytical solution to the numerical simulation results at three different driving frequencies and for five different samples. To make a comparison, we used a conical tip of semivertical angle $\theta = 15^o$. Figure 4.9 shows the results for $w = 0.95w_1/2$ case. It is seen that the simulation results match the analytical solution almost perfectly even though the second harmonic amplitude can be as large as 8% of A_0.

To make a more precise evaluation, we provided the tip position and tip-sample force in one period for each sample in Fig. 4.10 (a)-(e). In this figure

the solid lines show the analytical solutions whereas the dashed lines indicate the simulation results.

Note that the interaction force is multiplied by 10 to fit into the figure. It is seen that for soft samples, like in (e), the analytical solutions match perfectly the simulation results. For stiffer samples, like in (a), there is a small difference due to enhanced second harmonic. We plotted the maximum applied force as a function of normalized mean tip-surface distance in Fig. 4.11. This figure also shows that the simulation results deviate slightly from the analytical solutions as the sample gets stiffer (as the second harmonic amplitude increases).

We carried out the same comparison between the simulation results and analytical solutions in Figs. 4.12-4.14 for $w = 0.98w_1/2$ and in Figs. 4.15-4.17 for $w = w_1$. For $w = 0.98w_1/2$ case the disagreement is more than the previous case. But, notice that in this case the second harmonic amplitude exceeds 18% of A_0.

On the other hand, for $w = w_1$ case an excellent agreement is obtained between the simulations an analytical solutions. The reason is obvious that the second harmonic amplitude is not more than 0.2% of A_0 (very low harmonic distortion) as usual in conventional tapping-mode operation. Note also that for this case we choose the set point as $A_1/A_0 = 0.8$ which is typically selected in tapping-mode experiments. If we select the set point as $A_1/A_0 = 0.99$, then the harmonic distortion will be less than the present case.

In summary, we showed that the analytical results are valid for small harmonic distortion case, which is a typical situation in conventional tapping-mode experiments. As the harmonic amplitudes increase, the analytical solutions start to deviate from the simulation results. There is a slight deviation for the case of $w = 0.98w_1/2$, but notice that the second harmonic amplitude is two orders of magnitude larger than the case of $w = w_1$. Moreover, the variation is monotonic and therefore the enhanced second harmonic amplitude can still be utilized to map sample elasticity.

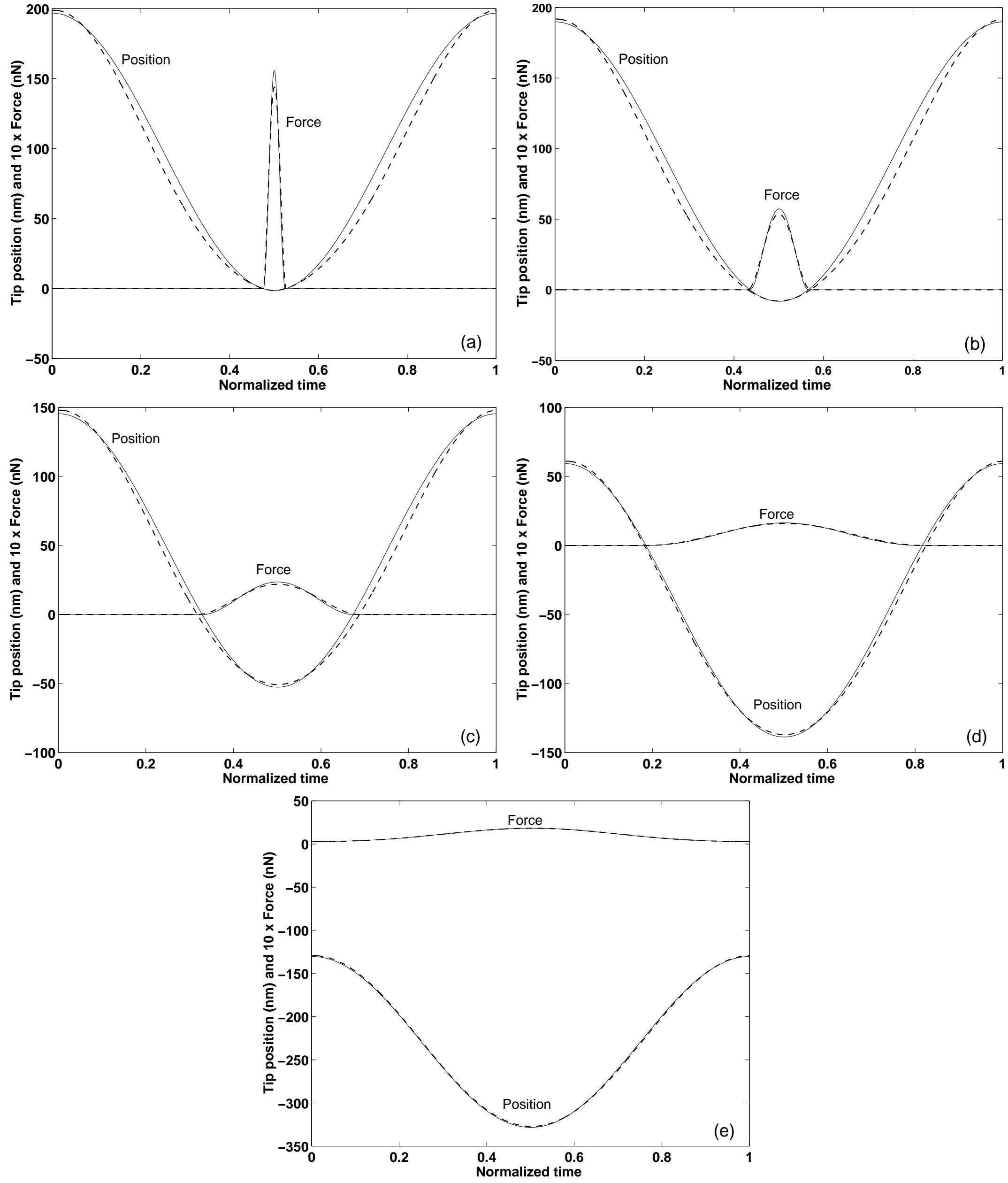

Figure 4.10: Tip position and 10×Force in one oscillation cycle. Simulation results are shown by thick dashed lines and analytical solutions are shown by thin solid lines at $w = 0.95w_1/2$ and $A_1/A_0 = 0.99$. (a) $E^* = 50$ GPa, (b) $E^* = 0.5$ GPa, (c) $E^* = 5$ MPa, (d) $E^* = 0.5$ MPa, and (e) $E^* = 0.1$ MPa.

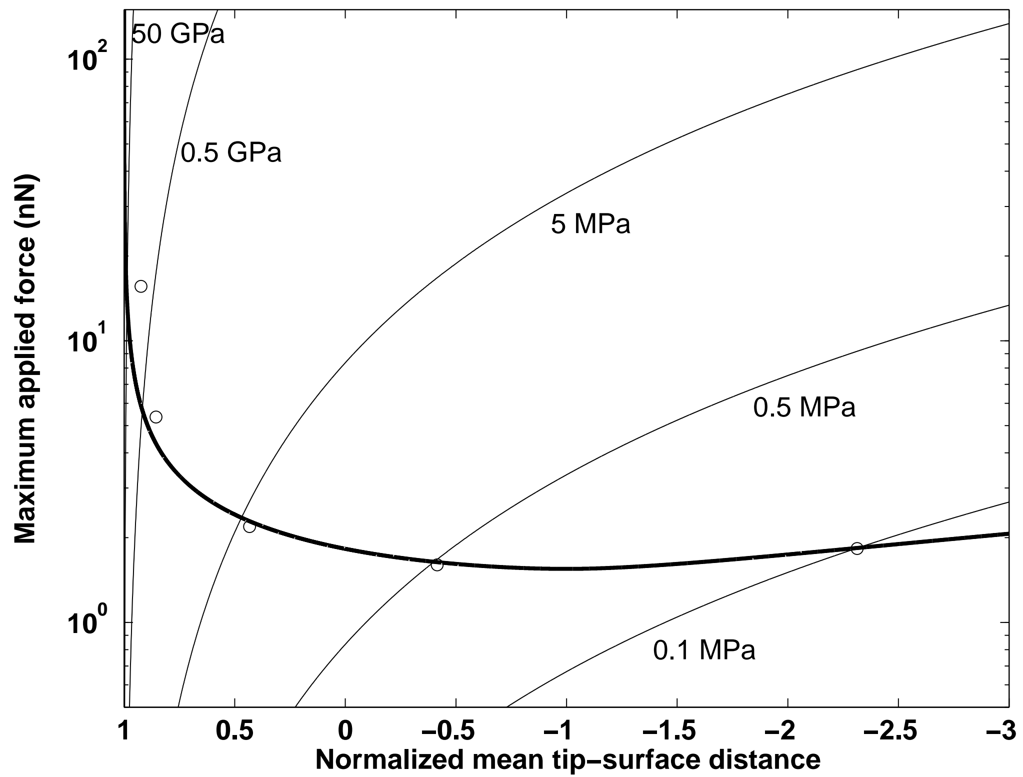

Figure 4.11: Maximum applied force versus normalized mean tip-surface distance. Analytical solutions (the intersection points of solid lines) and the simulation results (circles) at $w = 0.95w_1/2$ and $A_1/A_0 = 0.99$ for different samples.

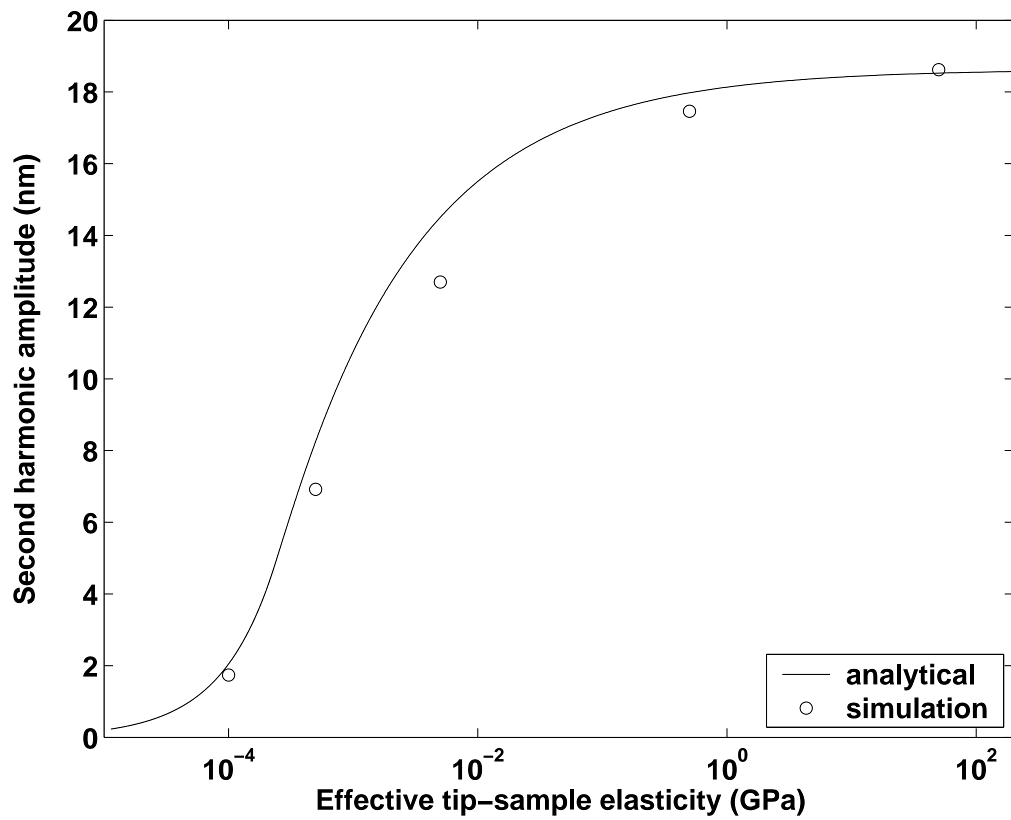

Figure 4.12: The variation of the second harmonic amplitude A_2 as a function of effective tip-sample elasticity E^* at $w = 0.98w_1/2$ and $A_1/A_0 = 0.99$.

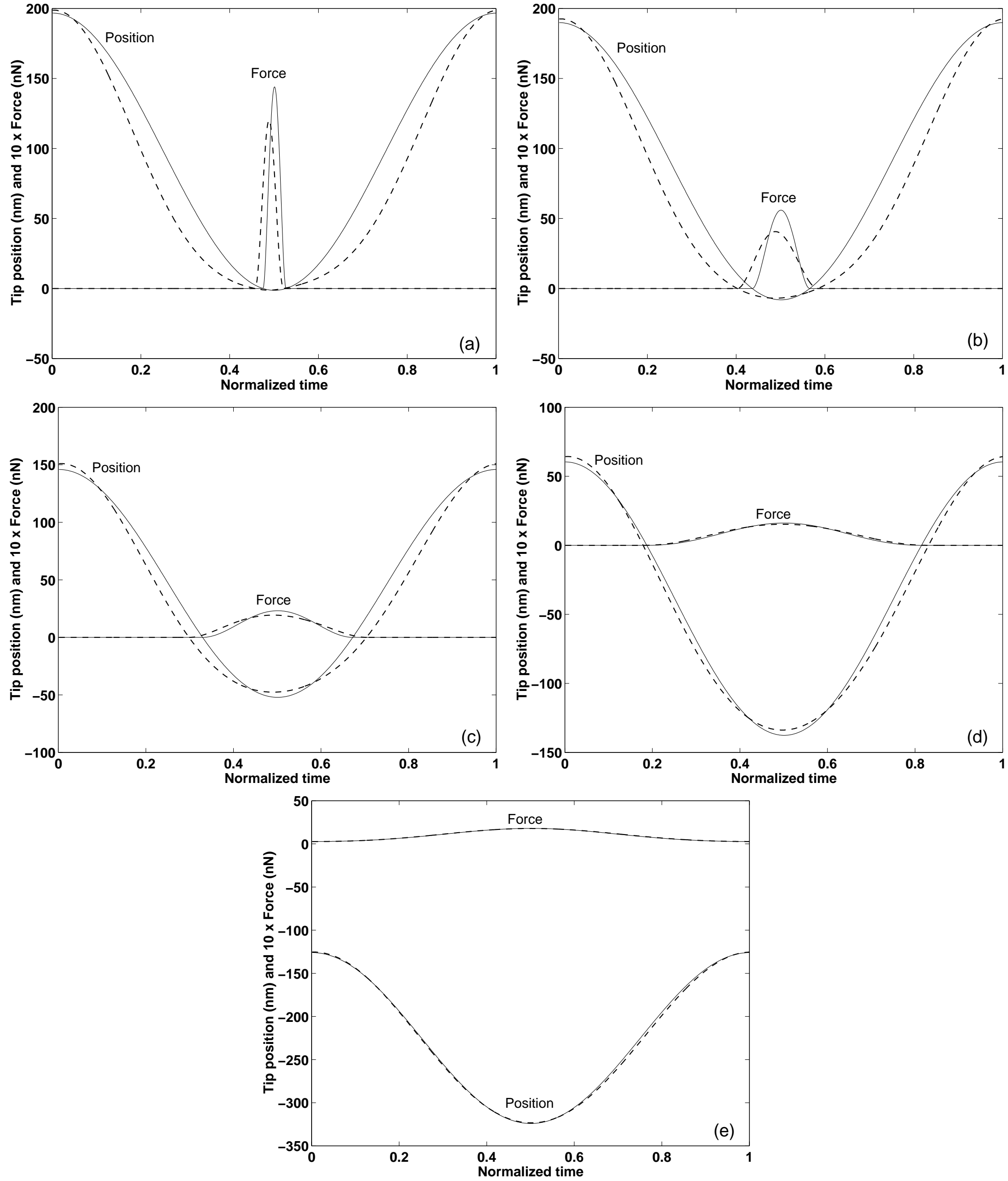

Figure 4.13: Tip position and 10×Force in one oscillation cycle. Simulation results are shown by thick dashed lines and analytical solutions are shown by thin solid lines at $w = 0.98w_1/2$ and $A_1/A_0 = 0.99$. (a) $E^* = 50$ GPa, (b) $E^* = 0.5$ GPa, (c) $E^* = 5$ MPa, (d) $E^* = 0.5$ MPa, and (e) $E^* = 0.1$ MPa.

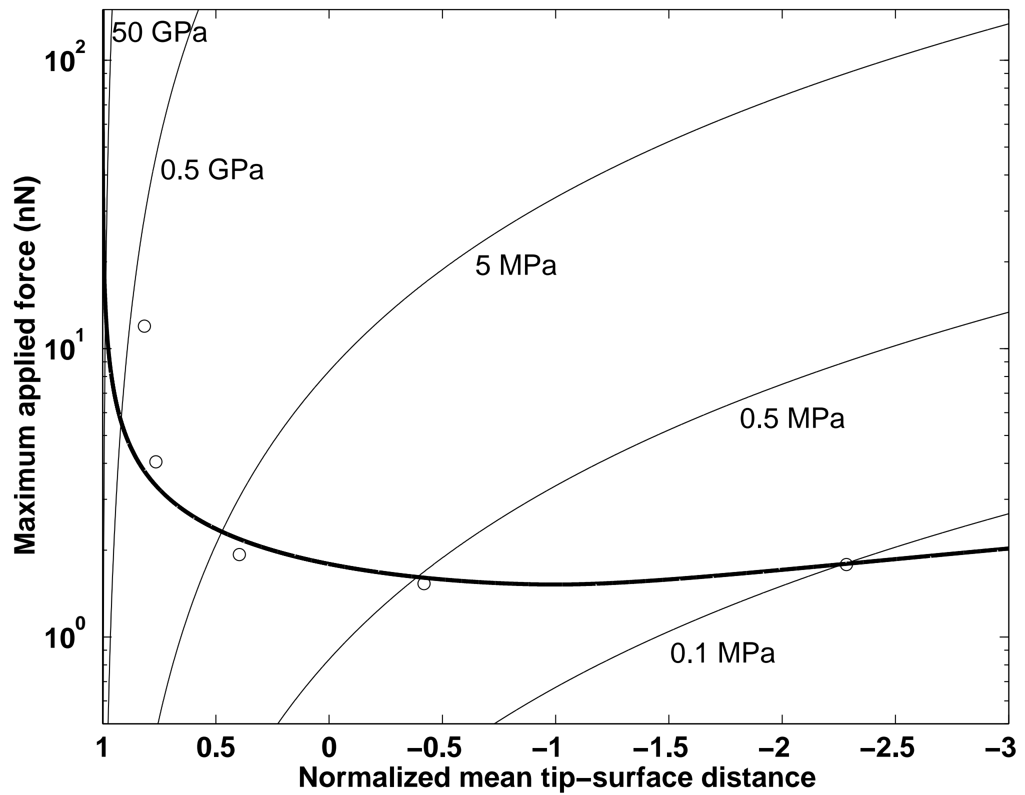

Figure 4.14: Maximum applied force versus normalized mean tip-surface distance. Analytical solutions (the intersection points of solid lines) and the simulation results (circles) at $w = 0.98w_1/2$ and $A_1/A_0 = 0.99$ for different samples.

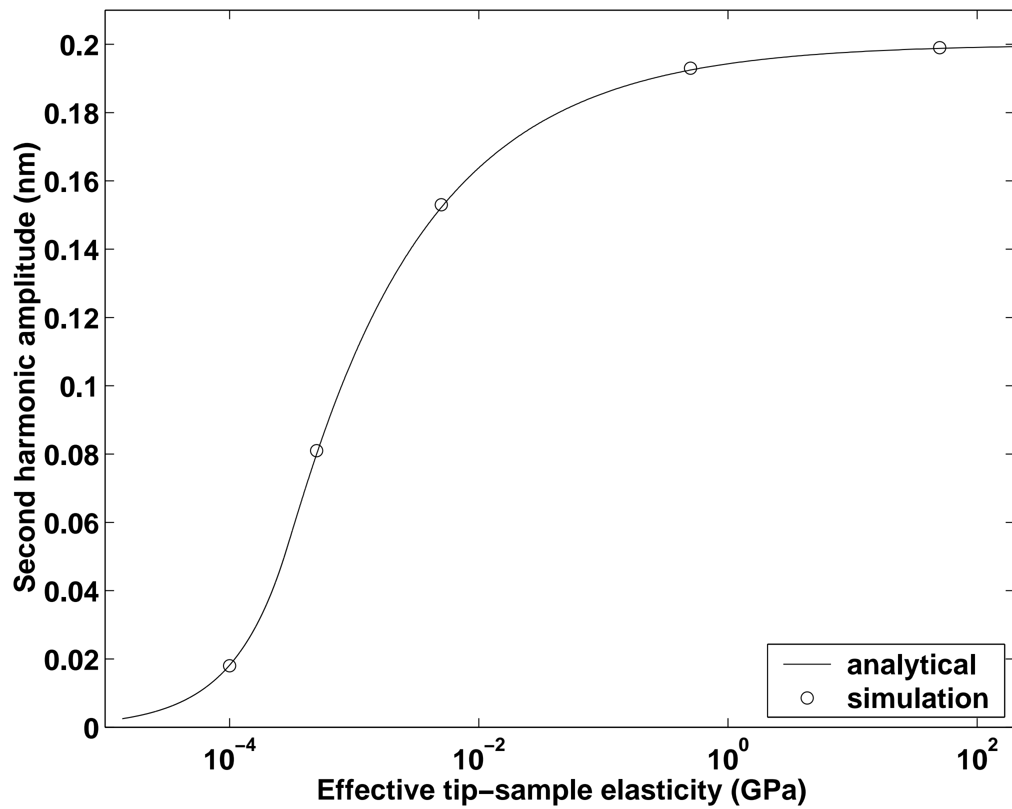

Figure 4.15: The variation of the second harmonic amplitude A_2 as a function of effective tip-sample elasticity E^* at $w = w_1$ and $A_1/A_0 = 0.8$.

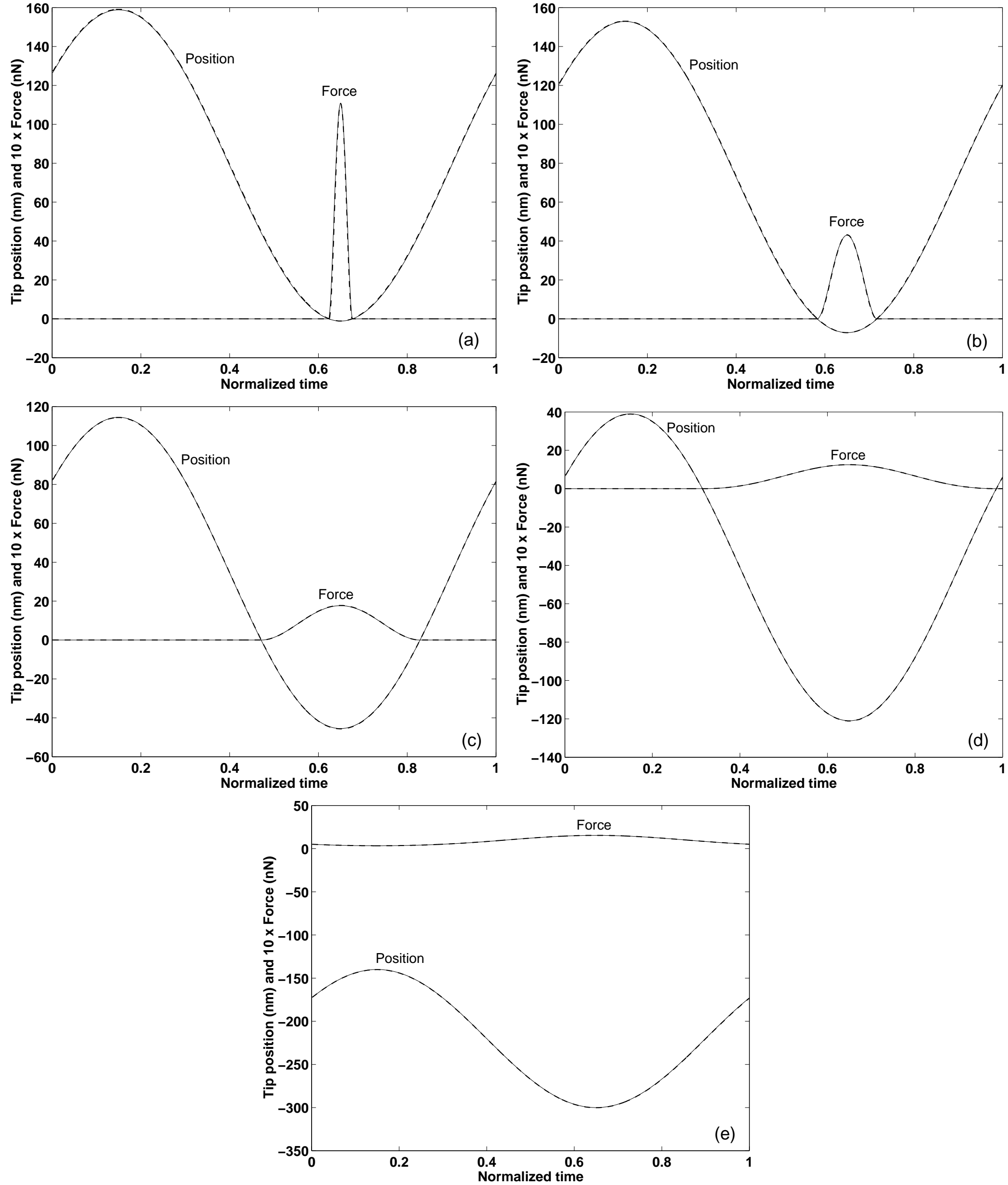

Figure 4.16: Tip position and 10×Force in one oscillation cycle. Simulation results are shown by thick dashed lines and analytical solutions are shown by thin solid lines at $w = w_1$ and $A_1/A_0 = 0.8$. (a) $E^* = 50$ GPa, (b) $E^* = 0.5$ GPa, (c) $E^* = 5$ MPa, (d) $E^* = 0.5$ MPa, and (e) $E^* = 0.1$ MPa.

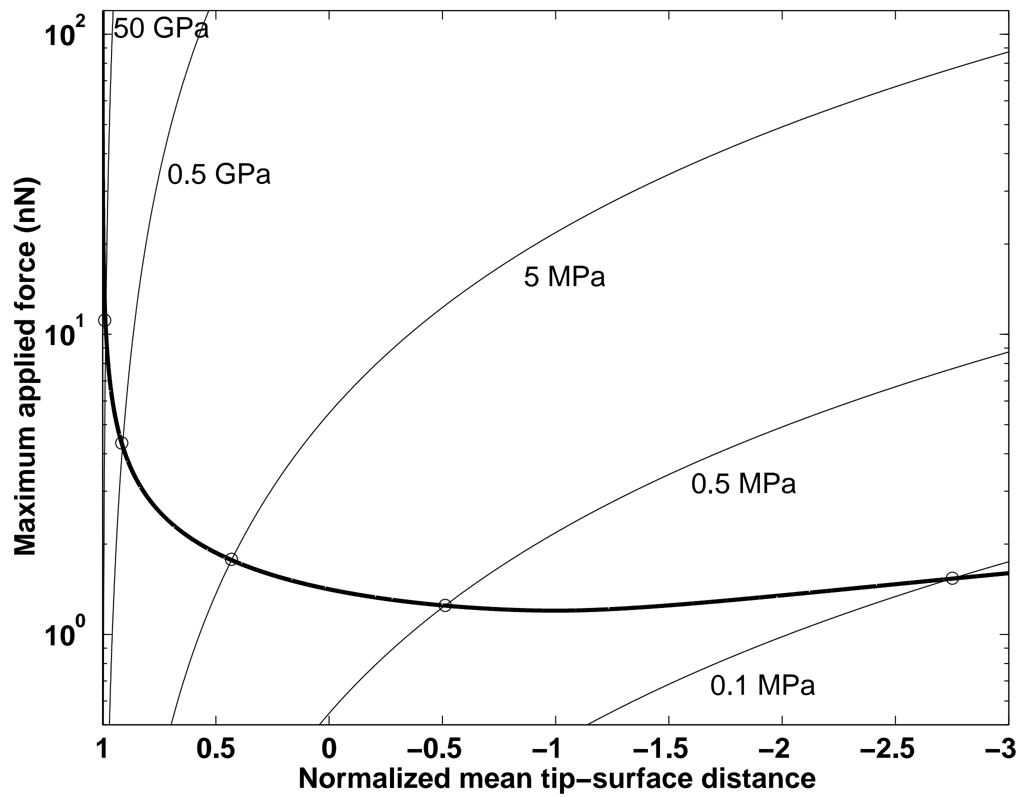

Figure 4.17: Maximum applied force versus normalized mean tip-surface distance. Analytical solutions (the intersection points of solid lines) and the simulation results (circles) at $w = w_1$ and $A_1/A_0 = 0.8$ for different samples.

Chapter 5

Experimental Setup

A schematic description of the experimental setup is shown in Fig. 5.1. An optical lever detection scheme [21] is employed in our AFM. Namely, a laser beam is positioned onto the cantilever, and the reflected laser beam is detected by a four-quadrant photo-detector. The cantilever base is excited by applying a sinusoidal voltage to the tapping piezo. A piezotube is used to scan the sample surface. It also moves the sample up and down in accordance with the feedback signal.

5.1 Instruments

We used two lock-in amplifiers, two synchronized signal generators, and a controller to perform the experiments. The first signal generator (Model DS345, Stanford Research Systems, Sunnyvale, CA) excites the cantilever at close to w_1/n and provides a reference signal for the first lock-in amplifier (Model SR830, Stanford Research Systems, Sunnyvale, CA) which measures the fundamental oscillation amplitude. The output of the first lock-in amplifier is fed back to the controller (NanoMagnetics Instruments Ltd., UK) which adjusts the vertical position of the piezotube. The second signal generator of the same model is used to provide a reference signal at close to w_1 to the second lock-in amplifier (Model SR844, Stanford Research Systems, Sunnyvale, CA) which measures the

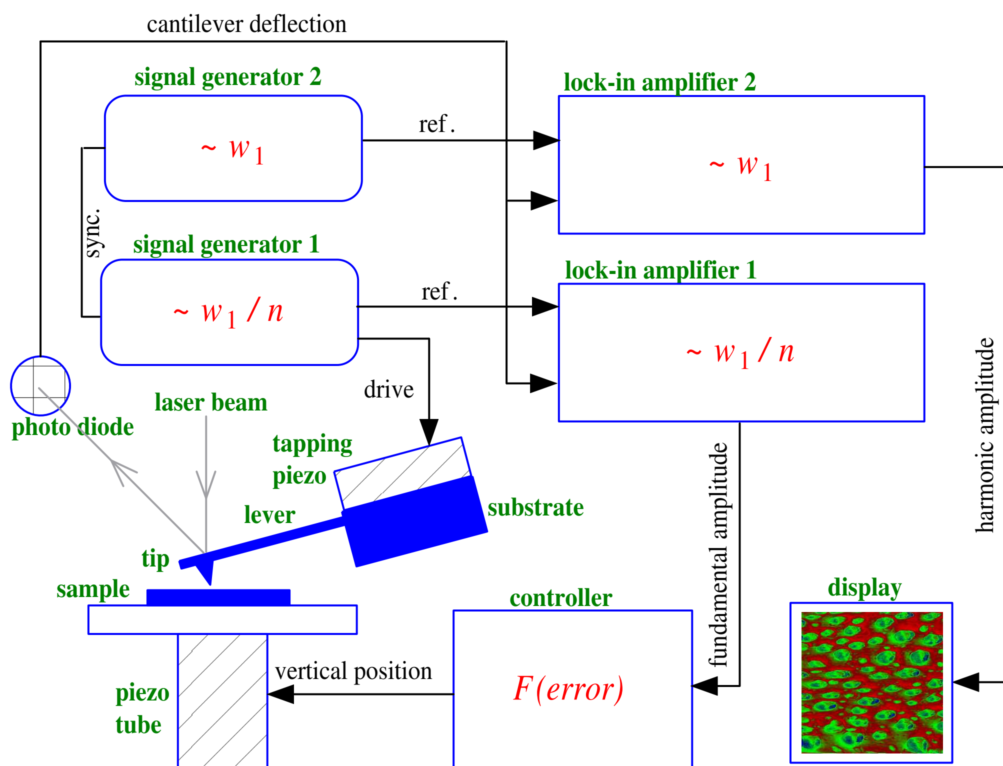

Figure 5.1: Schematic experimental setup.

nth harmonic amplitude.

To make a comparison, we also performed conventional tapping-mode experiments. In those cases, second signal generator and the first lock-in amplifier are not used. The first signal generator again drives the tapping piezo and provides a reference signal to the second lock-in amplifier which measures the fundamental amplitude. Therefore the input of the controller is connected to the output of the second lock-in amplifier. The reason of this change is simply that the first lock-in can measure up to 100 kHz whereas the second one can measure up to 200 MHz.

5.2 Measurement Cantilever

We used a single cantilever (Model No. MPA-11100, NanoDevices, Santa Barbara, CA) throughout the experiments. The scanning electron microscope (SEM) micrographs of the cantilever (after the experiments) are shown below. A contamination at the tip end seen in Fig. 5.4 (b) is probably a piece of photoresist left from the last experiment.

The dimensions of the cantilever are given in Appendix B. We found the point-mass model parameters of the cantilever to be $k \approx 28$ N/m, $Q = 420$ and $w_1 = 2\pi \times 254.4$ krad/s.

5.3 Noise

The noise in our measurement setup contains laser noise, shot noise of the photodiode, mechanical noise, electronic noise and thermomechanical noise of the cantilever. The total noise at the end of the preamplifier (SSM2017, Analog Devices, MA) is measured by a network/spectrum analyzer (HP 4195A, Hewlett Packard, CA) in a resolution bandwidth of 10 Hz. The filter slope and the time constant (τ) of the lock-in amplifier are chosen to be 24 dB/octave and 10 ms in all of the experiments. These values yield an equivalent noise bandwidth ($ENBW$)

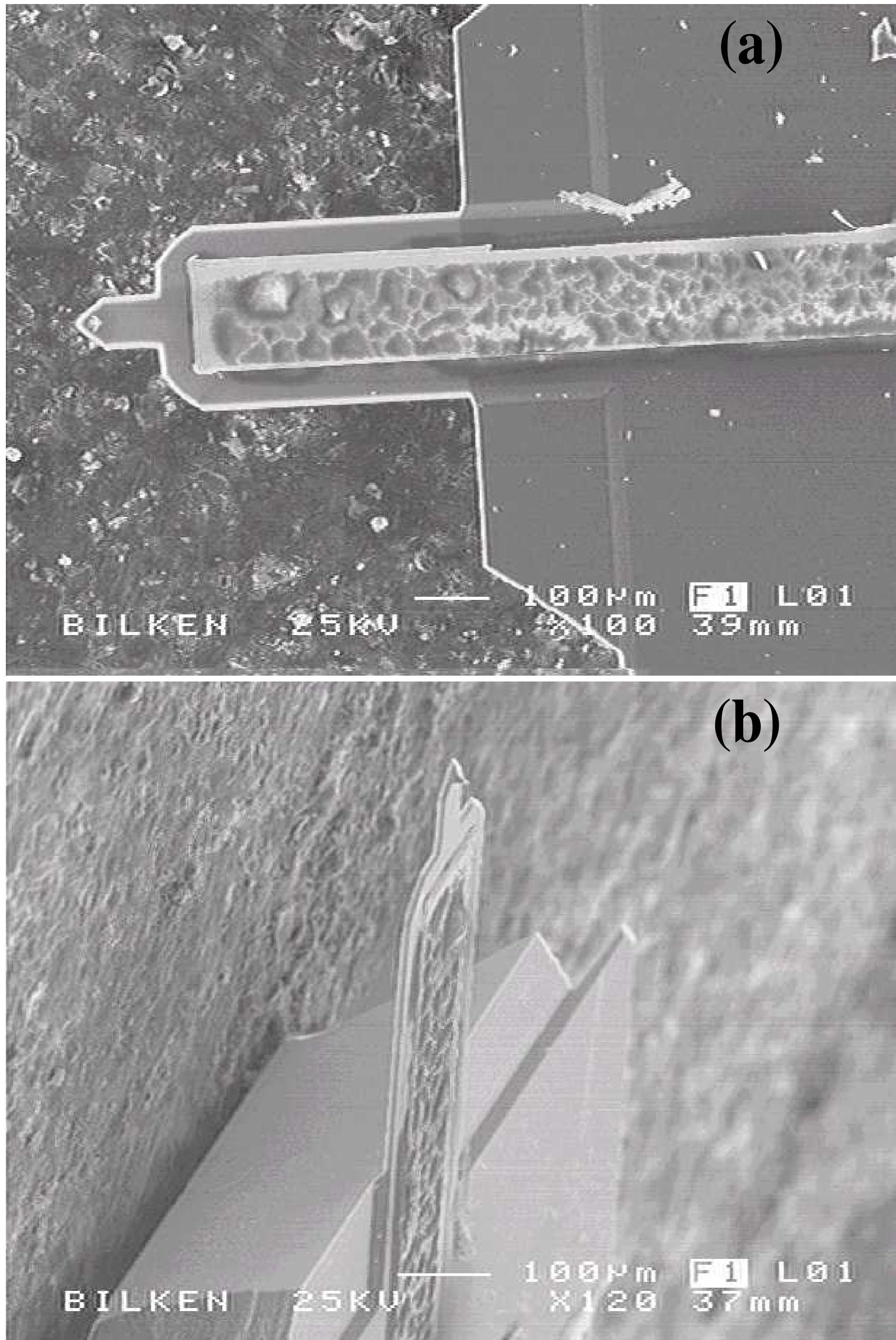

Figure 5.2: SEM micrograph of the cantilever showing both the sensor and actuator parts. (a) Top view. (b) Side view.

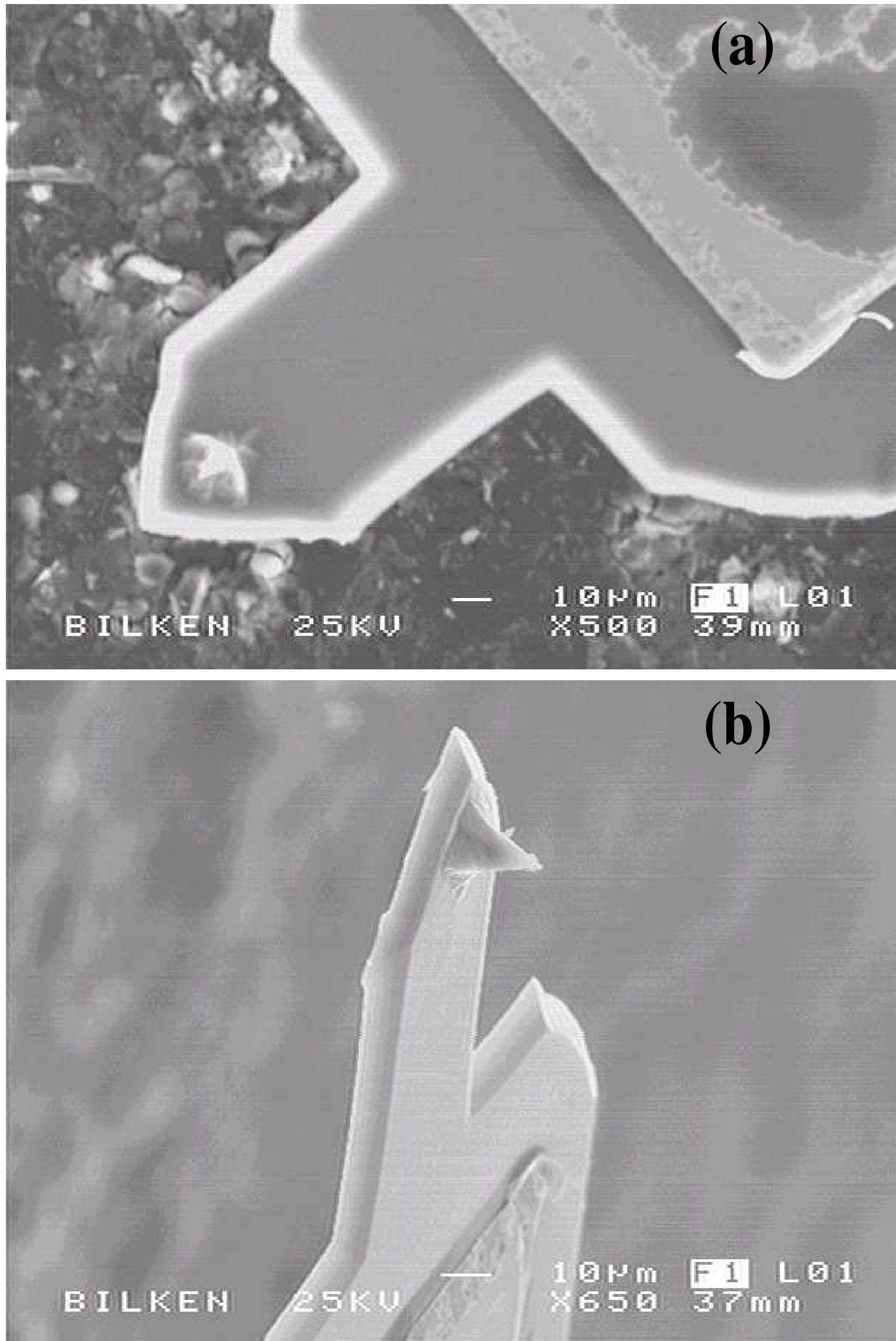

Figure 5.3: SEM micrograph of the sensor. (a) Top view. (b) Side view.

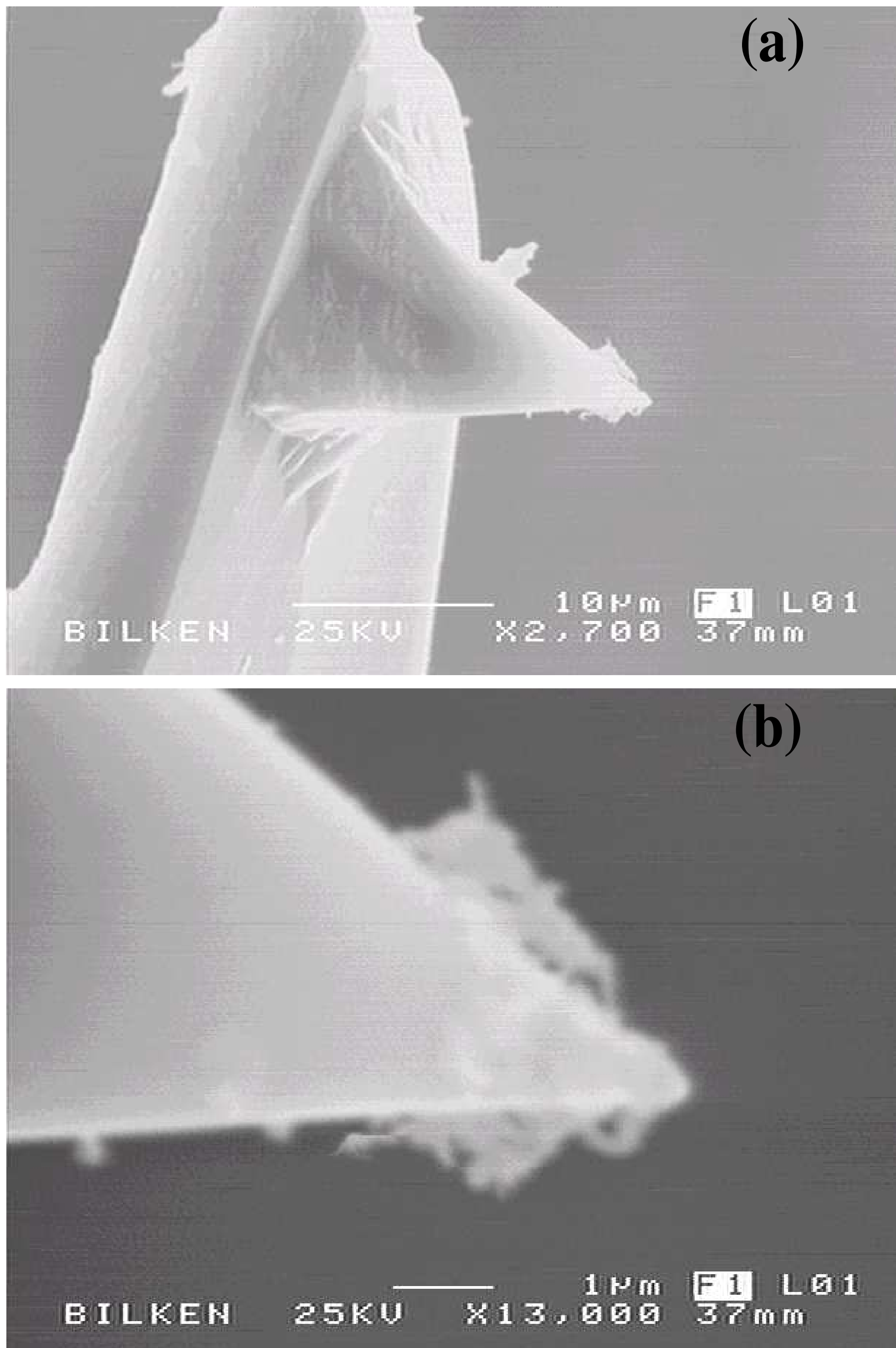

Figure 5.4: SEM micrograph of the tip in (a) and the tip end in (b).

of $5/(64\tau) = 7.8$ Hz, very close to the resolution bandwith of the spectrum analyzer. The total noise is found to be less than 90 μV up to 300 kHz. This is approximately equal to 0.04 Å (see Appendix C).

5.4 Experimental Problems

We observed several problems in the experiments. Some of these problems arose due to the proposed method. But, the others were seen in conventional tapping-mode also.

- **Optical interference:** The laser light reflected off the top of the cantilever and the light scattered from the sample surface interfere on the photodiode. It causes the detected voltage to drift slowly towards the set point value. Hence, the feedback loop assumes that the tip is touching the surface. The effect was so pronounced on the V-shaped cantilever that we could not use it. An FFT based method is proposed to remove the optical interference artifacts from the images off-line [100]. The high frequency laser current modulation technique [101] can also be utilized to remove the optical interference problem. We did not observe an interference problem for the cantilever that we used.

- **Noisy resonance spectra:** We observed that the resonance spectra of the cantilever is not so clean. The cantilever is vibrated by a piezoelectric bimorph located in the cantilever holder and a poor coupling between the piezo and the cantilever substrate results in a resonance peak deformation and additional parasitic peaks. The mechanical interface between the cantilever substrate and the holder must be as clean and smooth as possible.

- **Mechanical drift:** Our experiments took several hours due to slow scanning speed. We observed a small residual voltage at the end of some experiments. Since the optical head contains several adjustment screws, drifts in the long imaging times can be expected. The net effect of these drifts is a slight change in the set point of the measurement. The imaging speed can be increased by increasing the gain of the controller (considering the resonant frequency of the piezotube)

and then reducing the time constant of lock-in amplifier. The piezoelectric actuator part of our cantilever can also be used instead of piezotube to increase the speed [102]. We performed experiments at or below a tip speed of 1 μm/s and the time constant of lock-in amplifier was set to 10 ms.

- **Low oscillation amplitude:** We found that the oscillation amplitudes in harmonic imaging experiments are around a few nanometers. To increase the amplitude of oscillation by an order of magnitude, one requires to apply tens of volts by considering the maximum operating voltage of the tapping piezo. This problem can be solved more conveniently by using a larger tapping piezo or by applying any other excitation method.

- **Nonlinearity:** In the absence of tip-sample interaction, the harmonic amplitude should ideally be zero. However, in our experiments there was a small voltage ($\approx$ 0.25 mV) at the output of the second lock-in amplifier. This voltage increases as we operate closer to the resonance peak. There are two sources of this unwanted signal. The first one is the higher harmonic of the signal generator and the second one is the nonlinearity of the tapping piezo. We note that this signal is relatively small compared to the signal coming from the interaction and it can be subtracted from the measurement. Nonetheless, we must keep this signal below a certain value since it affects not only our harmonic measurement but also the tip-sample interaction.

- **Coupling:** In harmonic measurements, we applied voltages much larger than the ones that we applied for conventional operation since we excited the cantilever well below the resonance. This excitation signal is coupled to our deflection signal. Even though our operating frequency range is less than a megahertz, its effect is significant as shown in Fig. 5.5. We note that this is the signal at the output of the preamplifier (outside the head) which has a gain of 100. Hence, this problem can be alleviated by integrating the preamplifier to the head. We subtracted the coupled signal from the measured signal to find the real oscillation amplitude.

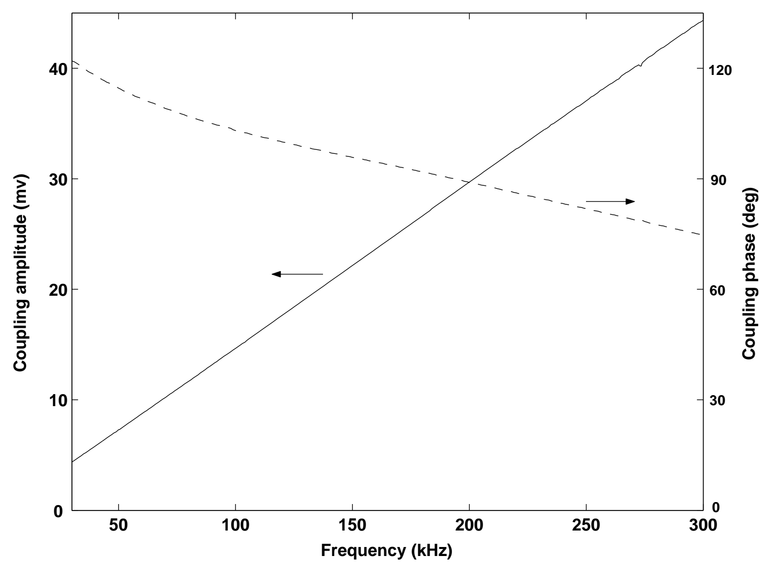

Figure 5.5: Amplitude and phase variations of the coupled voltage.

Chapter 6

Experimental Results

We tested our method on several samples. We have two test samples; one has only regular topography changes on it, and the other one has both topography and material changes on the surface. We analyzed three heterogeneous polymer mixtures and a triblock copolymer. A sample which has a scratched surface is also examined. We note that the order of the experiments is not the same as the order given in this chapter. All of the experiments were performed under ambient conditions and with the same cantilever.

In our analysis, we compared our results with the results of conventional tapping-mode topography and phase imaging. The locations where the images were taken are close but not the same for the harmonic imaging and conventional tapping-mode imaging experiments. The enhanced third harmonic imaging experiments were done by exciting the cantilever at a frequency of $w = 0.97w_{13}$. We excited the cantilever at $w = w_1$ for the conventional case. The oscillation amplitudes in the conventional cases are larger than those in the enhanced harmonic imaging experiments.

6.1 Test Samples

To check if the suggested method works or not, we studied two samples whose surface structures are known. The first sample, a square-patterned GaAs Substrate, is prepared by common microfabrication techniques (photolithography and wet etching). For the second sample, a square-patterned photoresist (PR) on GaAs substrate, the thickness of PR is thinned by reactive ion etching.

6.1.1 A Square-patterned GaAs Substrate

The optical micrographs of the first sample are shown in Fig. 6.1.

6.1.1.1 Enhanced Third Harmonic Imaging

The enhanced third harmonic image along with topography is given in Fig. 6.2. We see that the third harmonic does not change with topography [1] except at the edges of the squares where the oscillation amplitude changes as can be seen in Fig. 6.2 (a). This is what we expect since the material variation is uniform all over the sample surface. Three-dimensional views given in Fig. 6.3 clearly show that the third harmonic is almost constant through the surface.

Figure 6.4 shows the line [indicated in Fig. 6.2 (b)] profiles of the topography, third harmonic amplitude, and the error amplitude. Error amplitude is reversed and divided by ten to fit into the figure. Note that the third harmonic amplitude is almost constant except at the points where the error (fundamental amplitude) changes.

The histograms given in Fig. 6.5 also exhibit that the material uniformity does not change over the surface [a single hump in (c)] even though there is a topography variation [double humps in (b)]. The third harmonic amplitude is

[1] Here, what we mean with the topography is the change of surface height, but not the surface corrugation.

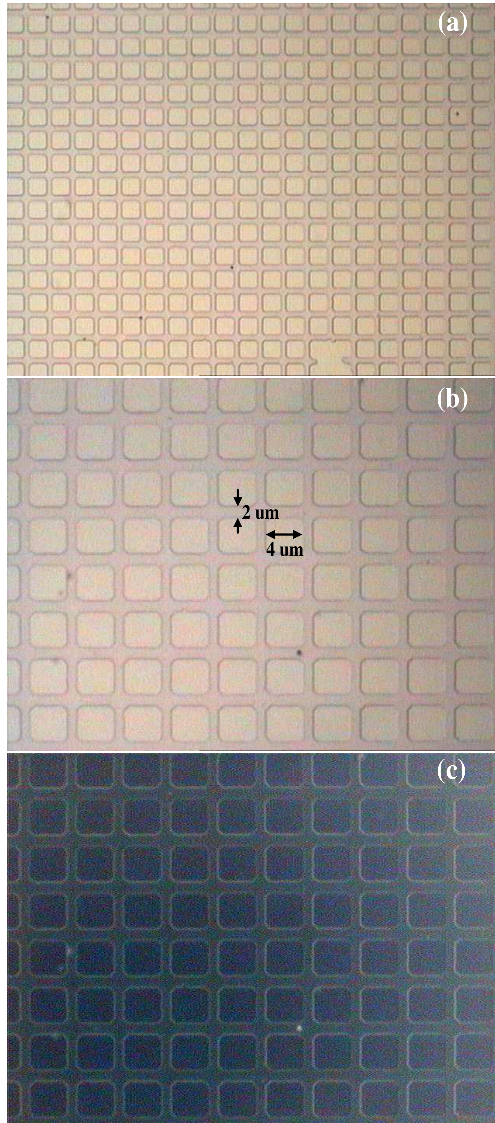

Figure 6.1: Optical micrographs of a square-patterned GaAs substrate at ×50 magnification in (a) and ×100 magnification in (b) and (c).

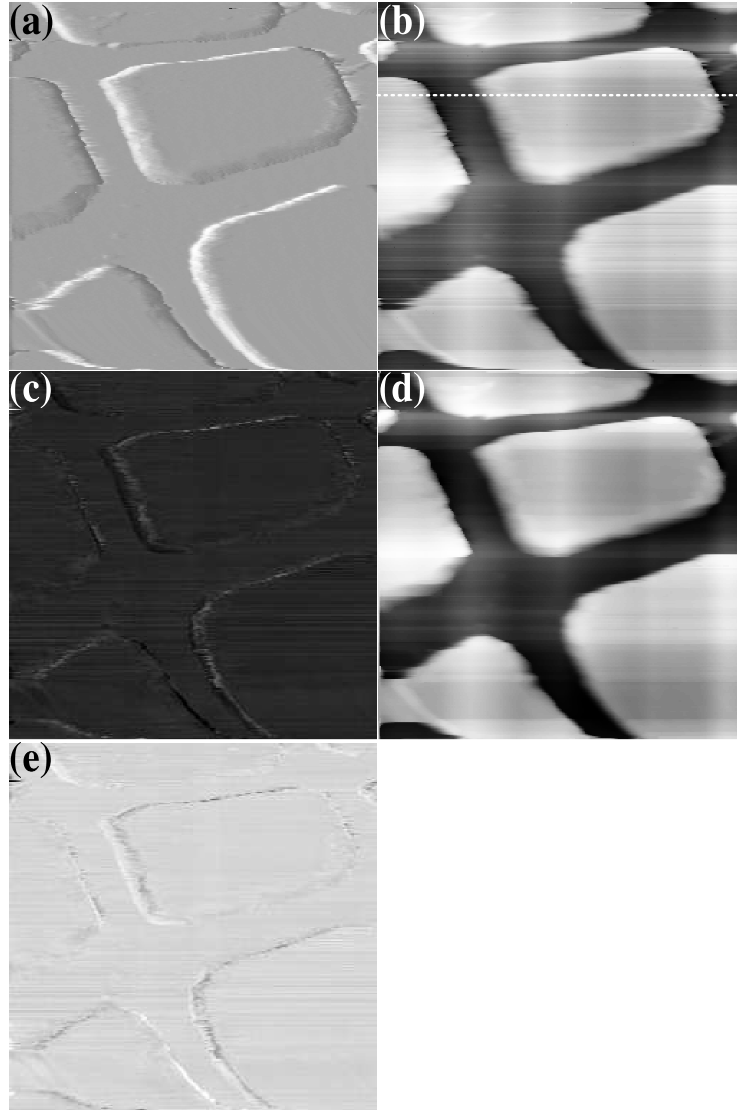

Figure 6.2: Enhanced third harmonic imaging of a square-patterned GaAs substrate. (a) Error, (b) Topography, (c) Third harmonic amplitude, (d) Topography (median filtered), and (e) Third harmonic amplitude (image contrast is reversed). The variation from black to white is 2.7 nm in (a), 340 nm in (b), 0.54 nm in (c), and 290 nm in (d). Image parameters: Scan size = 10×10 μm, Pixel size = 256×256, Scan speed = 0.8 μm/s. Operating parameters: $A_0 \approx 1.6$ nm, $A_1/A_0 = 1.2$, $w = 0.97 w_{13}$.

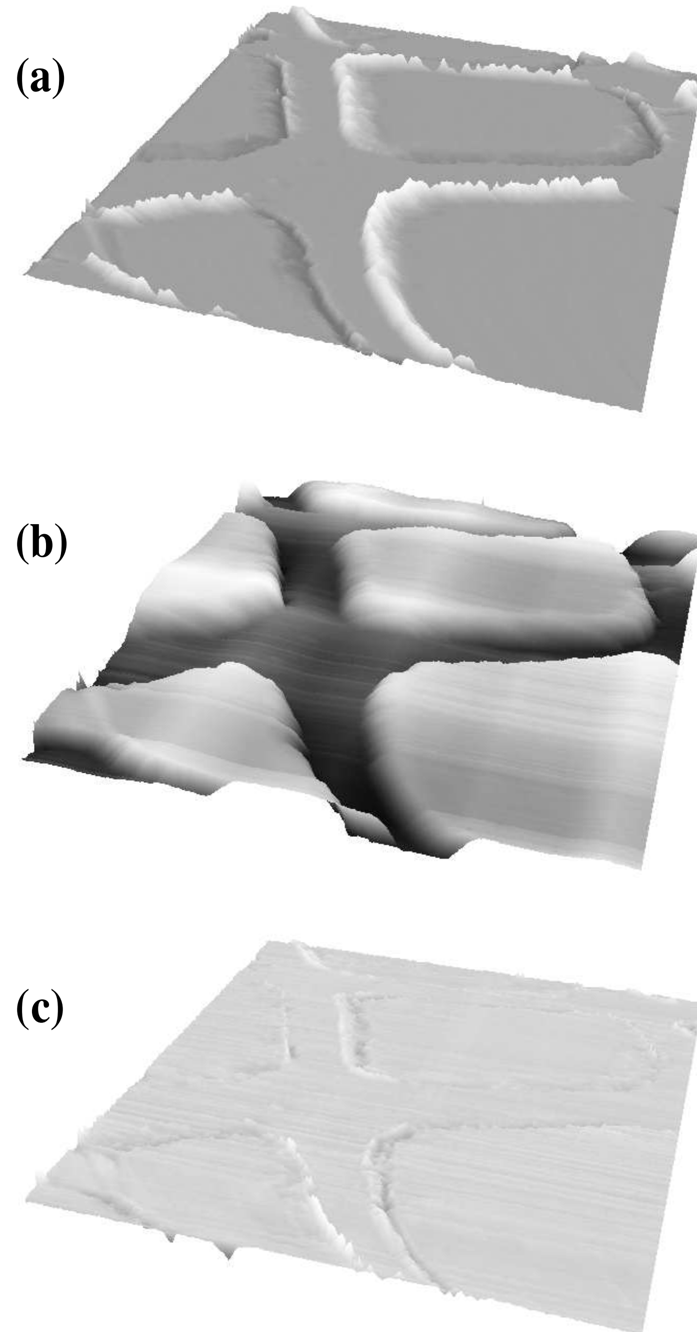

Figure 6.3: Three-dimensional views of the sample in Fig. 6.2. (a) Error, (b) Topography, and (c) Third harmonic amplitude (inverted colors).

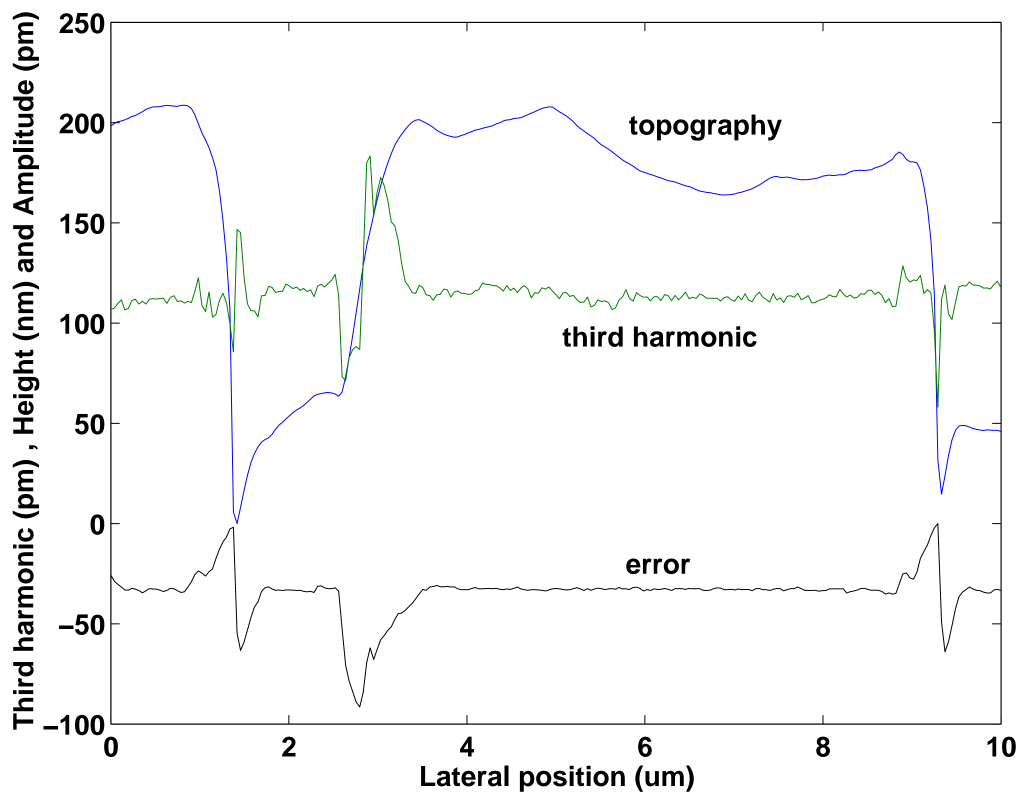

Figure 6.4: Third harmonic amplitude (green), surface topography (blue), and error amplitude (divided by -10 to fit) (black) variations across the line indicated in Fig. 6.2 (b).

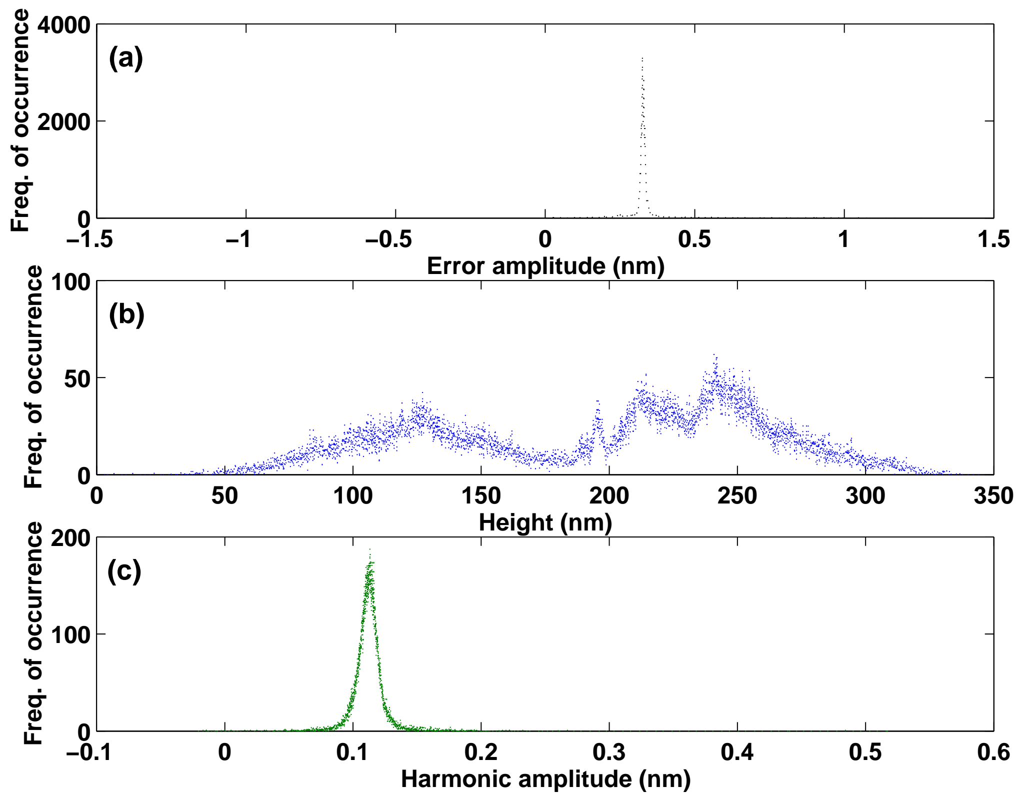

Figure 6.5: Histograms of (a) Error, (b) Surface height, and (c) Third harmonic.

approximately 1.2 Å on the average. This means a signal-to-noise ratio (SNR) of approximately 30 dB, where the total noise is found to be 0.04 Å.

6.1.1.2 Conventional Tapping-mode Imaging

We performed a conventional tapping-mode experiment for the same sample. The results are displayed in Figs. 6.6 and 6.7. We get the same topographical variation as in the previous experiment. To show the relation between the error and phase signals, we inverted the phase image contrast as shown in Figs. 6.6 (e). We observe that the error and phase signals are closely related to each other for this sample.

The line analysis is done in Fig. 6.8. The phase is shifted arbitrarily to fit into

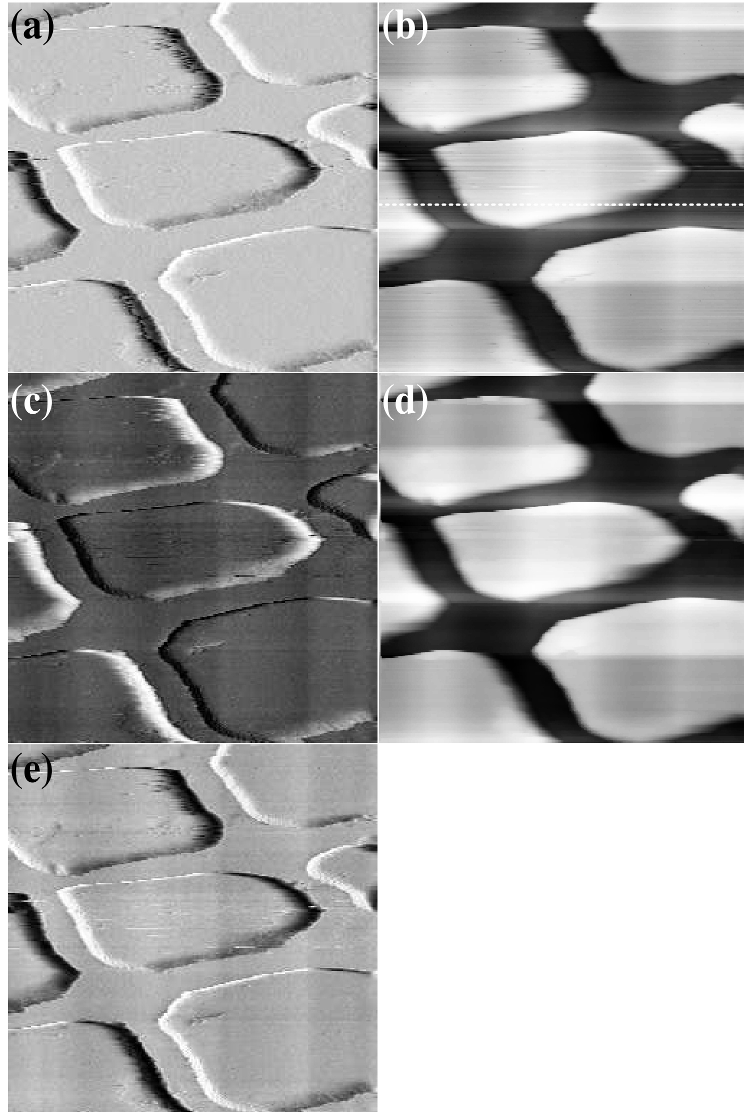

Figure 6.6: Conventional tapping-mode imaging of a square-patterned GaAs substrate. (a) Error, (b) Topography, (c) Phase, (d) Topography (median filtered), and (e) Phase (image contrast is reversed). The variation from black to white is 9.4 nm in (a), 300 nm in (b), 30° in (c), and 270 nm in (d). Image parameters: Scan size = 10×10 μm, Pixel size = 256×256, Scan speed = 0.8 μm/s. Operating parameters: $A_0 \approx 12.9$ nm, $A_1/A_0 = 0.78$, $w = w_1$.

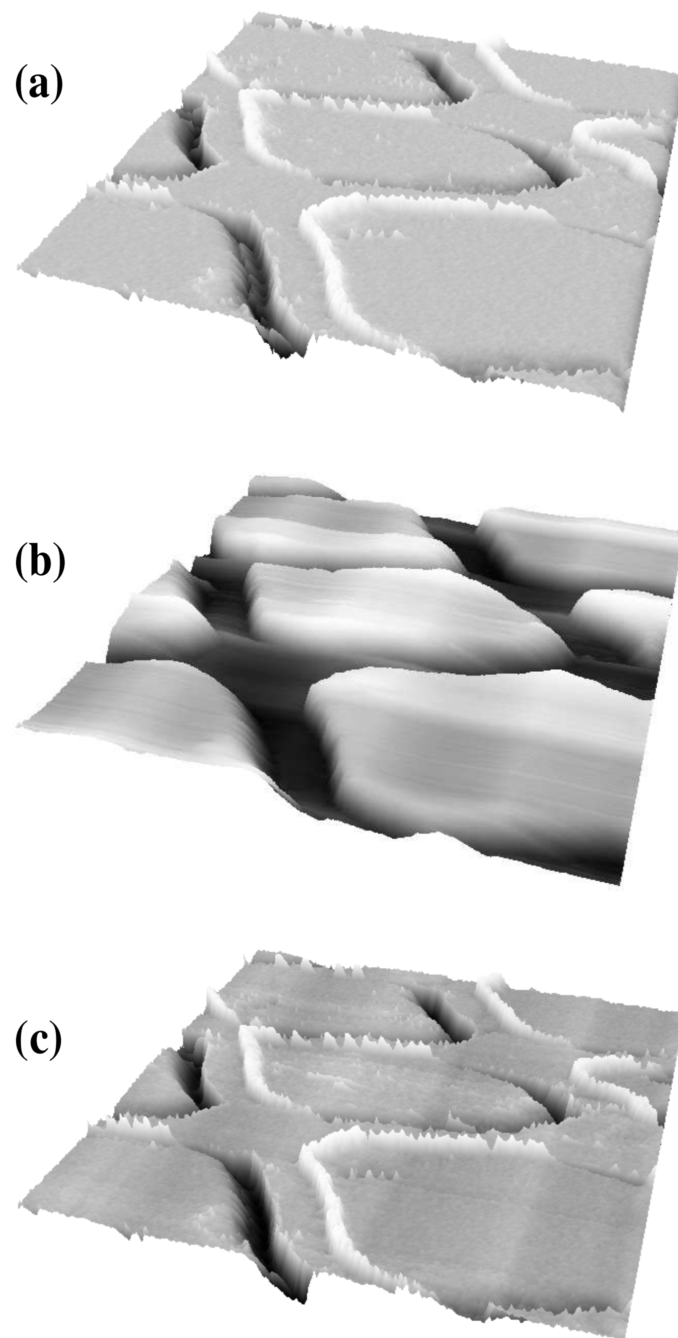

Figure 6.7: Three-dimensional views of the sample in Fig. 6.6. (a) Error, (b) Topography, and (c) Phase (inverted colors).

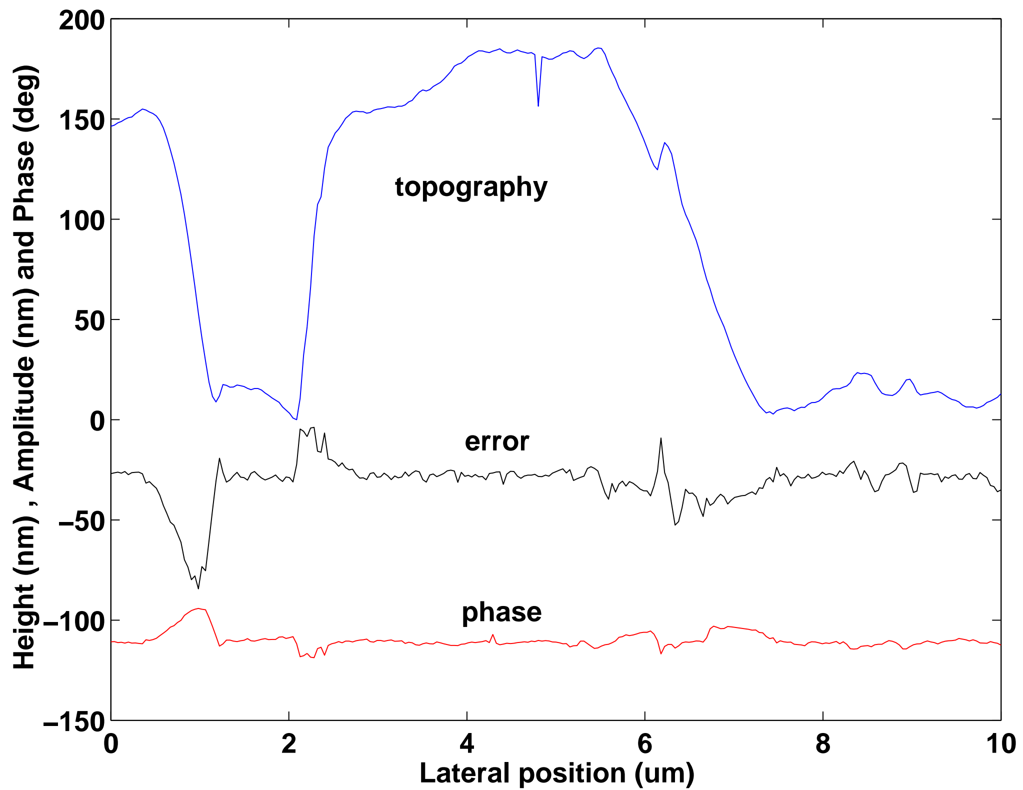

Figure 6.8: Surface topography (blue), error amplitude (multiplied by 10 to fit) (black), and phase (shifted arbitrarily) (red) variations across the line indicated in Fig. 6.6 (b).

the figure. The histograms of the error, topography, and phase are also provided in Fig. 6.9. It is seen that the phase is also nearly constant for this sample.

6.1.2 A Square-patterned Photoresist on GaAs Substrate

The optical micrographs of the second sample are shown in Fig. 6.10.

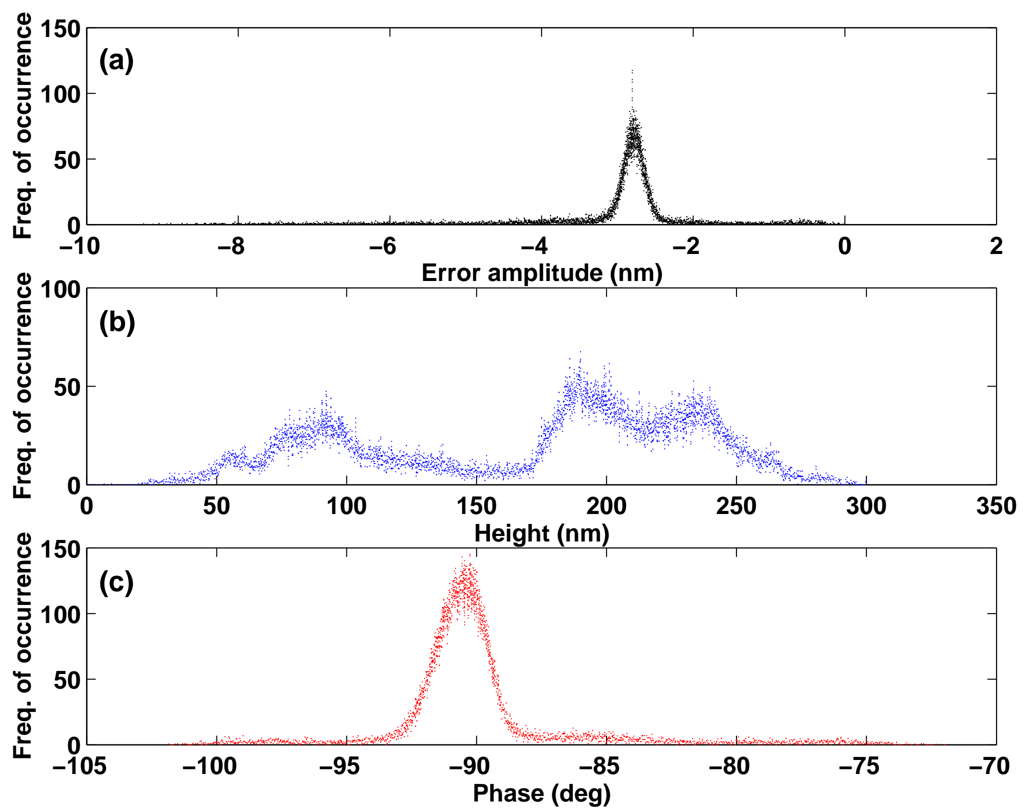

Figure 6.9: Histograms of (a) Error, (b) Surface height, and (c) Phase.

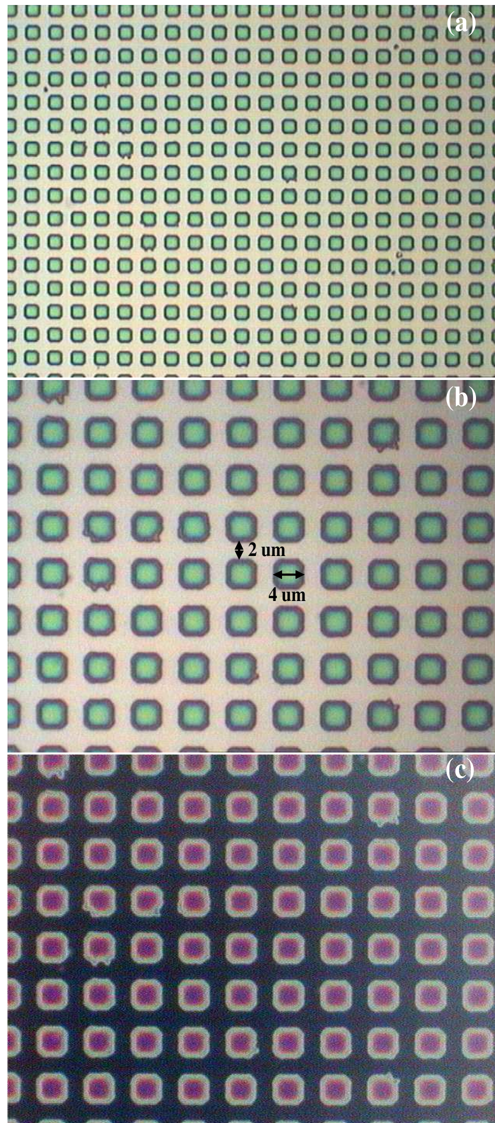

Figure 6.10: Optical micrographs of a square-patterned PR on GaAs substrate at ×50 magnification in (a) and ×100 magnification in (b) and (c).

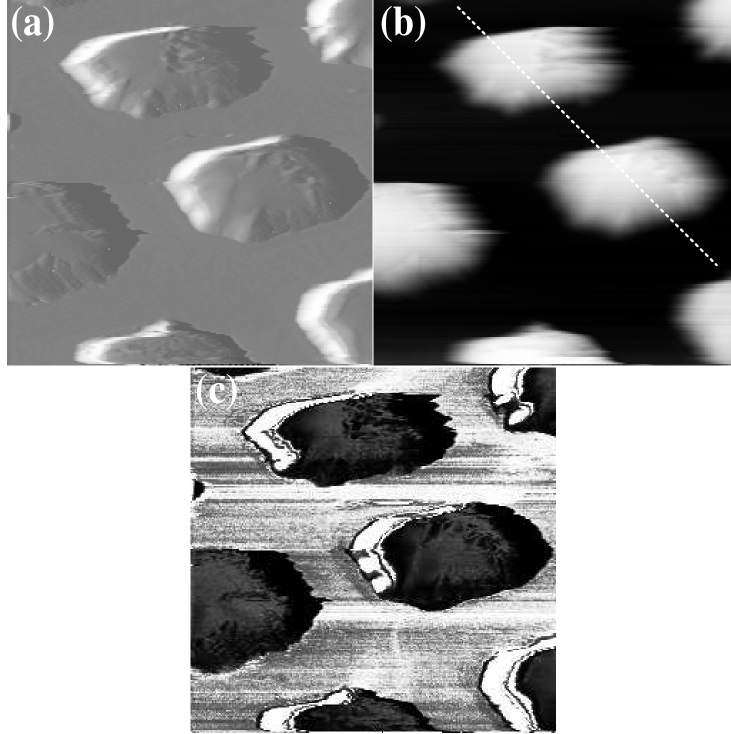

Figure 6.11: Enhanced third harmonic imaging of a square-patterned PR on GaAs substrate. (a) Error, (b) Topography, and (c) Third harmonic amplitude (image contrast is enhanced). The variation from black to white is 5.2 nm in (a), 700 nm in (b), and 0.9 nm in (c). Image parameters: Scan size = 10×10 μm, Pixel size = 256×256, Scan speed = 0.8 μm/s. Operating parameters: $A_0 \approx 1.6$ nm, $A_1/A_0 = 1.3$, $w = 0.97w_{13}$.

6.1.2.1 Enhanced Third Harmonic Imaging

We performed two experiments at different set point amplitudes for this sample. In the first one (Fig. 6.11), the third harmonic amplitude is seen to be lower at the region of PR (squares) than at the region of GaAs. Note that the contrast is enhanced in third harmonic image. Because in the original image, the amplitude difference between the two regions is not so obvious.

The cross sections corresponding to the line drawn in Fig. 6.11 (b) are given in Fig. 6.12. From this figure we see that the variation of third harmonic amplitude (the difference between the dashed lines) is small but it is roughly 17 dB larger

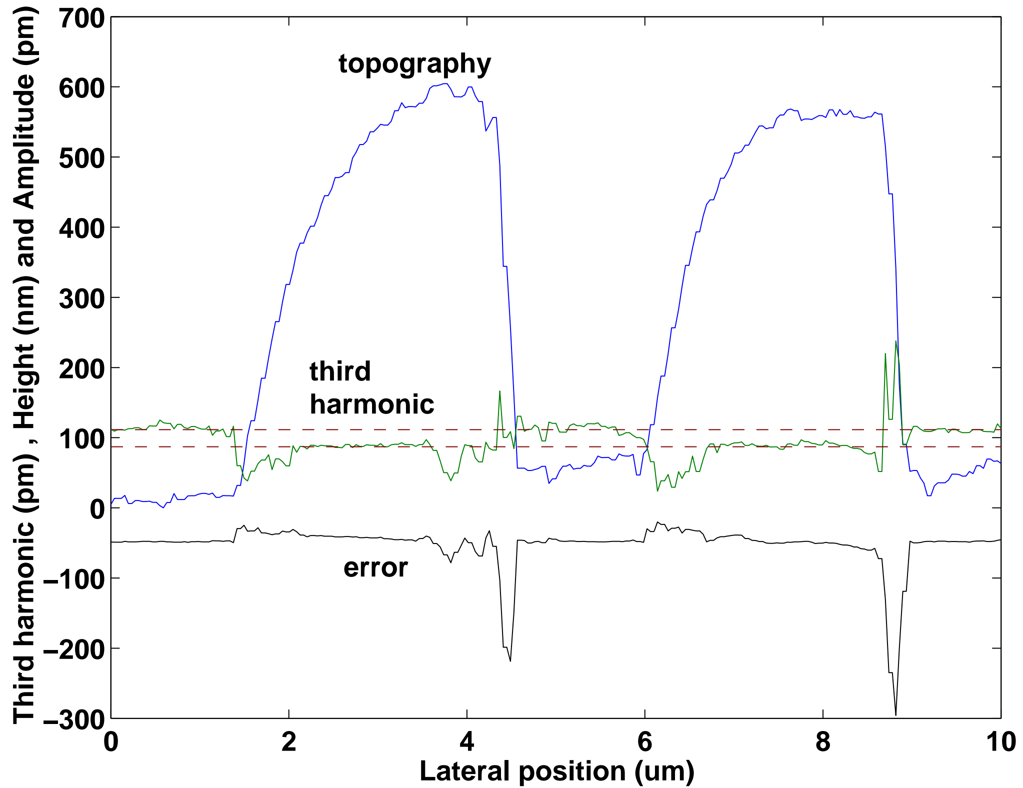

Figure 6.12: Third harmonic amplitude (green), surface topography (blue), and error amplitude (divided by -10 to fit) (black) variations across the line indicated in Fig. 6.11 (b).

than the noise level.

By looking at the histogram of the third harmonic [Fig. 6.13 (c)], we can say that the sample contains more than one kind of material. Note the small hump (and its extension left to it) near to the bigger one as compared to the previous experiment. The surface height corresponding to PR is seen to be distributed in a wide region. We think that the reason of this is the high scan speed (or low feedback gain) since the slopes of the features in Fig. 6.12 are not very sharp.

The second enhanced harmonic imaging experiment of this sample is performed at a lower set point amplitude. The scan speed is reduced to 0.5 μm/s. The pixel size is also reduced to complete the experiment in a reasonable time.

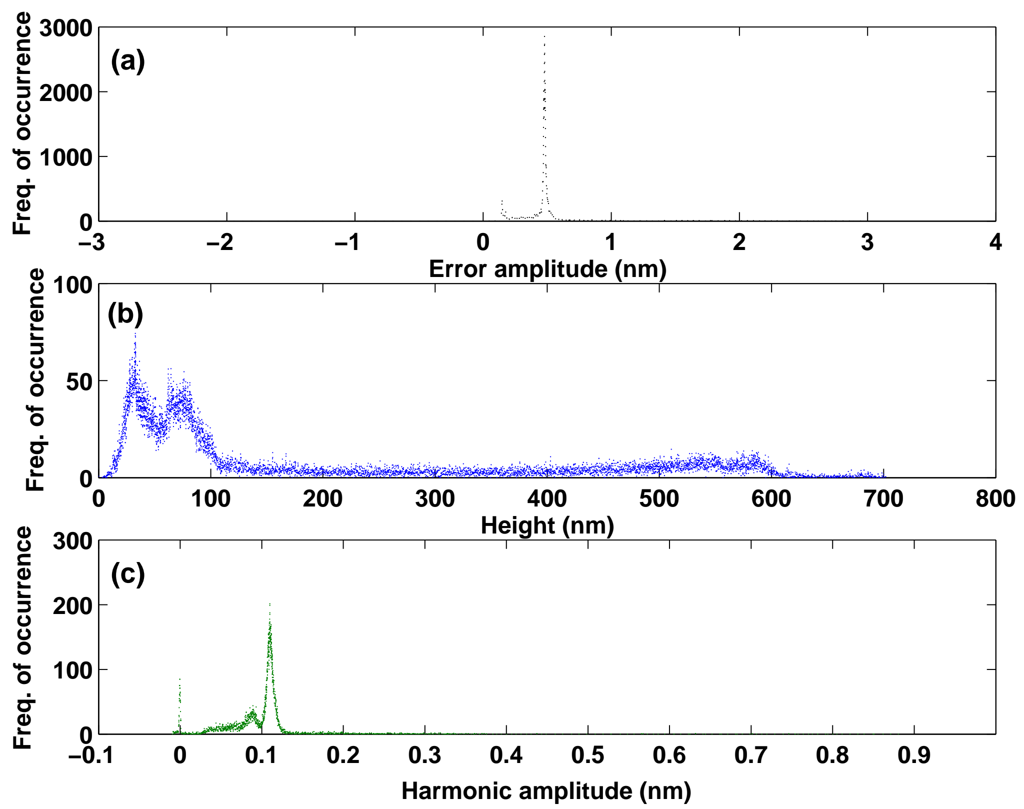

Figure 6.13: Histograms of (a) Error, (b) Surface height, and (c) Third harmonic.

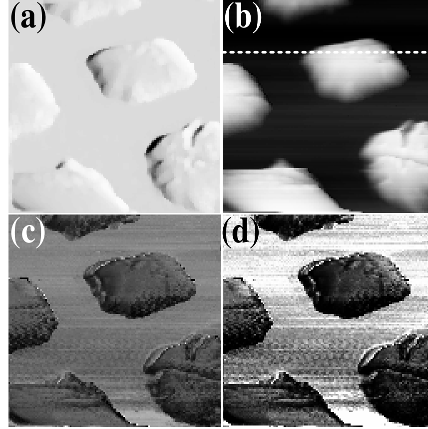

Figure 6.14: Enhanced third harmonic imaging of a square-patterned PR on GaAs substrate. (a) Error (image contrast is reversed), (b) Topography, (c) Third harmonic amplitude, and (d) Third harmonic amplitude (image contrast is enhanced). The variation from black to white is 3 nm in (a), 810 nm in (b), and 0.24 nm in (c). Image parameters: Scan size = 10×10 μm, Pixel size = 128×128, Scan speed = 0.5 μm/s. Operating parameters: $A_0 \approx 1.6$ nm, $A_1/A_0 = 1.2$, $w = 0.97w_{13}$.

The images and their three-dimensional views are shown in Figs. 6.14 and 6.15. The results are similar to the previous experiment. Clearly, the third harmonic detects the material difference in the sample.

Again, we see from the line analysis in Fig. 6.16 that the difference between the dashed lines is well above the noise level. Interestingly, the amplitudes of the higher harmonics are almost same for these two experiments where the set point amplitudes differ about 8%. We see that the extent of the third harmonic amplitude [see Fig. 6.17 (c)] is smaller compared to the previous experiment since the operation is done at a lower set point amplitude.

6.1.2.2 Conventional Tapping-mode Imaging

The results of the conventional mode are shown in Fig. 6.18. The quality of the topography image is not so good. This can be related to the tip contamination

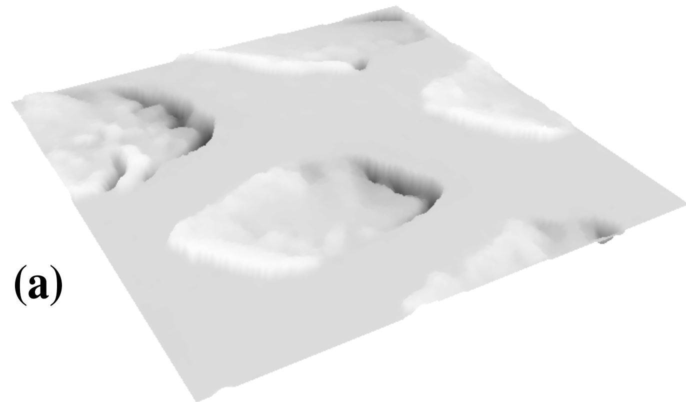

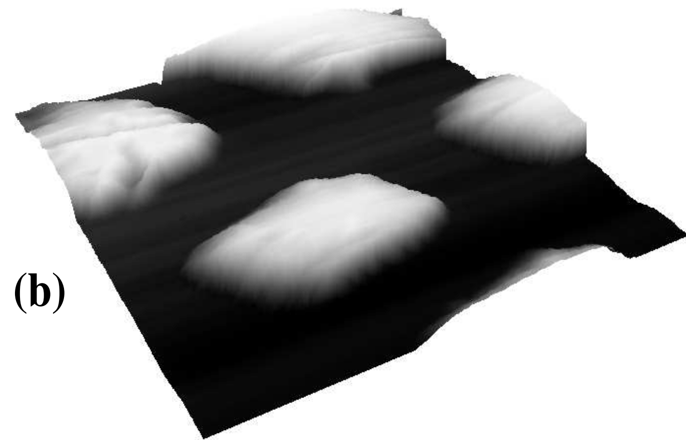

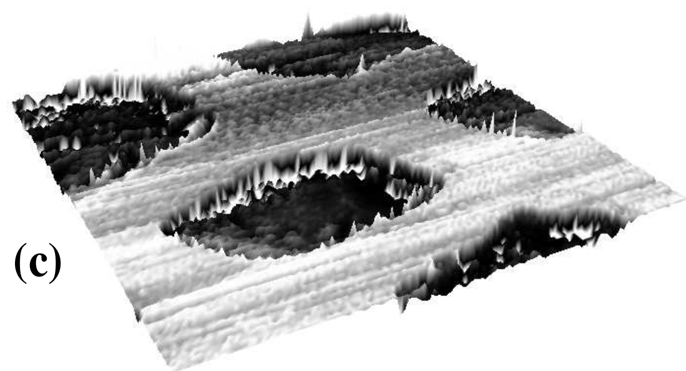

Figure 6.15: Three-dimensional views of the sample in Fig. 6.14. (a) Error, (b) Topography, and (c) Third harmonic amplitude (enhanced contrast).

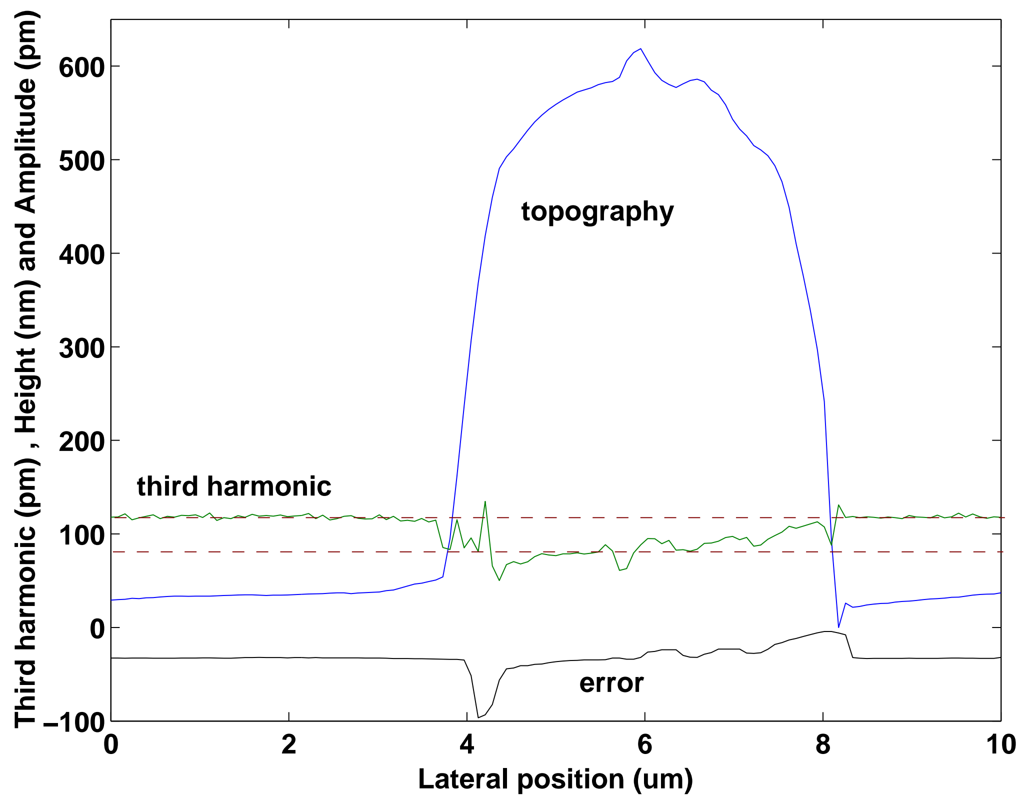

Figure 6.16: Third harmonic amplitude (green), surface topography (blue), and error amplitude (divided by -10 to fit) (black) variations across the line indicated in Fig. 6.14 (b).

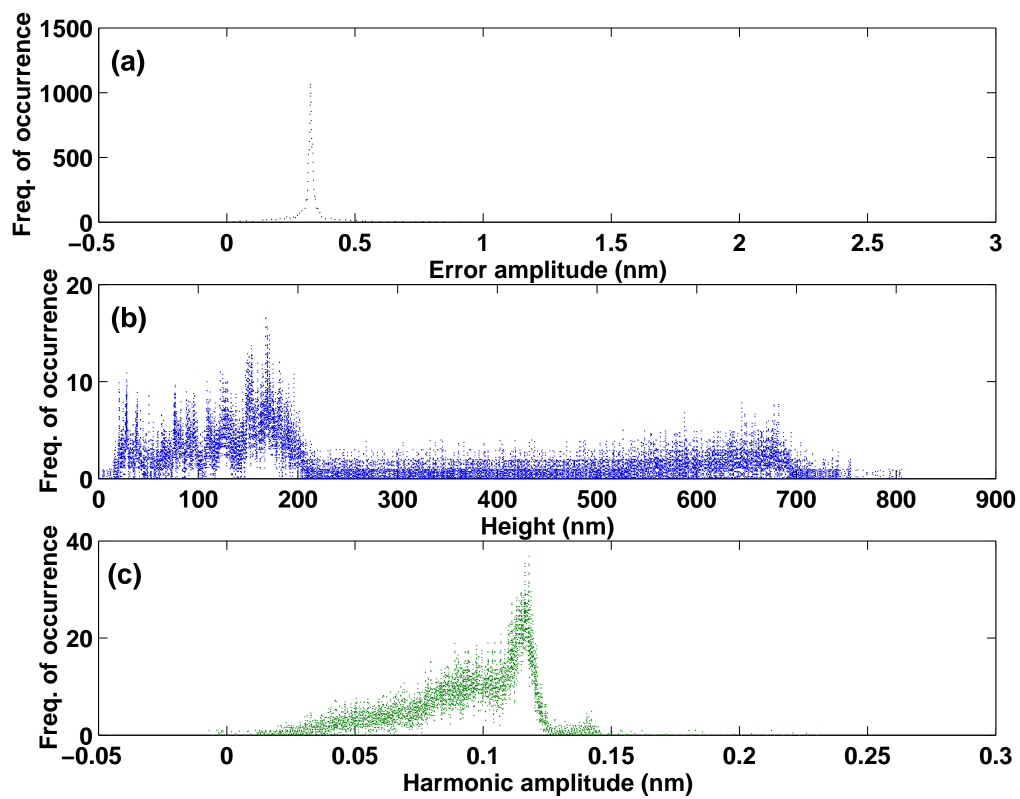

Figure 6.17: Histograms of (a) Error, (b) Surface height, and (c) Third harmonic.

(see previous chapter). The white lines (which contains no data) in the phase image can be attributed to a software failure.

The line analysis and the histograms are given in Figs. 6.19 and 6.20, respectively. Note the similarity between the phase and error signals.

6.2 Heterogeneous Polymers

The previous experiments showed that the enhanced higher harmonic can be used to map material heterogeneity in a sample. To show the usefulness of our method, we applied it to the heterogeneous polymer samples. We acquired polystyrene (PS) (Product No. 43,010-2), polyisoprene (PI) (Product No. 43,126-5), and polystyrene-*block*-polyisoprene-*block*-polystyrene (SIS) (Product No. 43,239-3) from the Sigma-Aldrich Company. We chose PS and PI to make mixtures of them since they differ significantly in both mechanical and chemical properties. Polystyrene is a hard, glassy, and strong polymer. Polyisoprene (natural rubber) is, on the other hand, soft and sticky. Some of the properties of PS and PI are listed in Table 6.1. The information about the structural, mechanical, and thermodynamic properties of SIS triblock copolymers can be found in the literature [103–107].

Three blends and the SIS block copolymer were cast into thin films by a solution casting method using xylene as solvent. The first blend has a mass fraction of PS of 20% and a mass fraction of PI of 80% (designated by 20:80), the second blend has a mass fraction of PS of 80% and a mass fraction of PI of 20% (designated by 80:20), and the third blend has mass fractions of both PS and PI of 50% (designated by 50:50). These blends were prepared by mixing solutions of a mass fraction of PS of 2% in xylene and a mass fraction of PI of 2% in xylene at the appropriate ratios and spin casting the solutions onto silicon substrates. Prior to application of the solutions, the silicon substrates were cleaned with acetone. The cast films were conditioned for 1 day in vacuum.

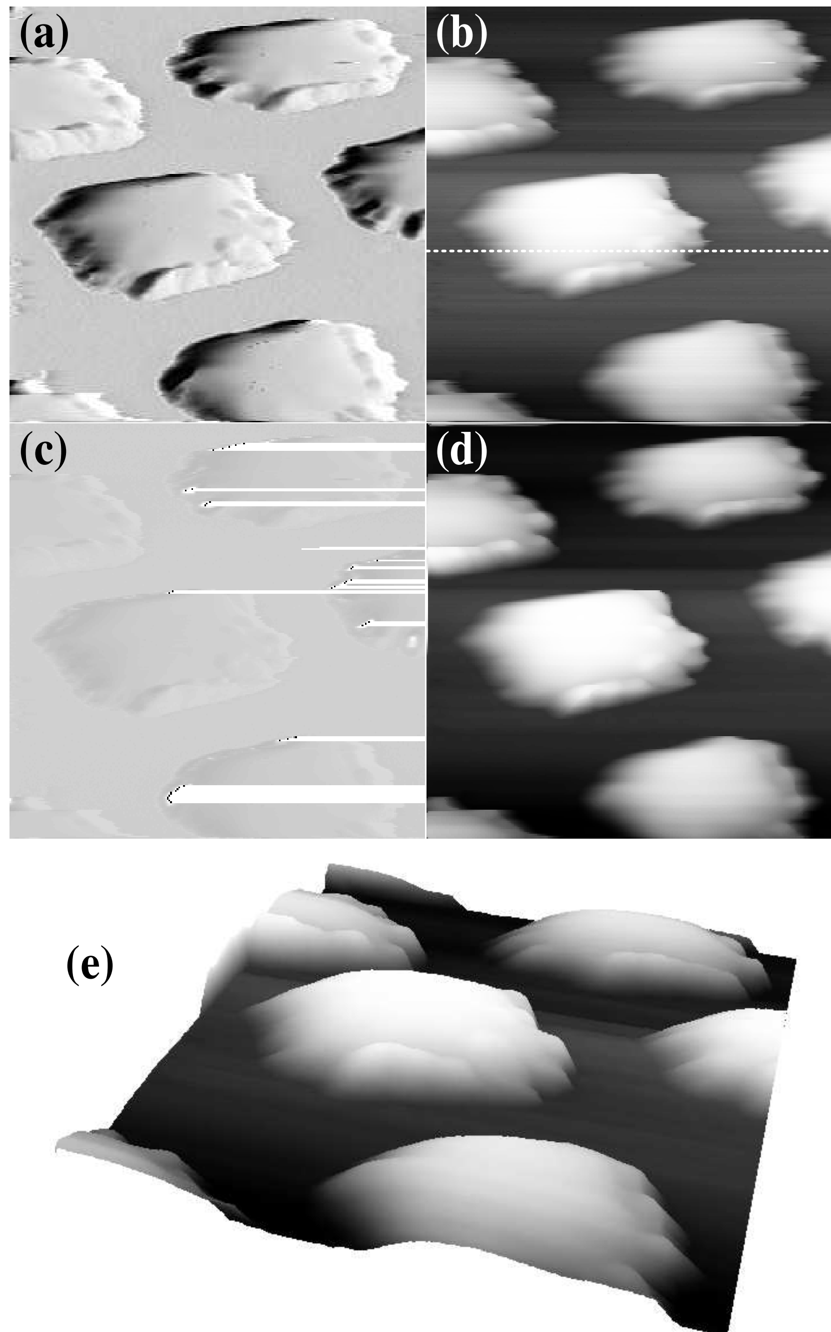

Figure 6.18: Conventional tapping-mode imaging of a square-patterned PR on GaAs substrate. (a) Error, (b) Topography, (c) Phase (image contrast is reversed), (d) Topography (median filtered), and (e) Three-dimensional view of topography. The variation from black to white is 10.9 nm in (a), 910 nm in (b), 120° in (c), and 770 nm in (d). Image parameters: Scan size = 10×10 μm, Pixel size = 256×256, Scan speed = 0.8 μm/s. Operating parameters: $A_0 \approx 14.3$ nm, $A_1/A_0 = 0.82$, $w = w_1$.

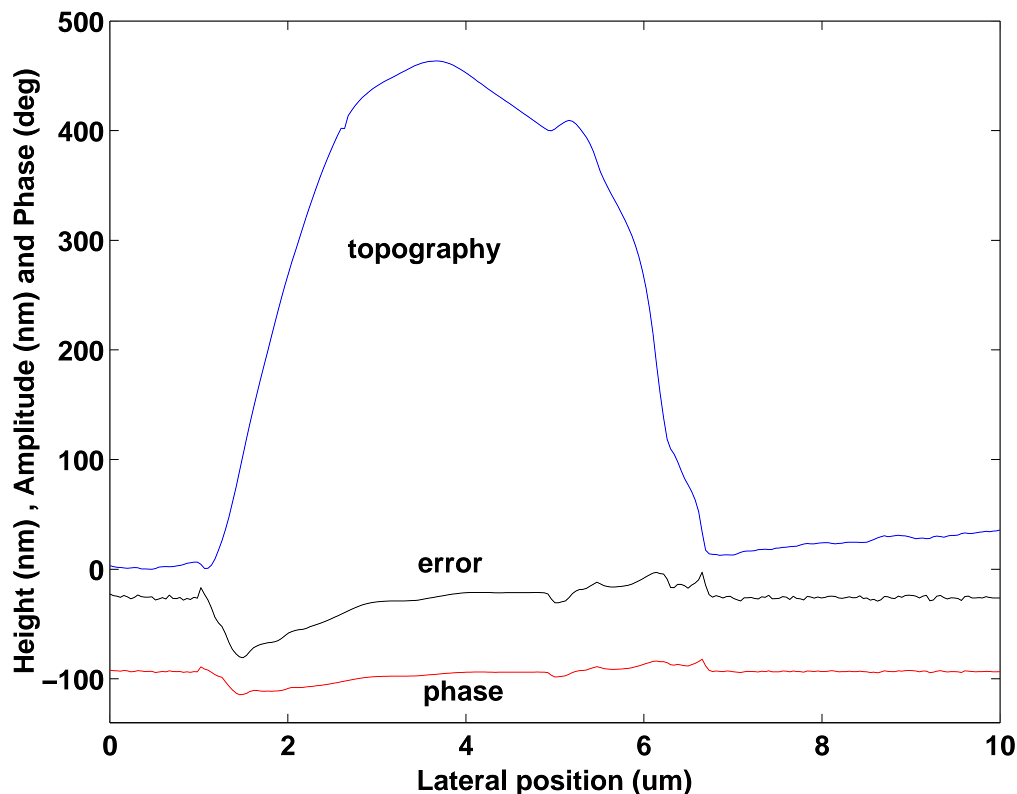

Figure 6.19: Surface topography (blue), error amplitude (multiplied by 10 to fit) (black), and phase (shifted arbitrarily) (red) variations across the line indicated in Fig. 6.18 (b).

Table 6.1: Properties of polystyrene and polyisoprene.

	Polystyrene	Polyisoprene
Molecular weight †	230,000	40,000
Density (g/mL) †	1.04	0.92
Glass transition temperature (^{o}C)	94 †	-72 ‡,§
Viscosity (poise) †		400
Elastic modulus (MPa)	3000 ‡	1-2 ‡,¶,*
Poisson ratio	0.33 ‡	0.49989 ‡,¶

† From Manufacturer.

‡ From Ref. [108].

§ Unvulcanized.

¶ Pure-gum vulcanizate.

* 2-100 MPa in Ref. [109].

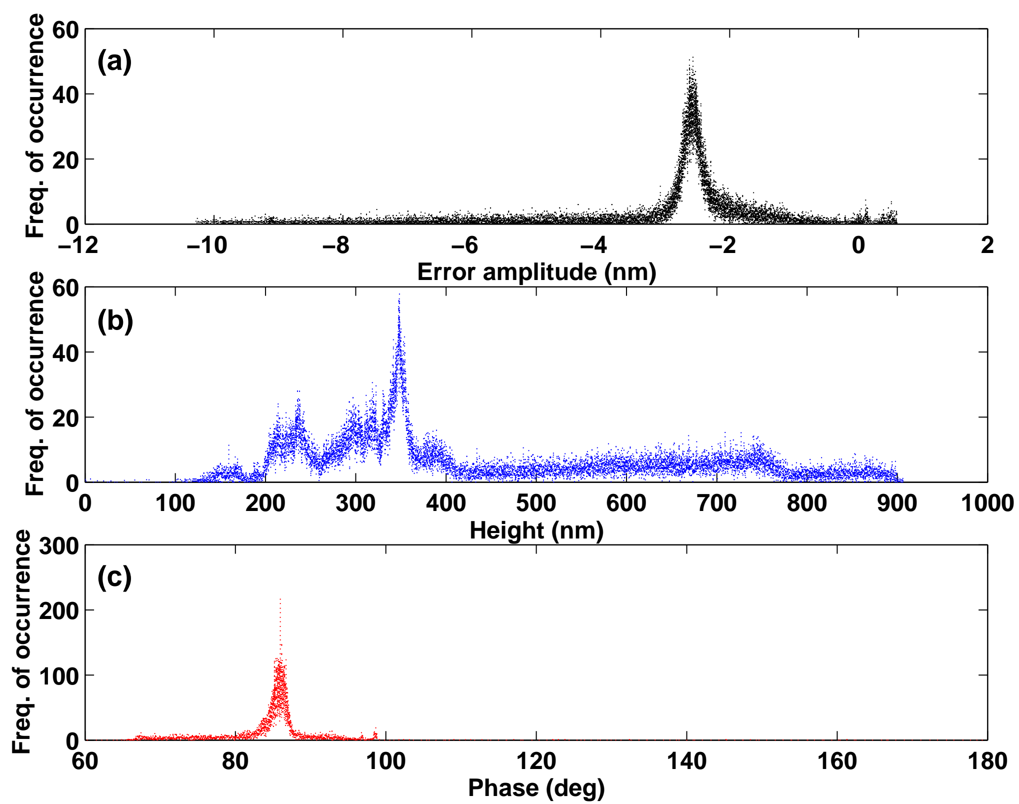

Figure 6.20: Histograms of (a) Error, (b) Surface height, and (c) Phase.

6.2.1 20:80 Polystyrene/Polyisoprene Blend

The optical micrographs of the first blend are shown in Fig. 6.21.

6.2.1.1 Enhanced Third Harmonic Imaging

The enhanced third harmonic and topography images of 20:80 PS/PI blend are shown in Fig. 6.22. Since the sample is composed of two mechanically different materials we expect that the third harmonic response is different in the different regions of the surface. We see that the low amplitude regions in the third harmonic image correspond to the high features in the topography image (see also Fig. 6.23). Also note that the small features are more distinct in the third harmonic image. In the error image, the fundamental amplitude increases or decreases as the tip passes over the edges of the hills.

The cross sections corresponding to the dashed and dotted lines drawn in Fig. 6.22 (d) are given in Figs. 6.24 and 6.25, respectively. The difference between the harmonic amplitudes for the hills and pits is clearly detectable. The signal level is around 0.2 nm which results in an SNR of 34 dB.

In the histogram of third harmonic [Fig. 6.26 (c)], there is no single hump, but rather the amplitude variation is distributed. Hence, we can safely say that the sample contains more than one kind of material.

6.2.1.2 Conventional Tapping-mode Imaging

The results of the conventional mode of operation are presented in Figs. 6.27 and 6.28. The topography image is very similar to what we obtained in the previous experiment. The phase image shown in (c) is seen to be closely related to the inverted error image given in (d). Note also the small protuberances seen in the error and phase images.

One scan line [indicated in Fig. 6.27 (b)] for each image is given in Fig. 6.29.

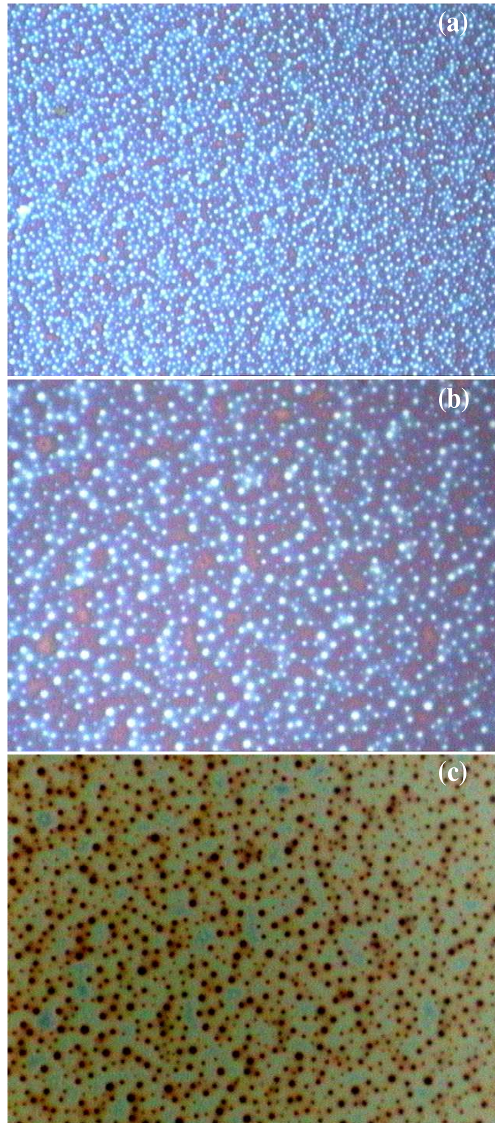

Figure 6.21: Optical micrographs of a 20:80 PS/PI blend at ×50 magnification in (a) and ×100 magnification in (b) and (c).

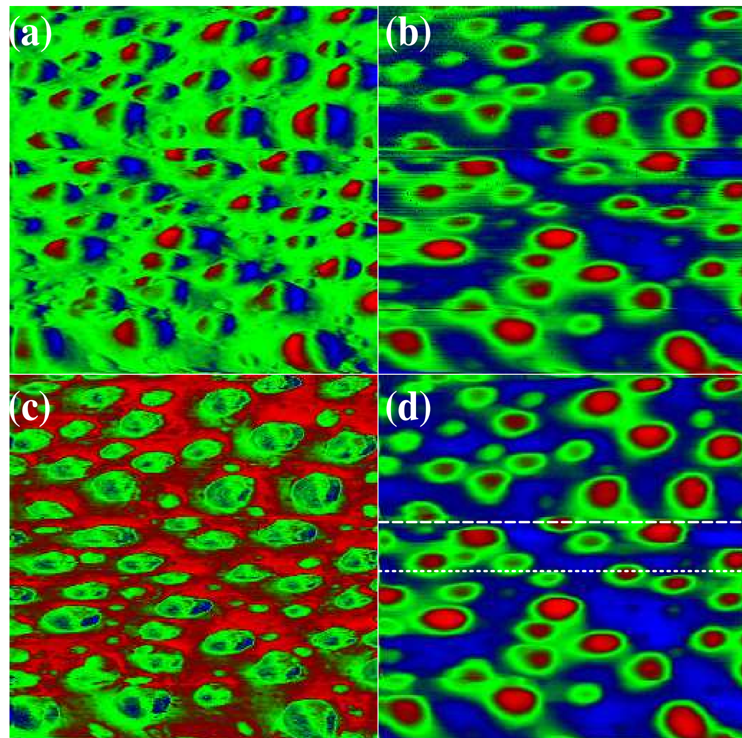

Figure 6.22: Enhanced third harmonic imaging of a 20:80 PS/PI blend. (a) Error, (b) Topography, (c) Third harmonic amplitude, and (d) Topography (median filtered). The variation from blue to red is 0.66 nm in (a), 150 nm in (b), 0.2 nm in (c), and 130 nm in (d). Image parameters: Scan size = 10×10 μm, Pixel size = 256×256, Scan speed = 1 μm/s. Operating parameters: $A_0 \approx 2.4$ nm, $A_1/A_0 = 1.2$, $w = 0.97 w_{13}$.

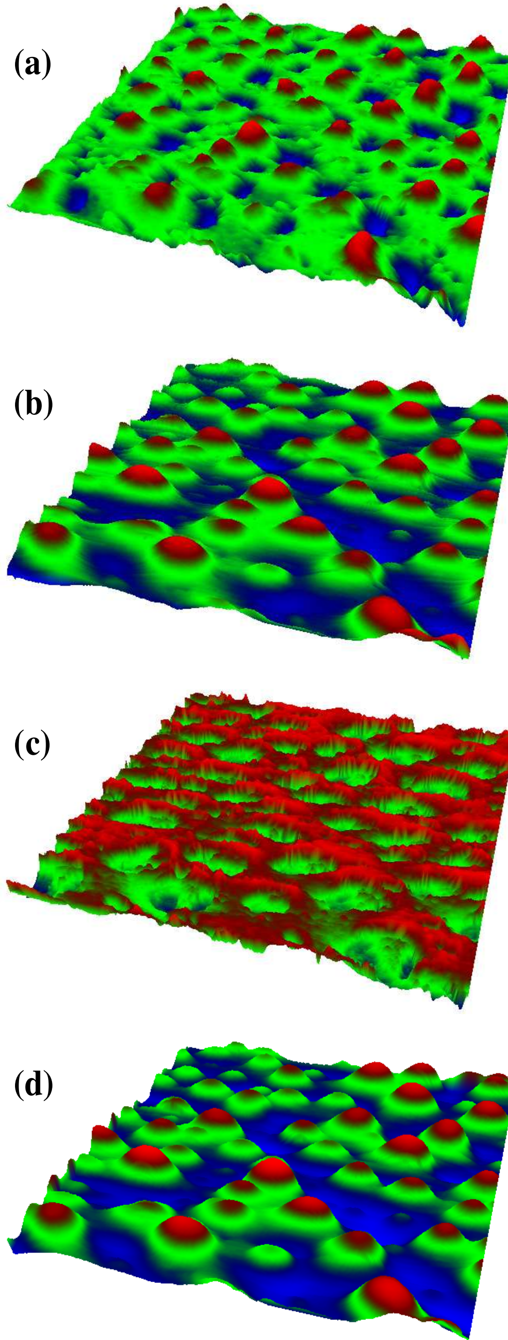

Figure 6.23: Three-dimensional views of the sample in Fig. 6.22. (a) Error, (b) Topography, (c) Third harmonic amplitude, and (d) Topography (median filtered).

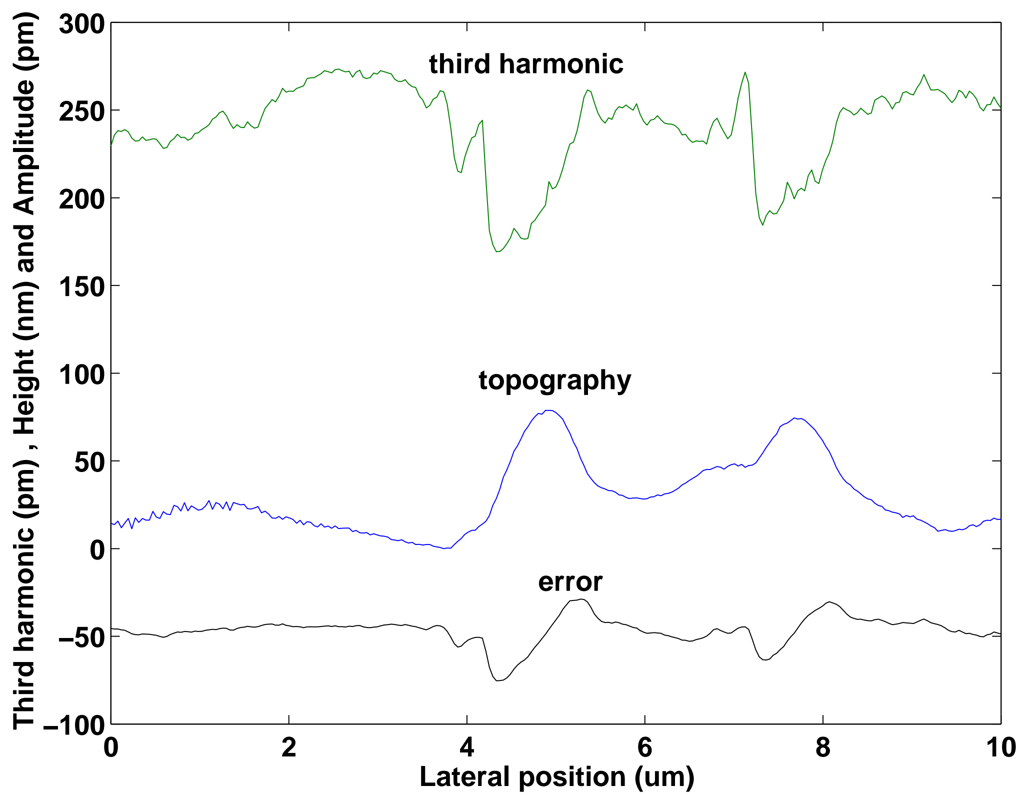

Figure 6.24: Third harmonic amplitude (green), surface topography (blue), and error amplitude (divided by -10 to fit) (black) variations across the dashed line indicated in Fig. 6.22 (d).

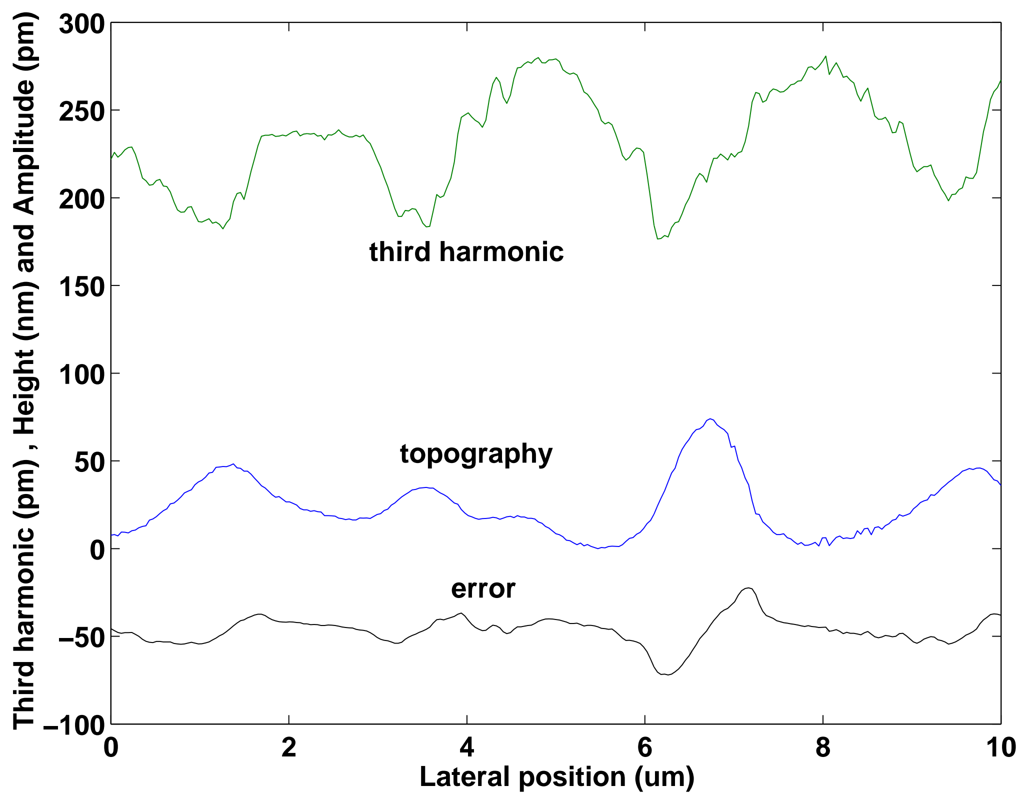

Figure 6.25: Third harmonic amplitude (green), surface topography (blue), and error amplitude (divided by -10 to fit) (black) variations across the dotted line indicated in Fig. 6.22 (d).

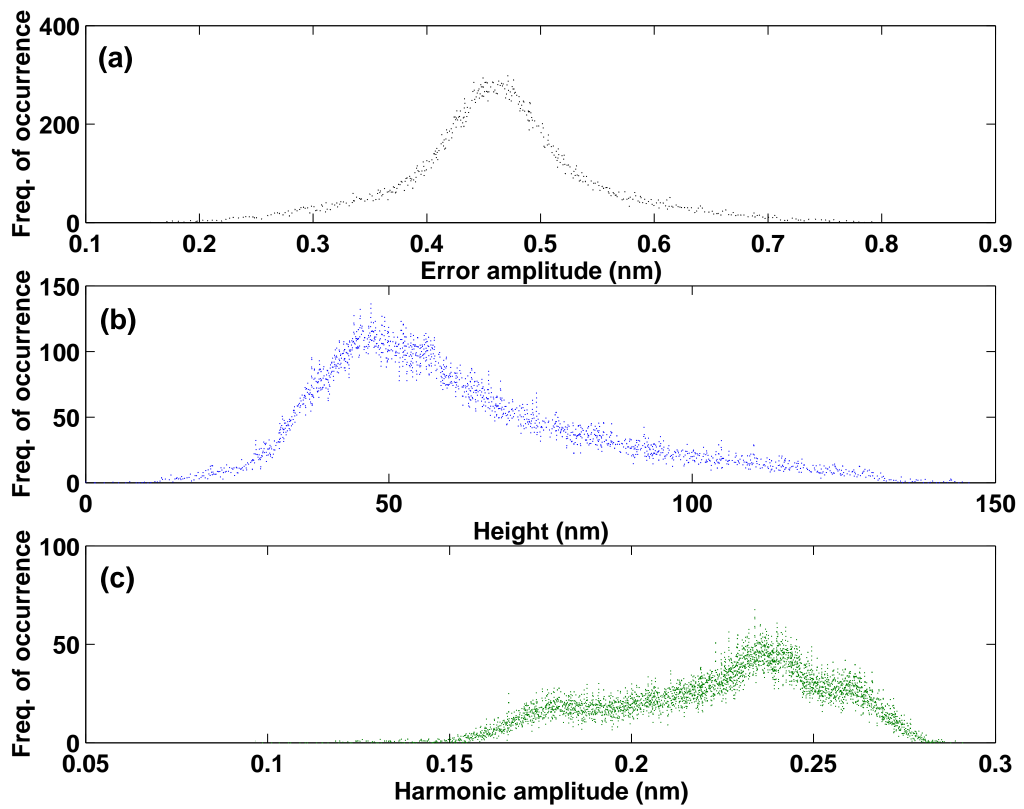

Figure 6.26: Histograms of (a) Error, (b) Surface height, and (c) Third harmonic.

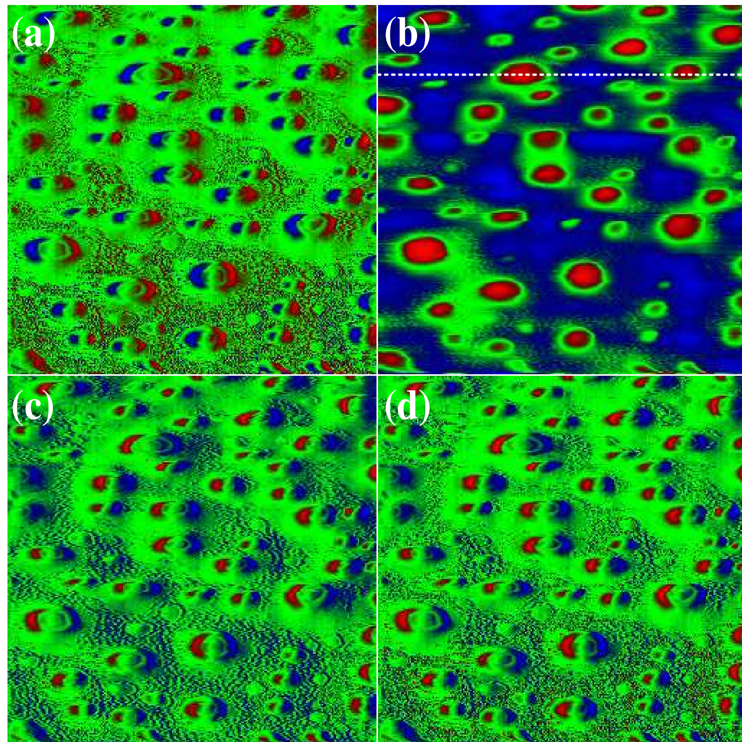

Figure 6.27: Conventional tapping-mode imaging of of a 20:80 PS/PI blend. (a) Error, (b) Topography, (c) Phase, and (d) Error (image contrast is reversed). The variation from blue to red is 1 nm in (a), 150 nm in (b), and 12° in (c). Image parameters: Scan size = 10×10 μm, Pixel size = 256×256, Scan speed = 1 μm/s. Operating parameters: $A_0 \approx 10$ nm, $A_1/A_0 = 0.9$, $w = w_1$.

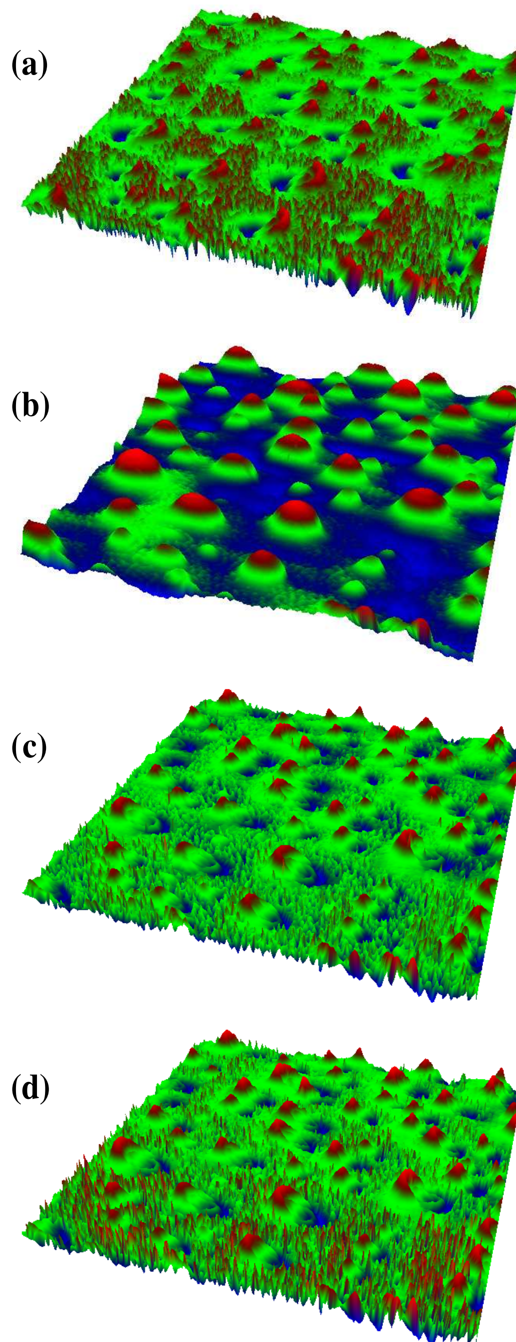

Figure 6.28: Three-dimensional views of the sample in Fig. 6.27. (a) Error, (b) Topography, (c) Phase, and (d) Error (inverted colors).

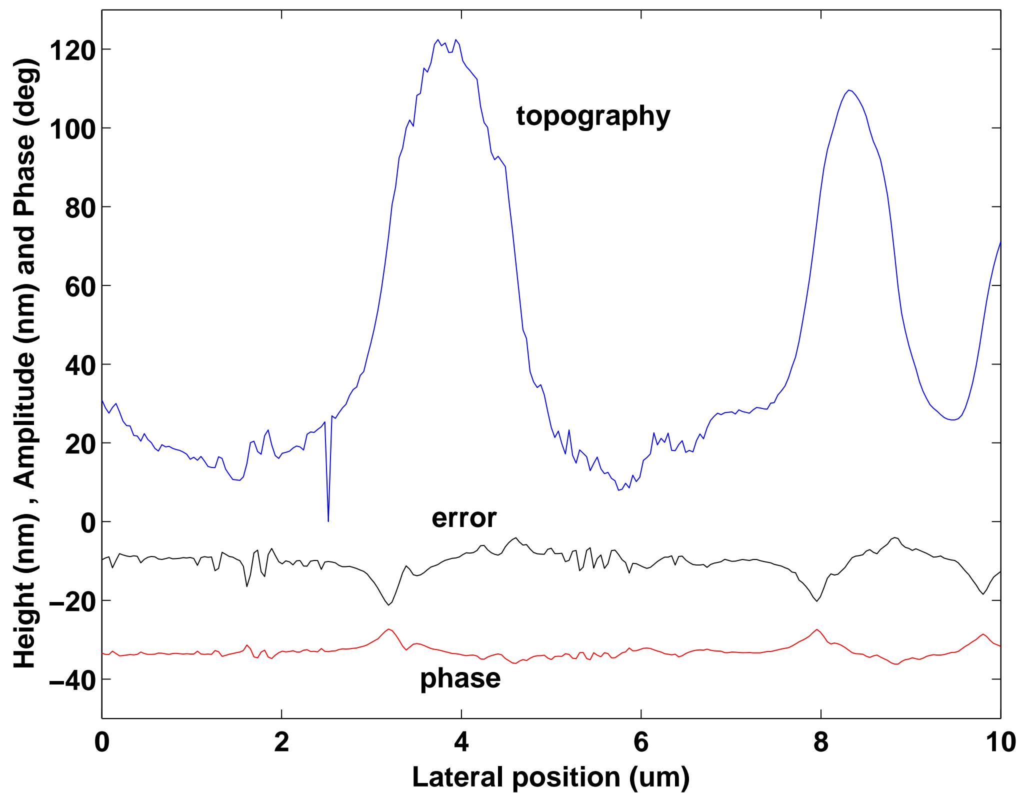

Figure 6.29: Surface topography (blue), error amplitude (multiplied by 10 to fit) (black), and phase (shifted arbitrarily) (red) variations across the line indicated in Fig. 6.27 (b).

We find that the phase signal is the same for the hills and the pits. It depends heavily on the error signal.

If we look at the histogram of the phase in Fig. 6.30 (c), there is no evidence that the sample is heterogeneous.

6.2.2 80:20 Polystyrene/Polyisoprene Blend

The optical micrographs of the second blend are shown in Fig. 6.31.

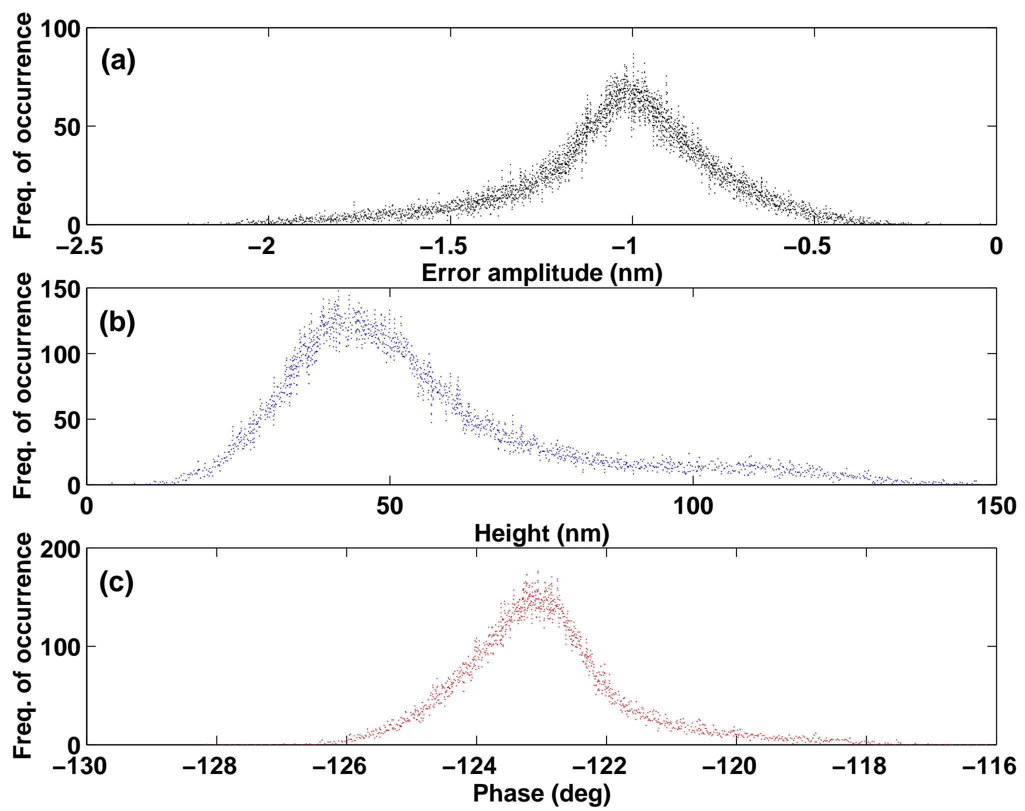

Figure 6.30: Histograms of (a) Error, (b) Surface height, and (c) Phase.

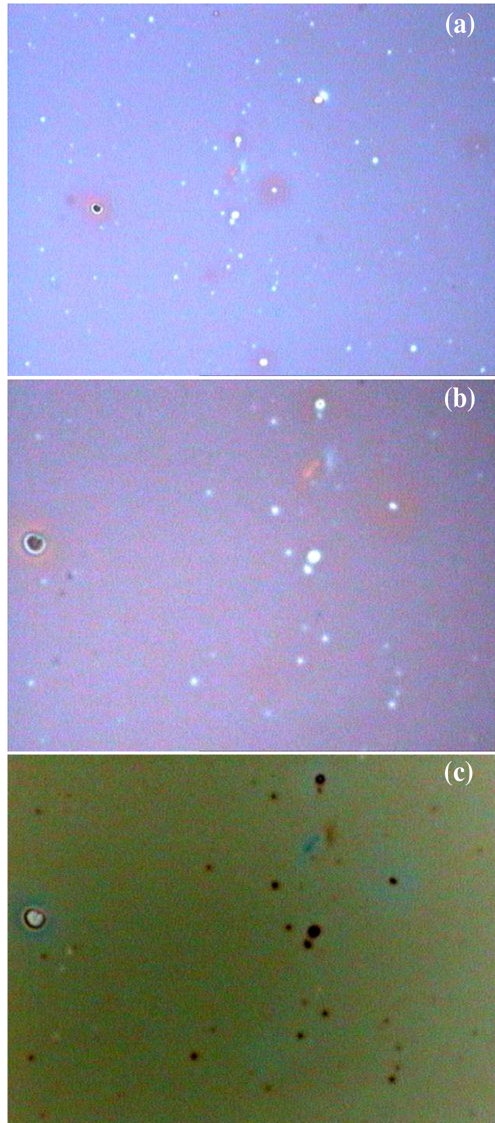

Figure 6.31: Optical micrographs of a 80:20 PS/PI blend at ×50 magnification in (a) and ×100 magnification in (b) and (c).

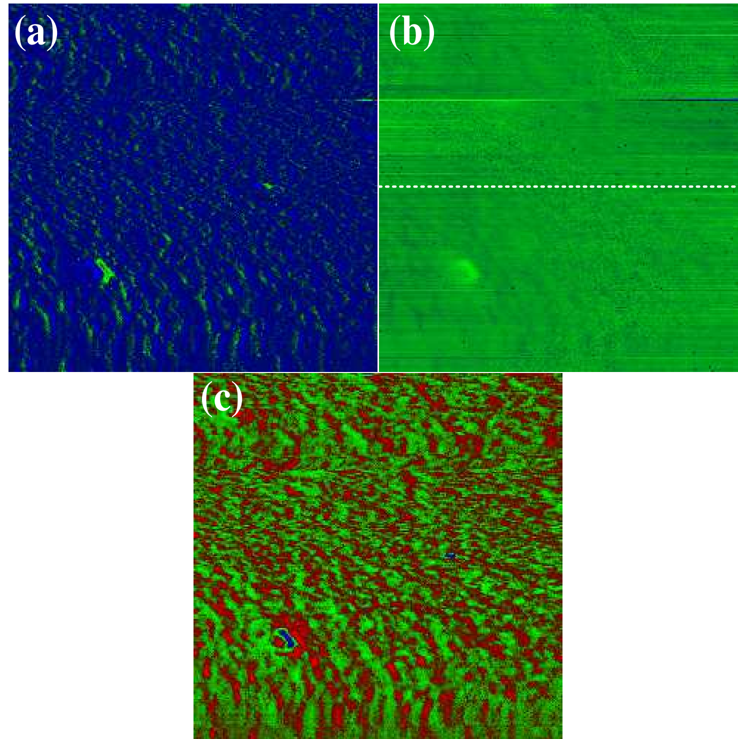

Figure 6.32: Enhanced third harmonic imaging of a 80:20 PS/PI blend. (a) Error, (b) Topography, and (c) Third harmonic amplitude. The variation from blue to red is 0.28 nm in (a), 230 nm in (b), and 0.07 nm in (c). Image parameters: Scan size = 10×10 μm, Pixel size = 256×256, Scan speed = 0.6 μm/s. Operating parameters: $A_0 \approx 2.4$ nm, $A_1/A_0 = 1.2$, $w = 0.97 w_{13}$.

6.2.2.1 Enhanced Third Harmonic Imaging

The result of this experiment is provided in Fig. 6.32. The topography image does not show any significant surface feature. But, the third harmonic image reveals some differences on the surface. This can be seen more easily in the three-dimensional views (Fig. 6.33).

The cross sections along the dashed line shown in Fig. 6.32 (b) are given in Fig. 6.34. The topography does not change too much. Third harmonic is also considered to be constant except at one point where there is a small hill on the surface.

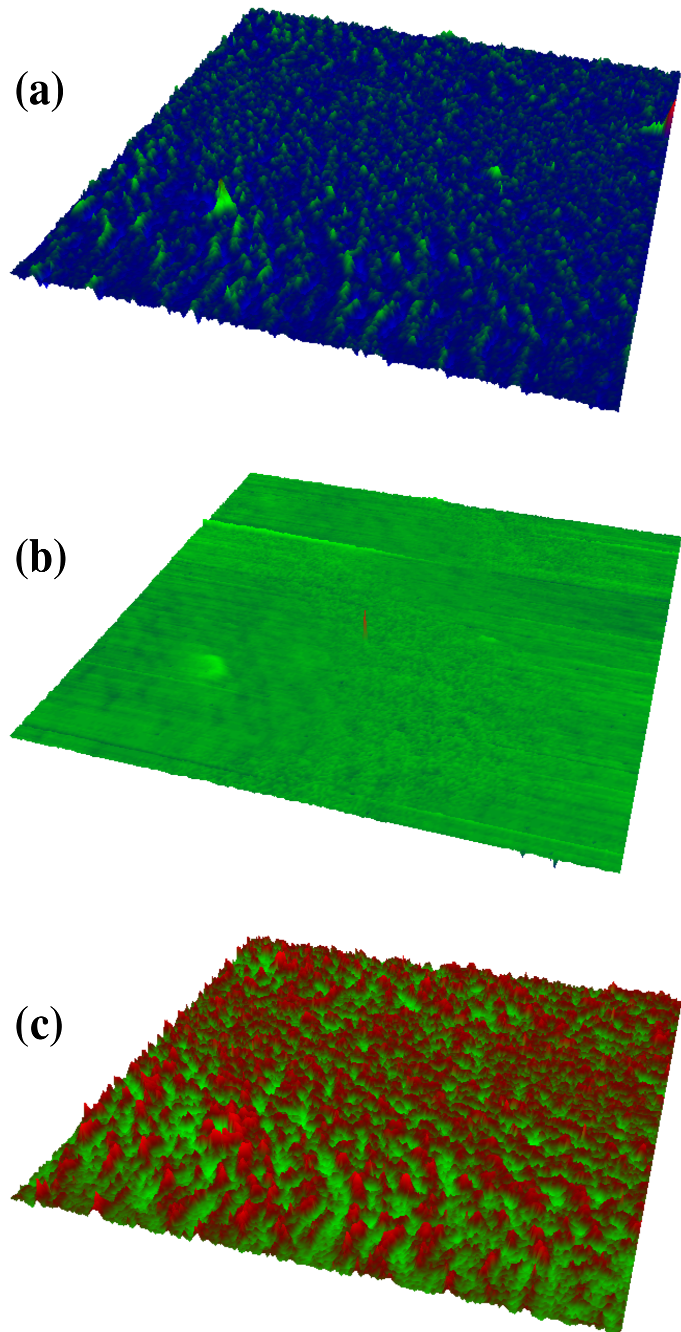

Figure 6.33: Three-dimensional views of the sample in Fig. 6.32. (a) Error, (b) Topography, and (c) Third harmonic amplitude.

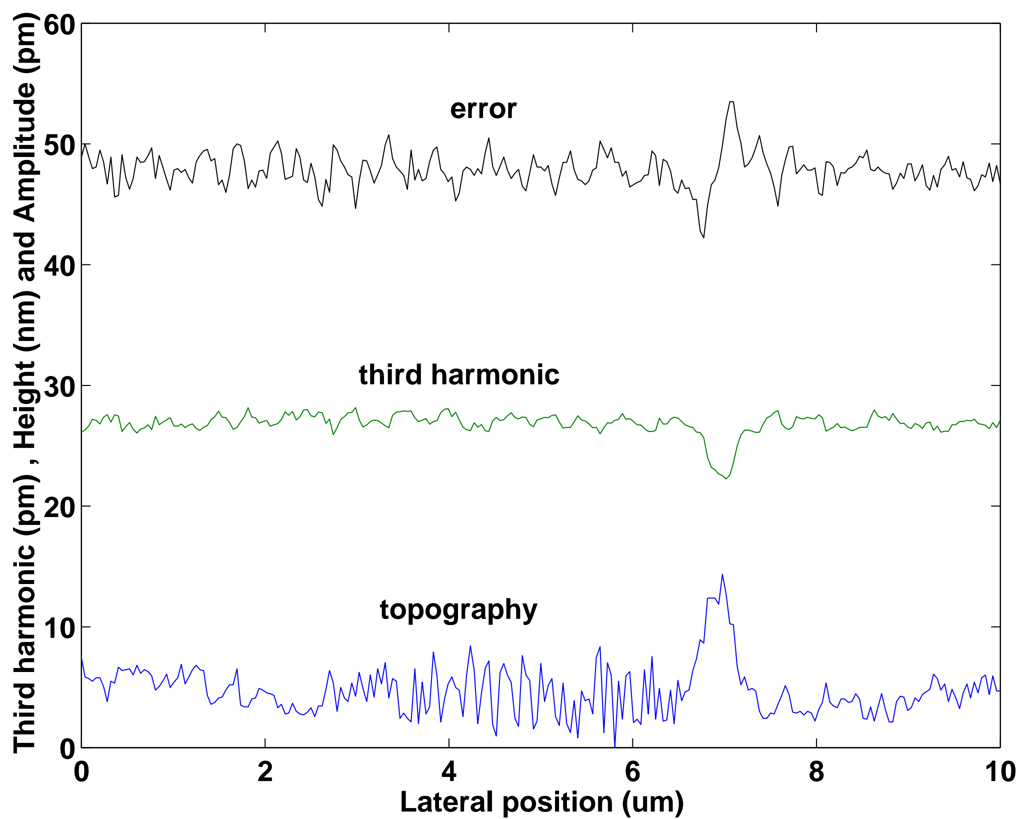

Figure 6.34: Third harmonic amplitude (divided by 10 to fit) (green), surface topography (blue), and error amplitude (divided by 10 to fit) (black) variations across the line indicated in Fig. 6.32 (b).

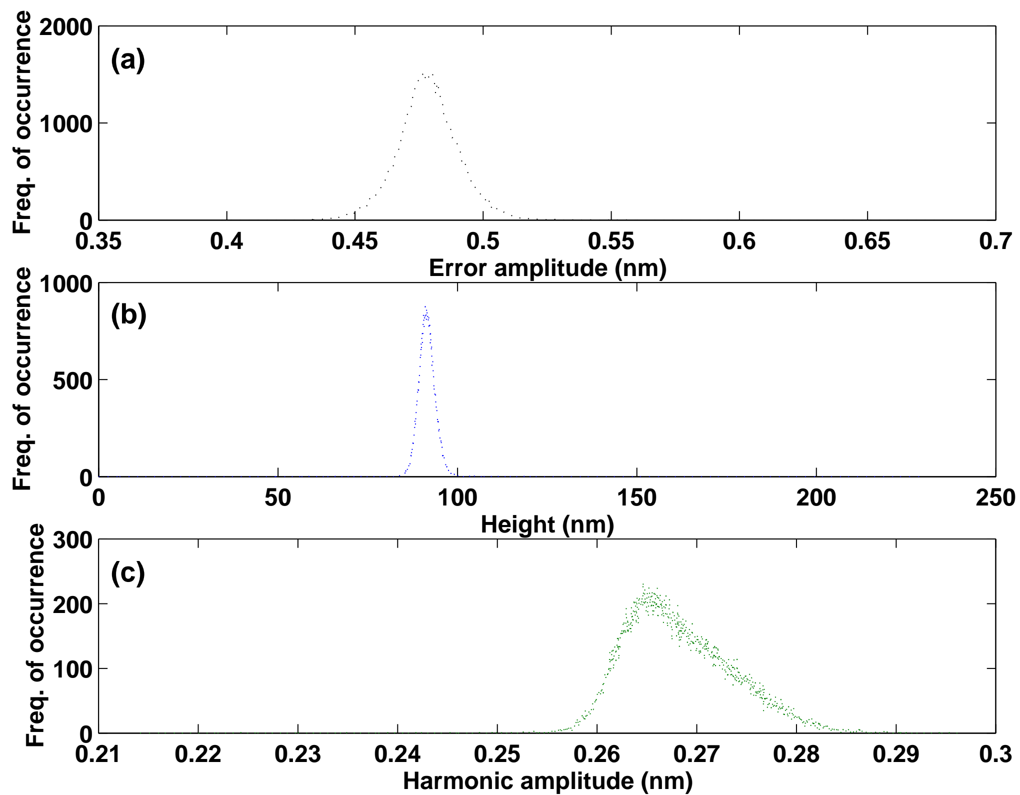

Figure 6.35: Histograms of (a) Error, (b) Surface height, and (c) Third harmonic.

By looking at the histograms in Fig. 6.35, we cannot say that the sample is heterogeneous. Notice that the average third harmonic amplitude for this sample is very close to that of low features in the first blend.

6.2.2.2 Conventional Tapping-mode Imaging

Error, topography, and phase images of the conventional tapping-mode mode are displayed in Fig. 6.36. We are not able to interpret the cause of the horizontal lines in the images. We performed a second experiment and observed similar anomalies. Except for the bumps, the surface can be considered to be relatively smooth.

The cross sections along the line indicated in Fig. 6.36 (b) are given in

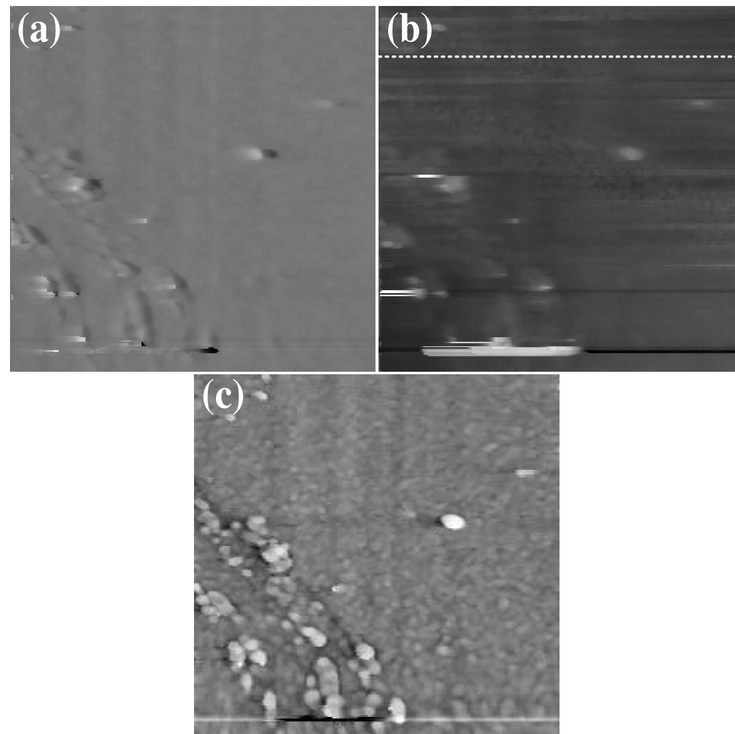

Figure 6.36: Conventional tapping-mode imaging of of a 80:20 PS/PI blend. (a) Error, (b) Topography, and (c) Phase. The variation from black to white is 1.7 nm in (a), 80 nm in (b), and 17° in (c). Image parameters: Scan size = 10×10 μm, Pixel size = 256×256, Scan speed = 0.6 μm/s. Operating parameters: $A_0 \approx 12.7$ nm, $A_1/A_0 = 0.84$, $w = w_1$.

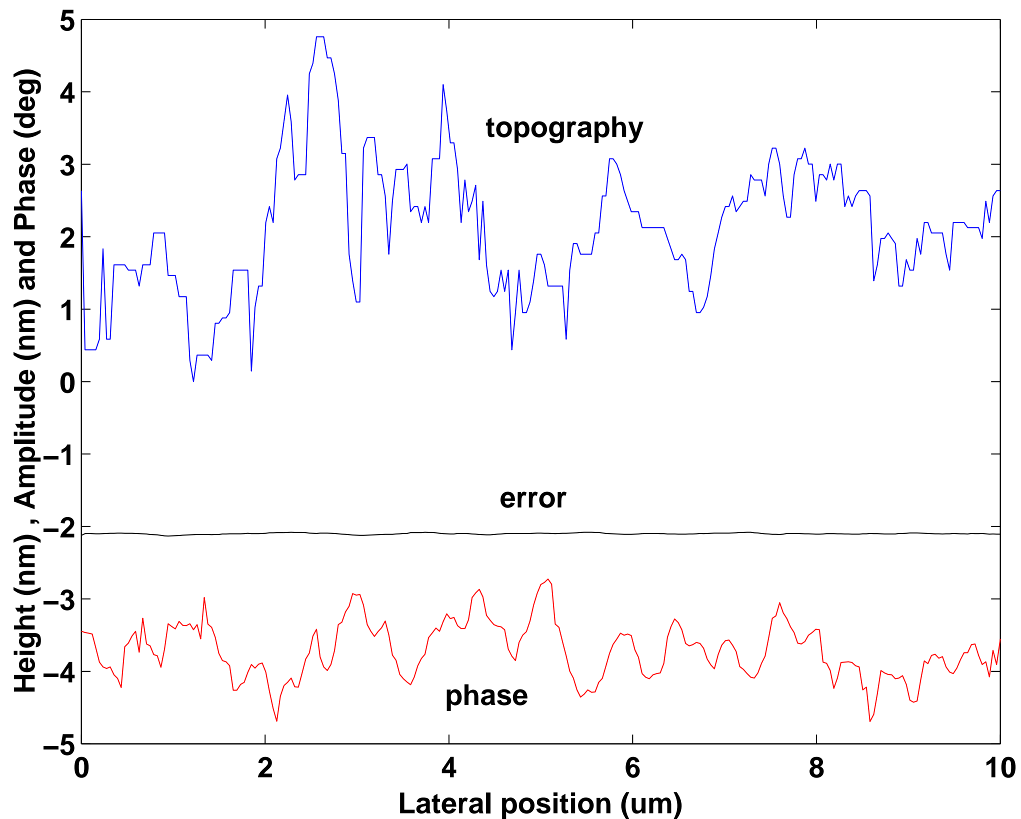

Figure 6.37: Surface topography (blue), error amplitude (black), and phase (shifted arbitrarily) (red) variations across the line indicated in Fig. 6.36 (b).

Fig. 6.37. The histograms are shown in Fig. 6.38. We see that both the topography and phase do not change too much.

6.2.3 50:50 Polystyrene/Polyisoprene Blend

The optical micrographs of the third blend are shown in Fig. 6.39.

6.2.3.1 Enhanced Third Harmonic Imaging

The enhanced third harmonic and topography images of 50:50 PS/PI blend are given in Fig. 6.40. In comparison to the first blend, we see that the domains

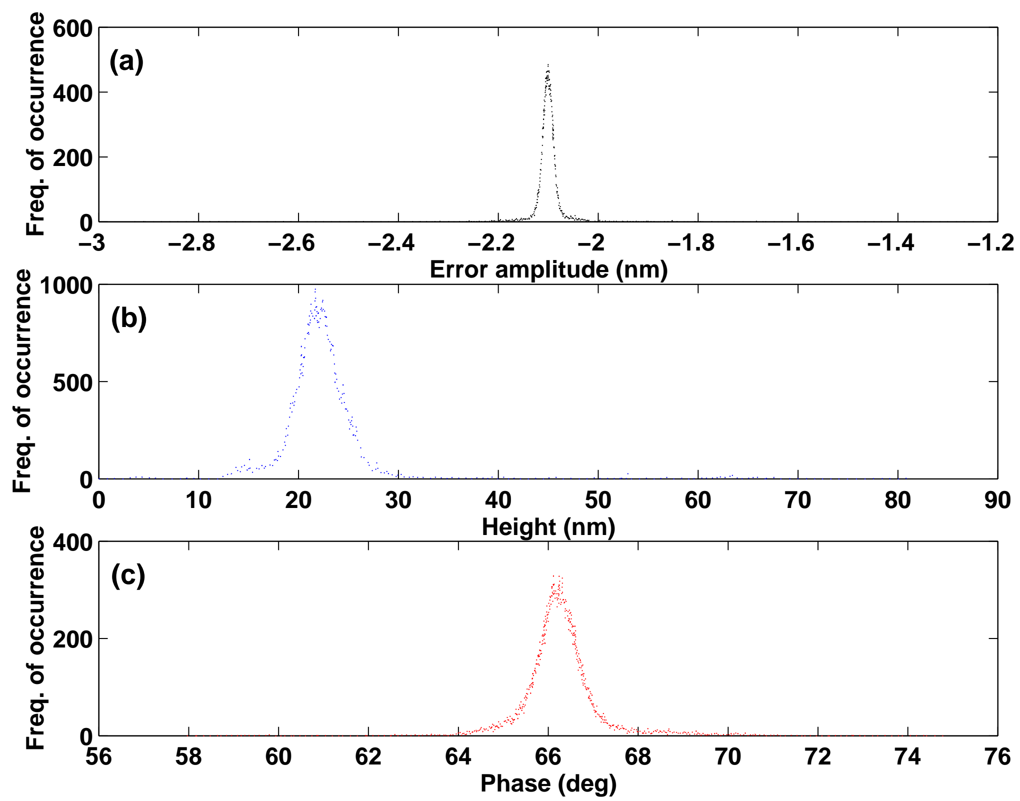

Figure 6.38: Histograms of (a) Error, (b) Surface height, and (c) Phase.

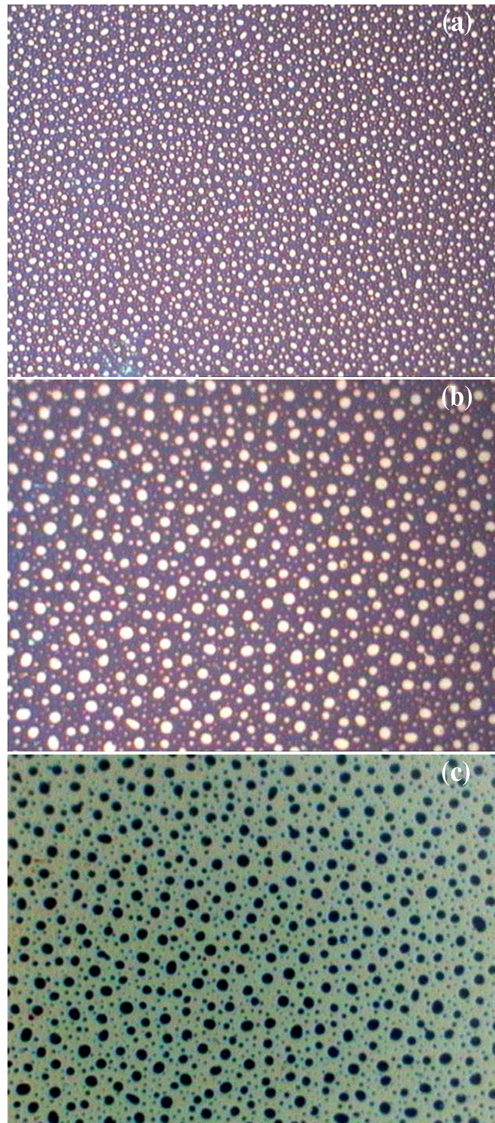

Figure 6.39: Optical micrographs of a 50:50 PS/PI blend at ×50 magnification in (a) and ×100 magnification in (b) and (c).

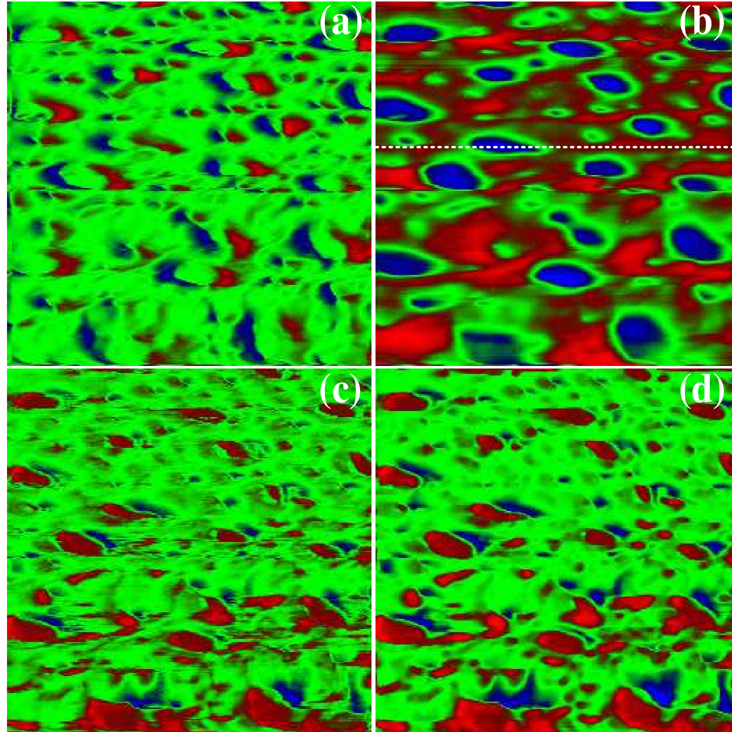

Figure 6.40: Enhanced third harmonic imaging of a 50:50 PS/PI blend. (a) Error, (b) Topography, (c) Third harmonic amplitude, and (d) Third harmonic amplitude (median filtered). The variation from blue to red is 1.2 nm in (a), 200 nm in (b), 0.28 nm in (c), and 0.2 nm in (d). Image parameters: Scan size = 10×10 μm, Pixel size = 256×256, Scan speed = 1 μm/s. Operating parameters: $A_0 \approx 2.4$ nm, $A_1/A_0 = 1.2$, $w = 0.97w_{13}$.

(circular regions) are lower than the surrounding region. Besides, the third harmonic amplitude is found to be higher in these domains. The domains are seen to be somewhat small compared to the ones in the topography image. In the error image, again we see that the fundamental amplitude increases or decreases as the tip intersects the edges of the domains.

For this sample, we also provided the reverse scan obtained during the same experiment in Fig. 6.41. The results are very close but not exactly the same due to the asymmetric tip profile. The median filtering in Fig. 6.41 (d) increases the visibility of the domains considerably.

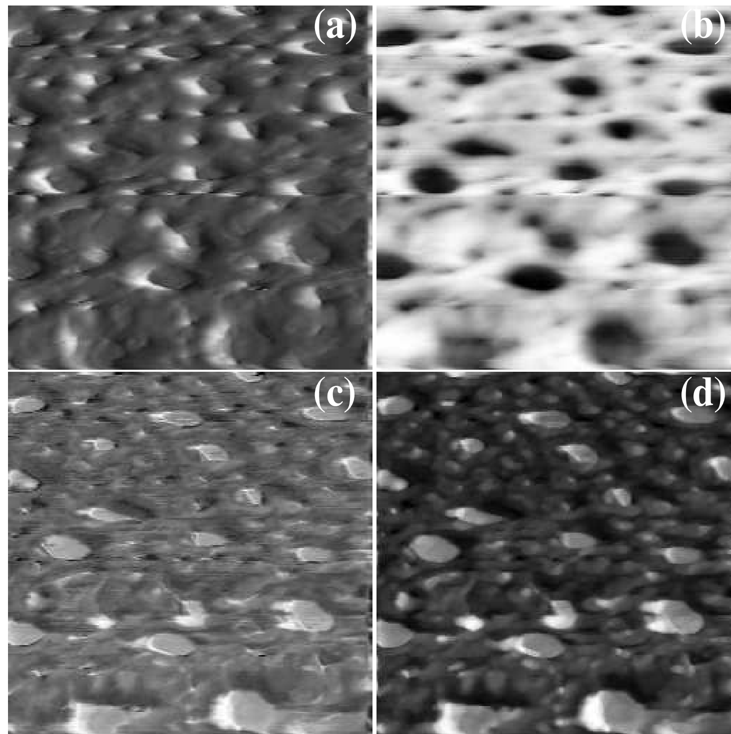

Figure 6.41: Reverse scan of the sample in Fig. 6.40. (a) Error, (b) Topography, (c) Third harmonic amplitude, and (d) Third harmonic amplitude (median filtered). The variation from black to white is 1.3 nm in (a), 200 nm in (b), 0.3 nm in (c), and 0.2 nm in (d).

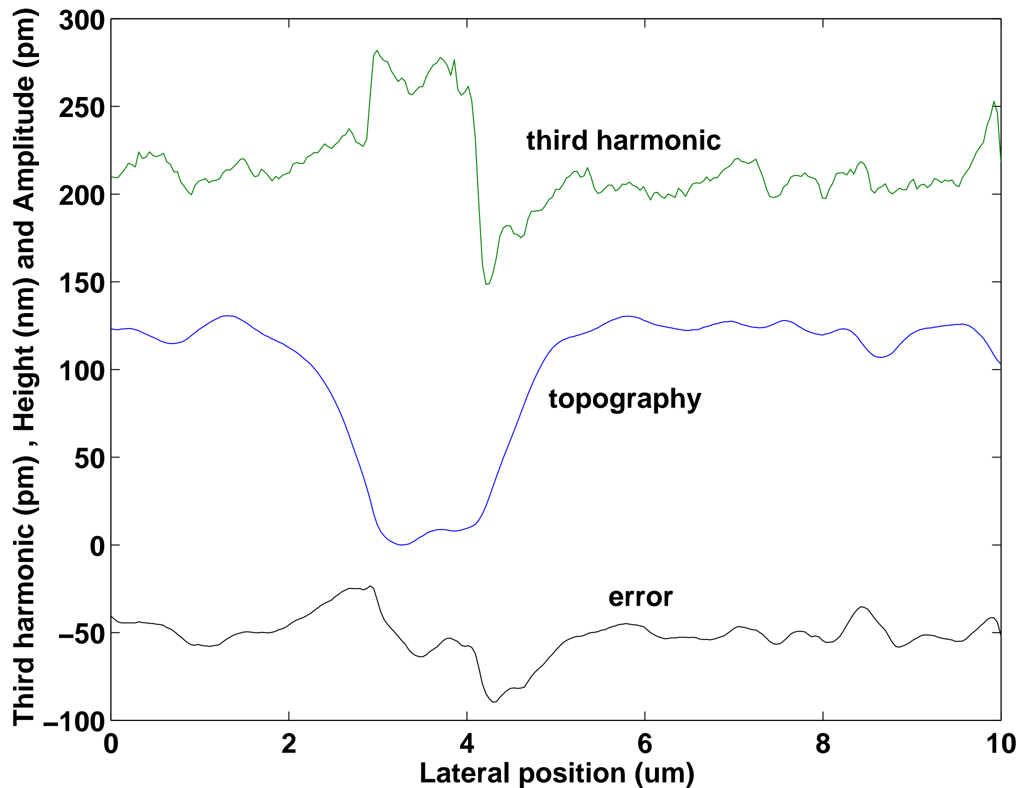

Figure 6.42: Third harmonic amplitude (green), surface topography (blue), and error amplitude (divided by -10 to fit) (black) variations across the line indicated in Fig. 6.40 (b).

Figure 6.42 shows the line [indicated in Fig. 6.40 (b)] profiles of the topography, third harmonic amplitude, and the error. We see that the enhanced third harmonic detects the material difference in a clear manner.

If we look at the histogram of the third harmonic [Fig. 6.43 (c)], we observe two things. First, the amplitude distribution reveals that the sample contains more than one material and most probably two materials (double humps). The hump on the right is smaller. Since this is a 50:50 mixture, one may expect to see two humps in equal magnitude. However, we recall that the domain sizes are relatively small in the third harmonic image and the scan size is also small. Second, the variation of third harmonic amplitude is in the same range of the first blend.

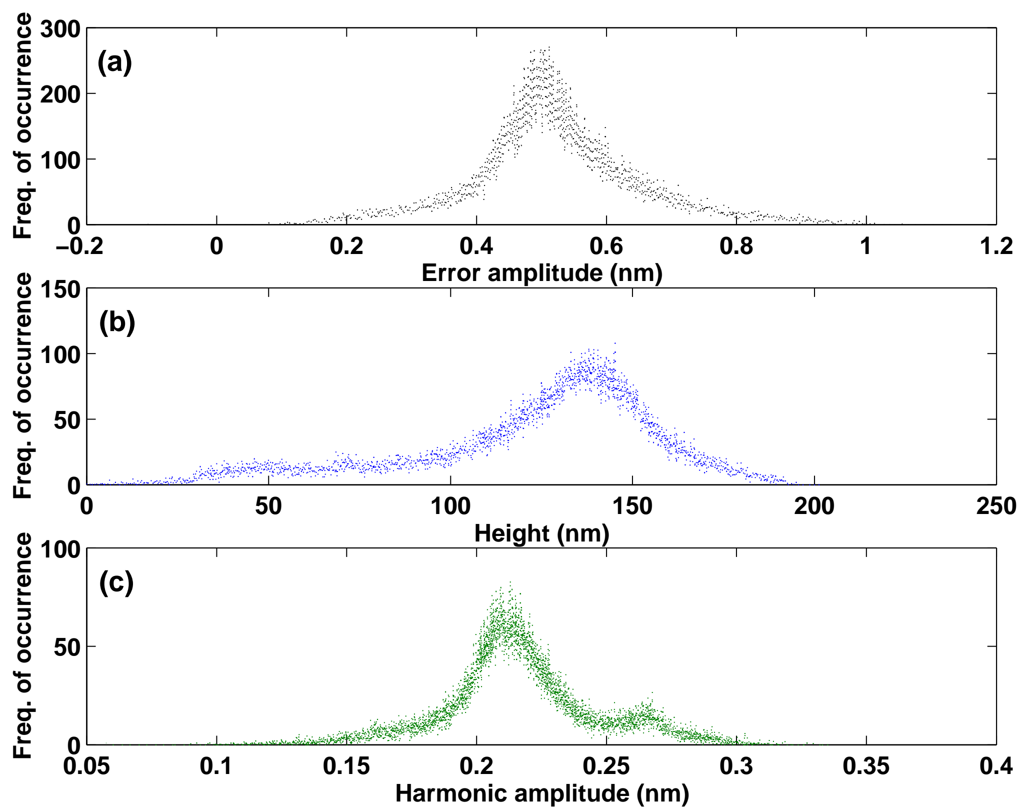

Figure 6.43: Histograms of (a) Error, (b) Surface height, and (c) Third harmonic.

6.2.3.2 Conventional Tapping-mode Imaging

The results of the conventional mode experiment are given in Fig. 6.44. The topography image shows similar surface structures as we obtained in the previous experiment. The empty region in the phase image is probably due to a software failure. We note that the features seen in the phase image do not come from the material heterogeneity, but rather due to the change in the fundamental amplitude during the scan (see the error image).

The line analysis is done for two sections indicated in Fig. 6.44 (c). Figure 6.45 corresponds to the vertical line and Fig. 6.46 corresponds to the horizontal line. We found that the phase does not show any difference for the low and high regions in the topography. It depends on the error signal.

The histograms are provided in Fig. 6.47. Although the phase variation is distributed in a wide range, we cannot say anything about the material heterogeneity from this data. Note that the small left hump comes from the error signal.

6.2.4 Polystyrene-*block*-Polyisoprene-*block*-Polystyrene Copolymer

The optical micrographs of the SIS block copolymer are shown in Fig. 6.48.

6.2.4.1 Enhanced Third Harmonic Imaging

The results for our last polymer sample are shown in Fig. 6.49. It has an interesting surface structure. The domains are well discriminated from the surroundings both in topography and third harmonic images. The variation of the error signal is in the same way as we described previously. Once again, we find that the third harmonic amplitude is larger in regions where the surface height is lower (see Fig. 6.50).

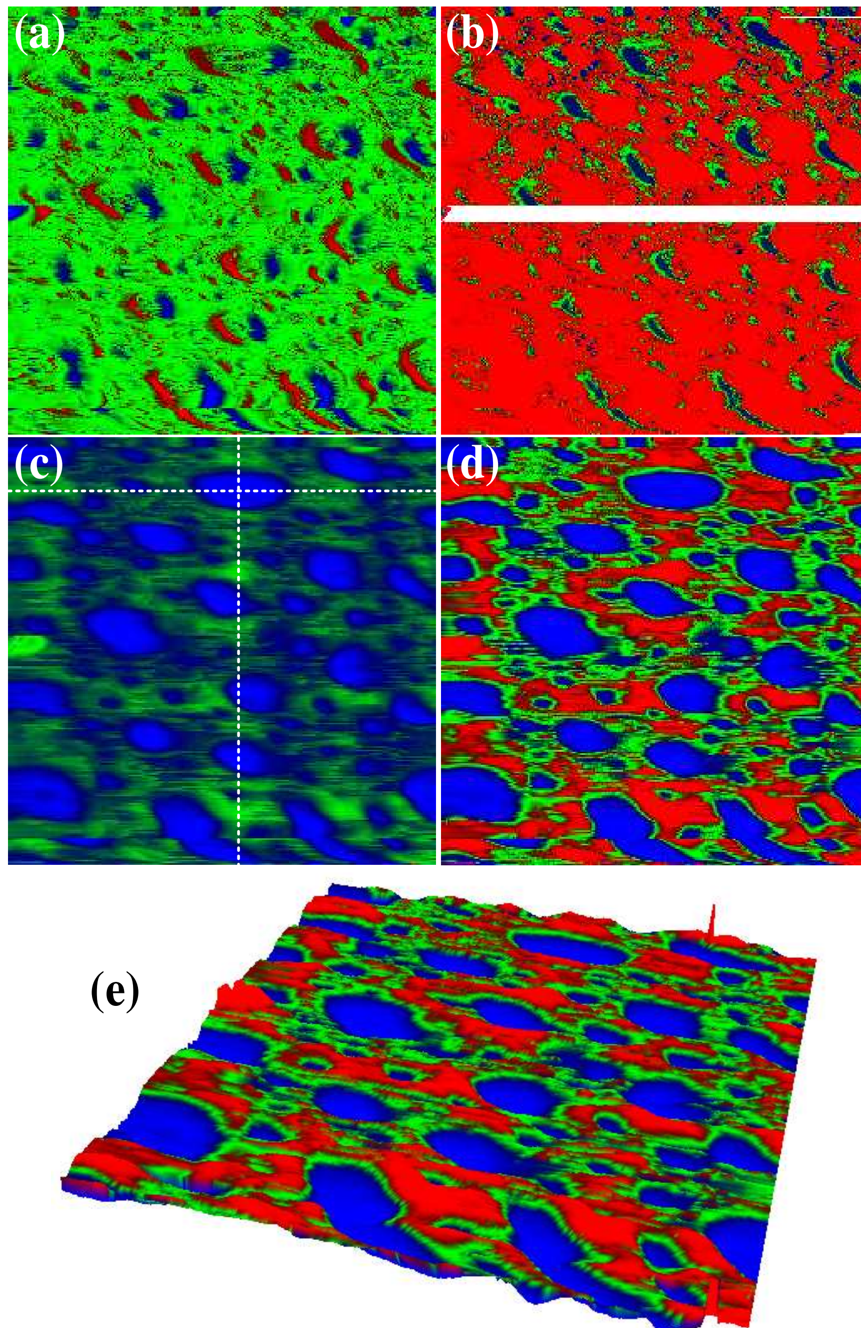

Figure 6.44: Conventional tapping-mode imaging of of a 50:50 PS/PI blend. (a) Error, (b) Phase, (c) Topography, (d) Topography (image contrast is enhanced), and (e) Three-dimensional view of topography (enhanced contrast). The variation from blue to red is 6 nm in (a), 98° in (b), and 500 nm in (c). Image parameters: Scan size = 10×10 μm, Pixel size = 256×256, Scan speed = 0.6 μm/s. Operating parameters: $A_0 \approx 8.7$ nm, $A_1/A_0 = 0.6$, $w = w_1$.

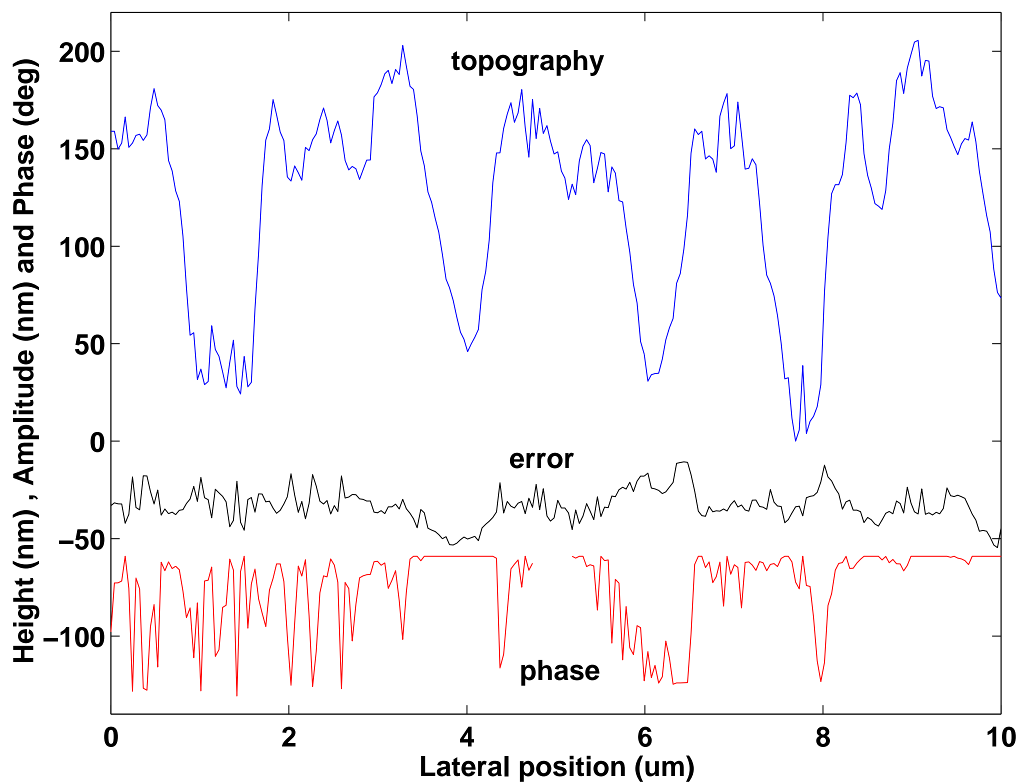

Figure 6.45: Surface topography (blue), error amplitude (multiplied by 10 to fit) (black), and phase (shifted arbitrarily) (red) variations across the vertical line indicated in Fig. 6.44 (c).

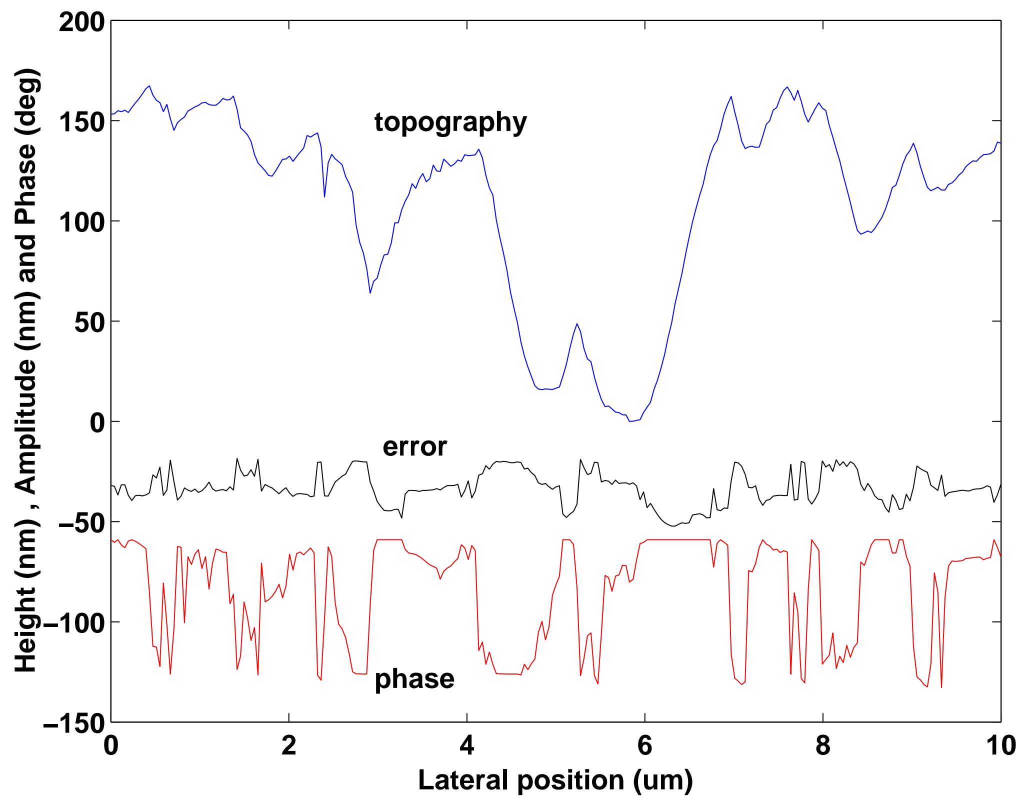

Figure 6.46: Surface topography (blue), error amplitude (multiplied by 10 to fit) (black), and phase (shifted arbitrarily) (red) variations across the horizontal line indicated in Fig. 6.44 (c).

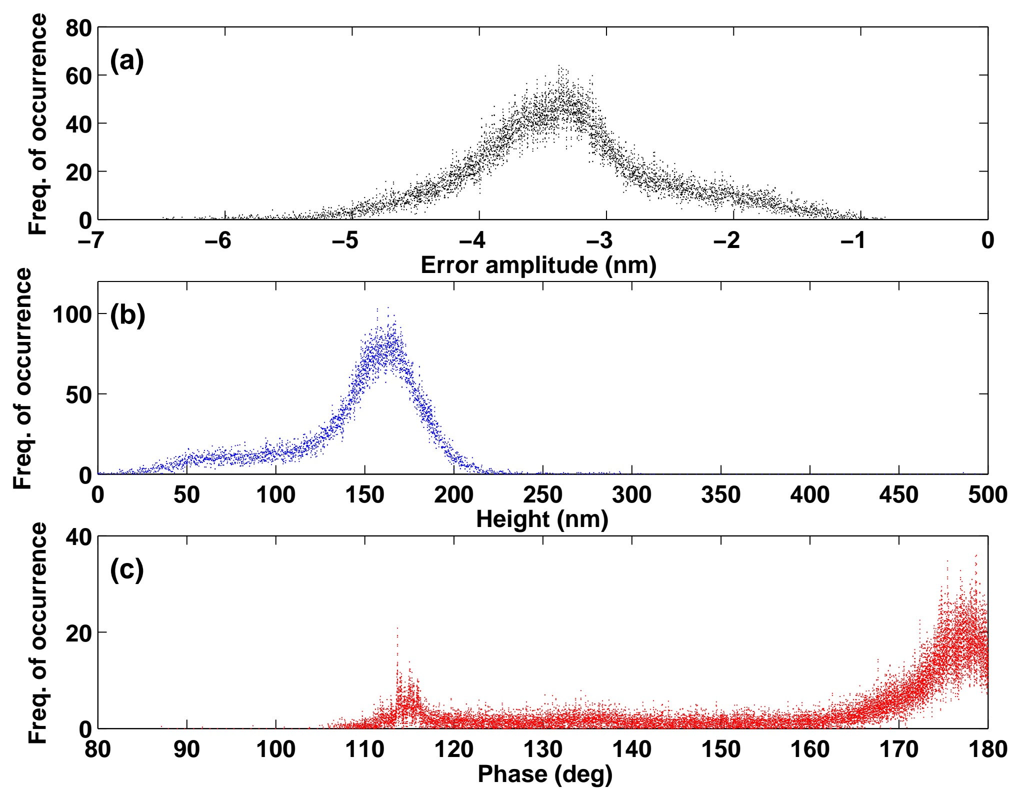

Figure 6.47: Histograms of (a) Error, (b) Surface height, and (c) Phase.

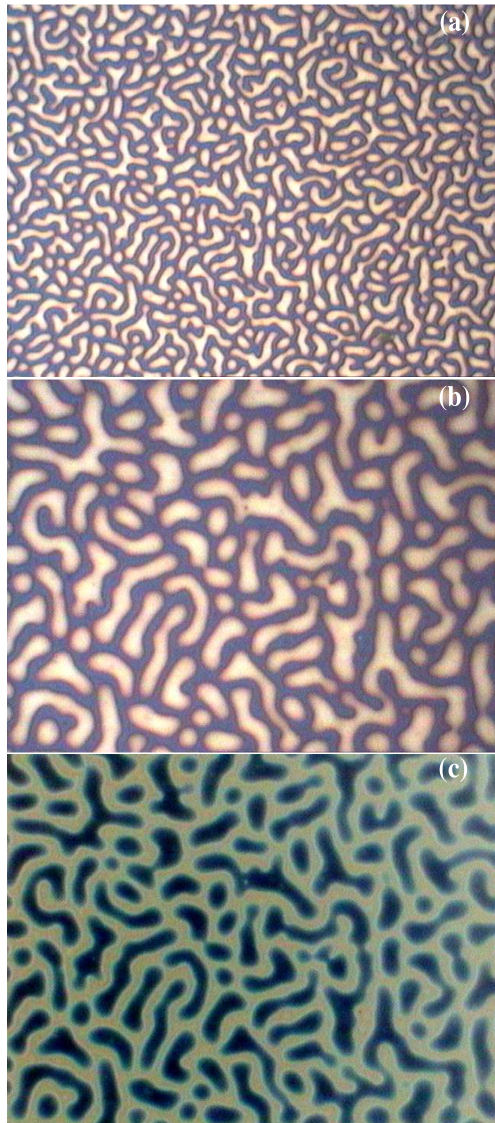

Figure 6.48: Optical micrographs of a SIS copolymer at ×50 magnification in (a) and ×100 magnification in (b) and (c).

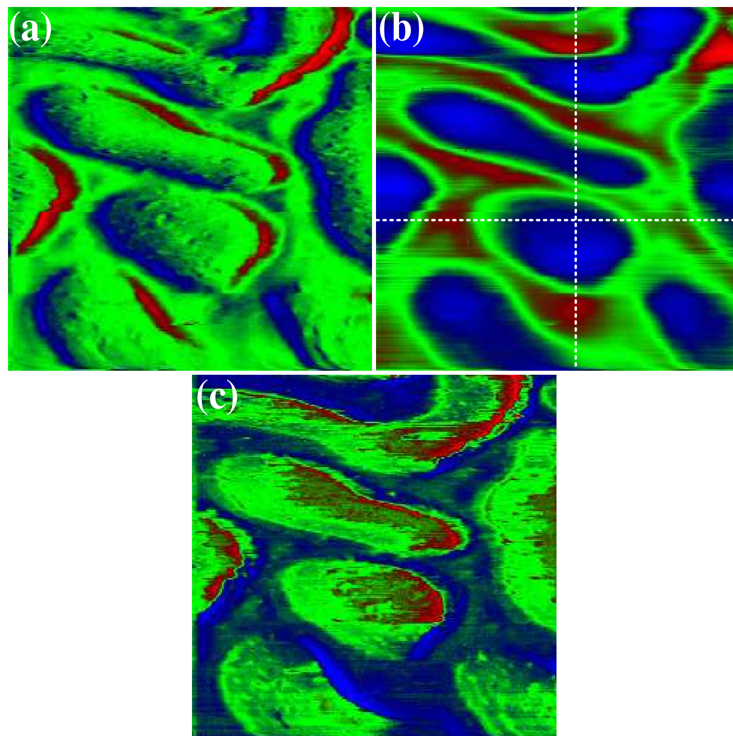

Figure 6.49: Enhanced third harmonic imaging of a SIS copolymer. (a) Error, (b) Topography, and (c) Third harmonic amplitude. The variation from blue to red is 0.65 nm in (a), 190 nm in (b), and 0.2 nm in (c). Image parameters: Scan size = 10×10 μm, Pixel size = 256×256, Scan speed = 1 μm/s. Operating parameters: $A_0 \approx 2.4$ nm, $A_1/A_0 = 1.2$, $w = 0.97w_{13}$.

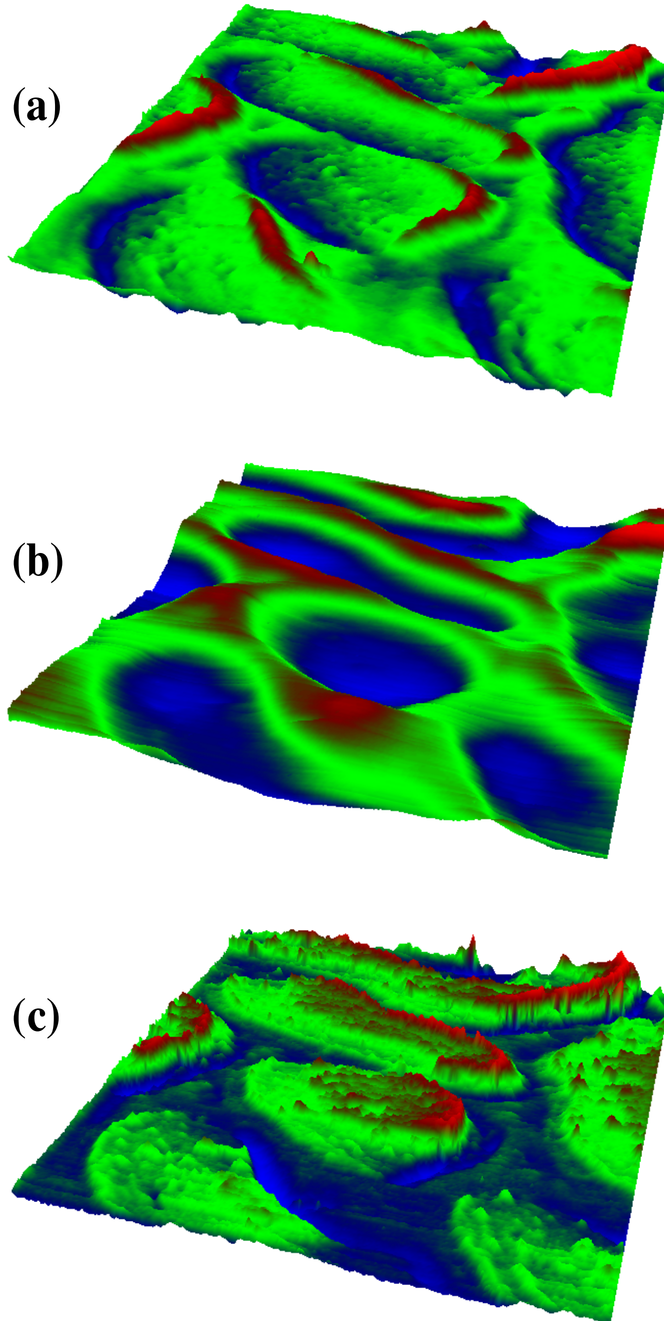

Figure 6.50: Three-dimensional views of the sample in Fig. 6.49. (a) Error, (b) Topography, and (c) Third harmonic amplitude.

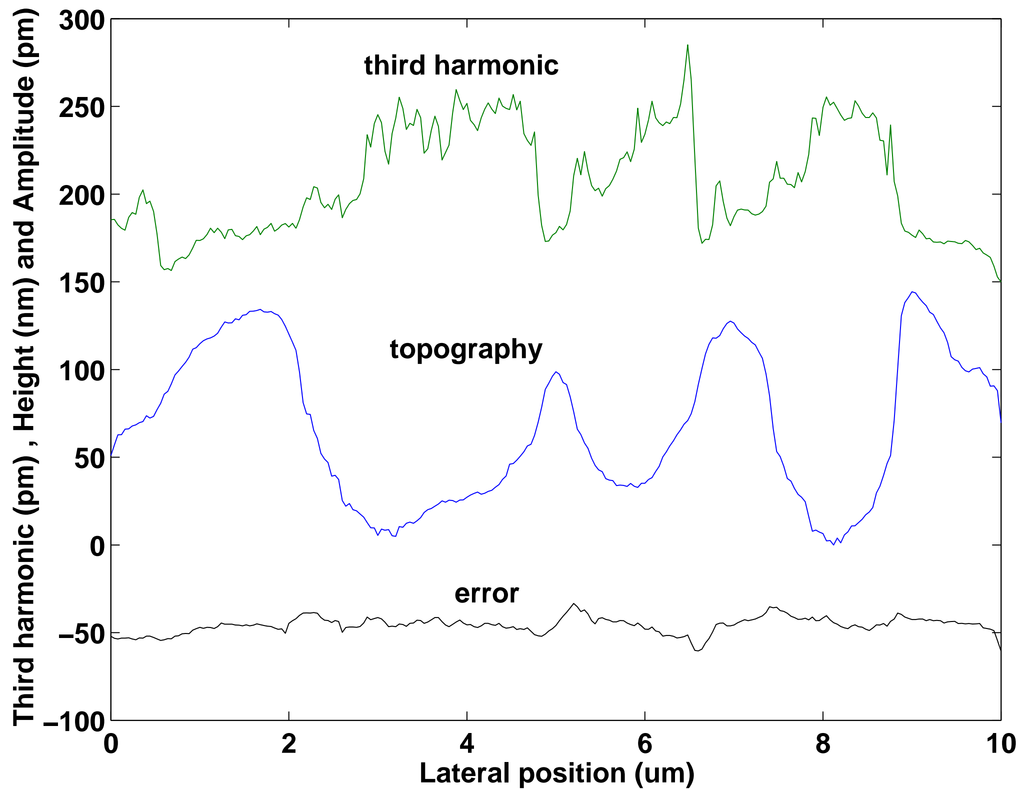

Figure 6.51: Third harmonic amplitude (green), surface topography (blue), and error amplitude (divided by -10 to fit) (black) variations across the vertical line indicated in Fig. 6.49 (b).

Figures 6.51 and 6.52 show the vertical and horizontal line [indicated in Fig. 6.49 (b)] profiles. The third harmonic again clearly detects the difference between the two materials. Not strictly speaking, the domains are not so smooth as one can infer from the topography profile.

The histogram of third harmonic in Fig. 6.53 (c) points out that the sample is heterogeneous and the amplitude distribution resembles the one that we found for the 50:50 blend.

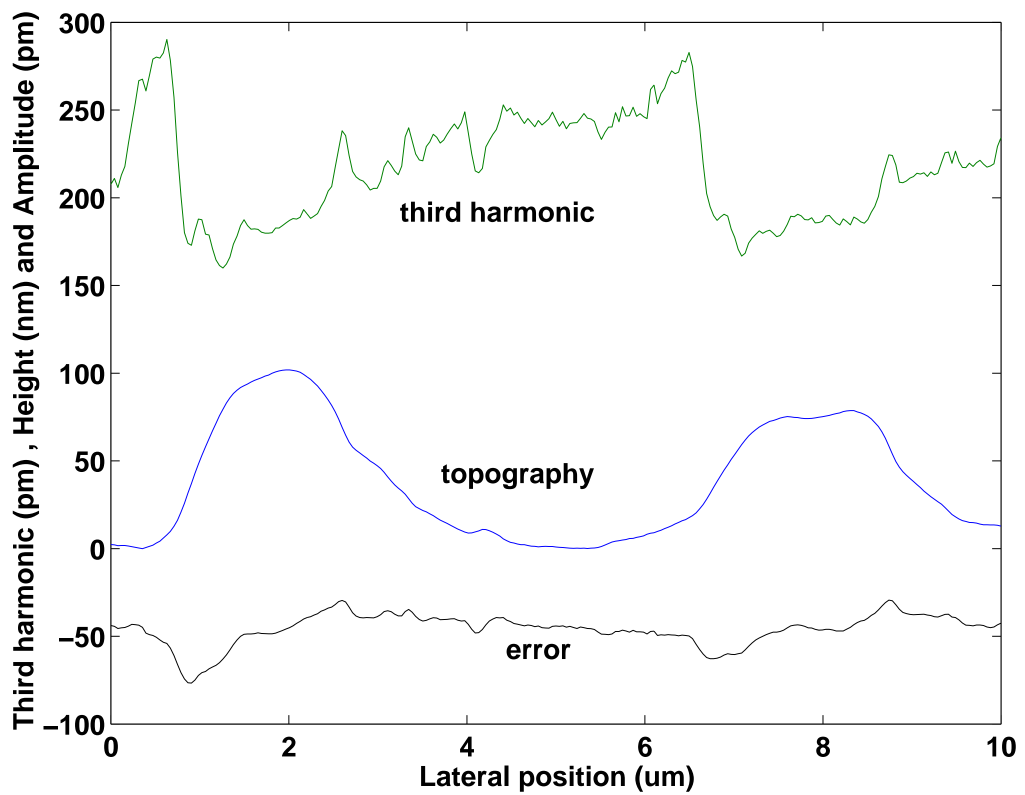

Figure 6.52: Third harmonic amplitude (green), surface topography (blue), and error amplitude (divided by -10 to fit) (black) variations across the dotted line indicated in Fig. 6.49 (b).

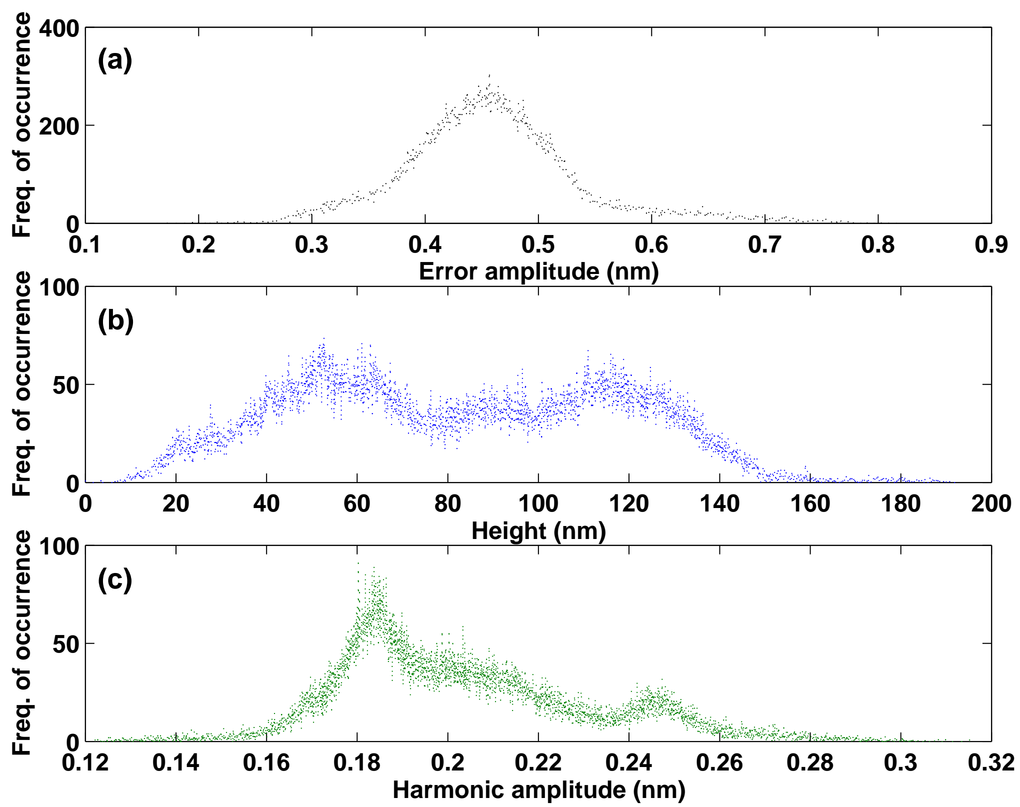

Figure 6.53: Histograms of (a) Error, (b) Surface height, and (c) Third harmonic.

6.2.4.2 Conventional Tapping-mode Imaging

The results of the conventional mode experiment are given in Figs. 6.54 and 6.55. The lower ends of the images seem to be blurred. This can be attributed to a possible mechanical drift explained in the previous chapter. The images in (d) and (h) are the inverted error images that we included to make a comparison with the phase image. The phase image contains the signs of the error image, but it is not exactly the same. The small dots in the domains of the phase image probably originate from the same source which caused the small protuberances seen in the phase image of 20:80 blend.

The cross sections corresponding to the line drawn in Fig. 6.54 (b) are given in Fig. 6.56. The histograms are provided in Fig. 6.57. By looking at either of these data, we can not say if the material is heterogeneous or not.

6.3 A Scratched Square-patterned GaAs Substrate

Our final sample is a homogeneous one, but its surface is scratched several times unintentionally. The optical micrographs of the sample are shown in Fig. 6.58 and the initial state of the sample is shown in Fig. 6.59. In the first experiment, we used a regular-patterned GaAs substrate which has smooth steps to make sure that the harmonic amplitude is not influenced by the surface height. This sample has also regular patterns on it, but the surface is not so smooth. The aim of this experiment is to show how the enhanced harmonic responds to the surface roughness.

The error, topography, and third harmonic amplitude images are shown in Fig. 6.60. The three-dimensional views are given in Fig. 6.61. We observe that the enhanced third harmonic signal recognizes even tiny surface features which is not available in the topography image. Moreover, on the average, the image contrast for the inside and outside regions of the rectangular areas are the same.

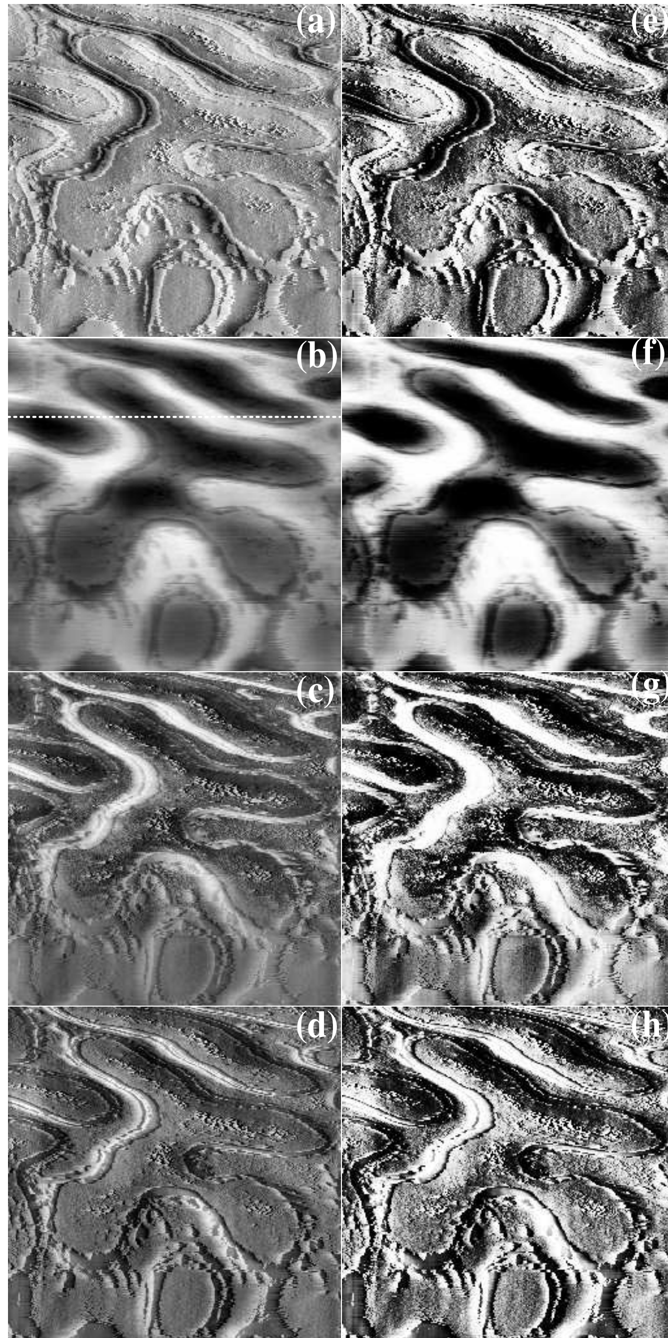

Figure 6.54: Conventional tapping-mode imaging of of a SIS copolymer. (a) Error, (b) Topography, (c) Phase, (d) Error (image contrast is reversed). The contrast of the images in (a)-(d) are enhanced by the software and the contrast enhanced images are shown in (e)-(h). The variation from black to white is 2.8 nm in (a), 160 nm in (b), and 56° in (c). Image parameters: Scan size = 10×10 μm, Pixel size = 256×256, Scan speed = 0.6 μm/s. Operating parameters: $A_0 \approx 10.5$ nm, $A_1/A_0 = 0.75$, $w = w_1$.

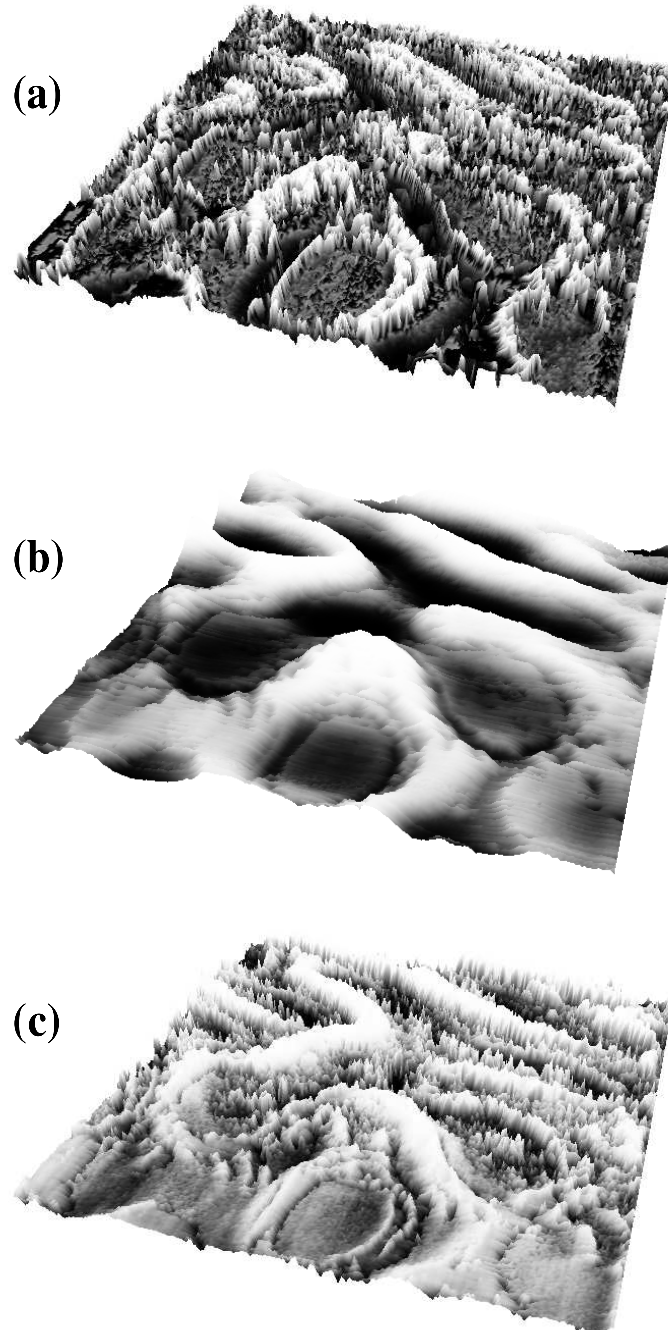

Figure 6.55: Three-dimensional views of the sample in Fig. 6.54. (a) Error, (b) Topography, and (c) Phase. The contrast in the images is enhanced.

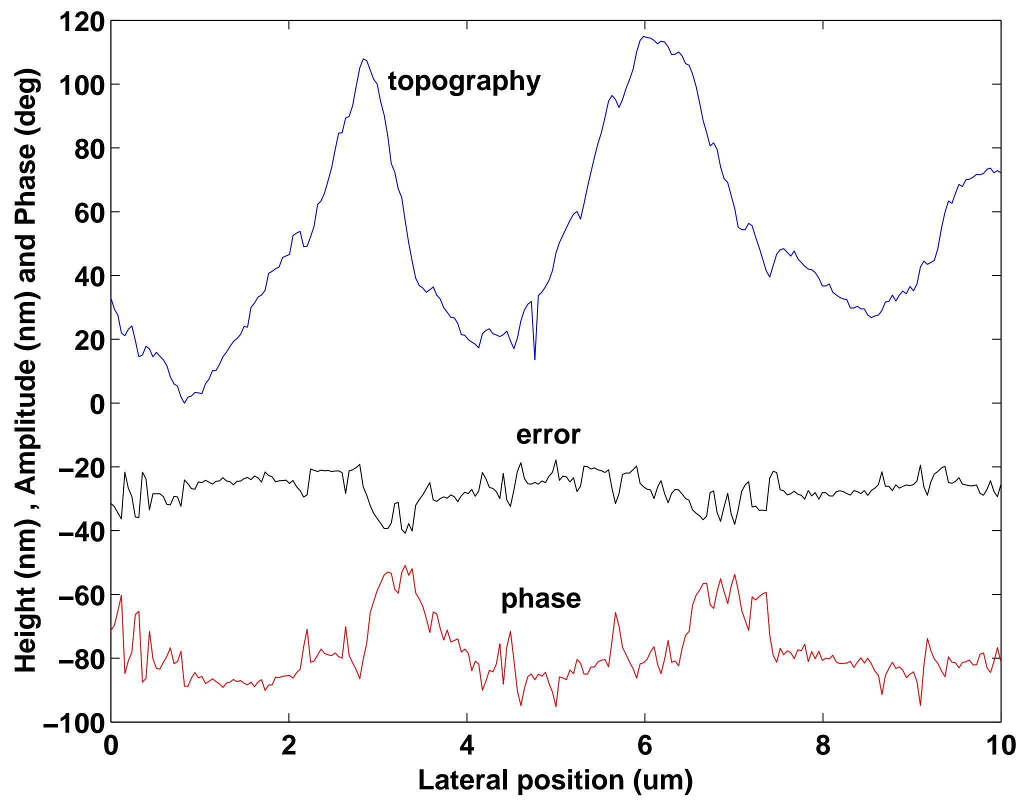

Figure 6.56: Surface topography (blue), error amplitude (multiplied by 10 to fit) (black), and phase (shifted arbitrarily) (red) variations across the line indicated in Fig. 6.54 (b).

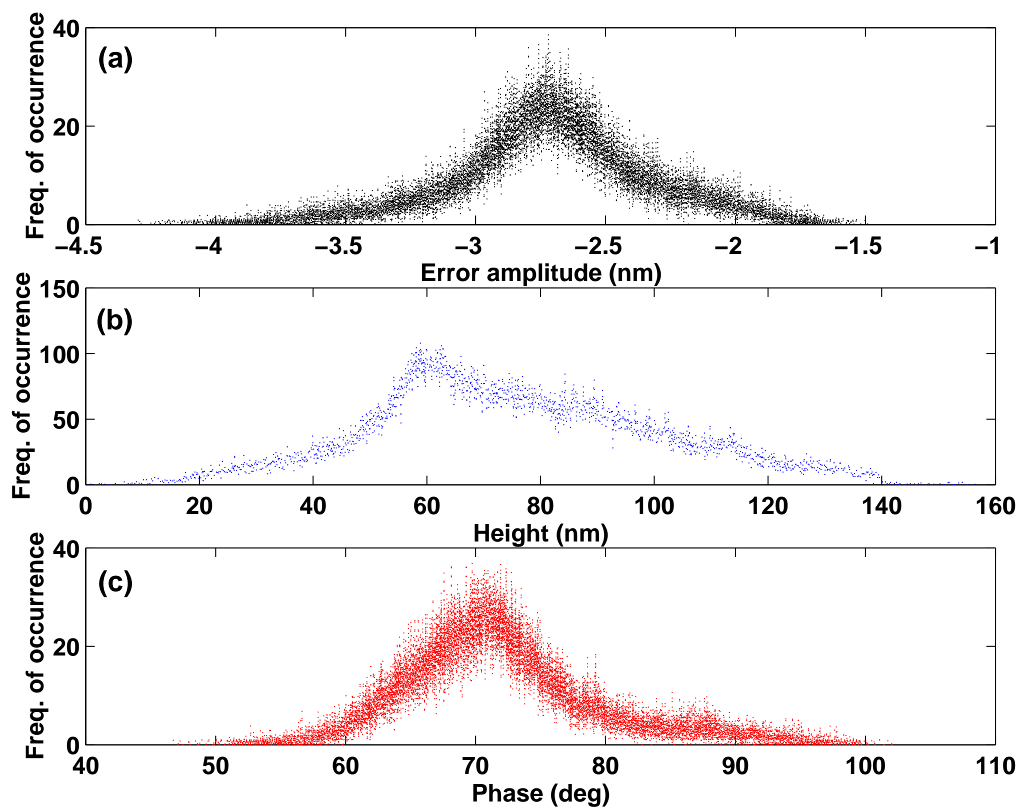

Figure 6.57: Histograms of (a) Error, (b) Surface height, and (c) Phase.

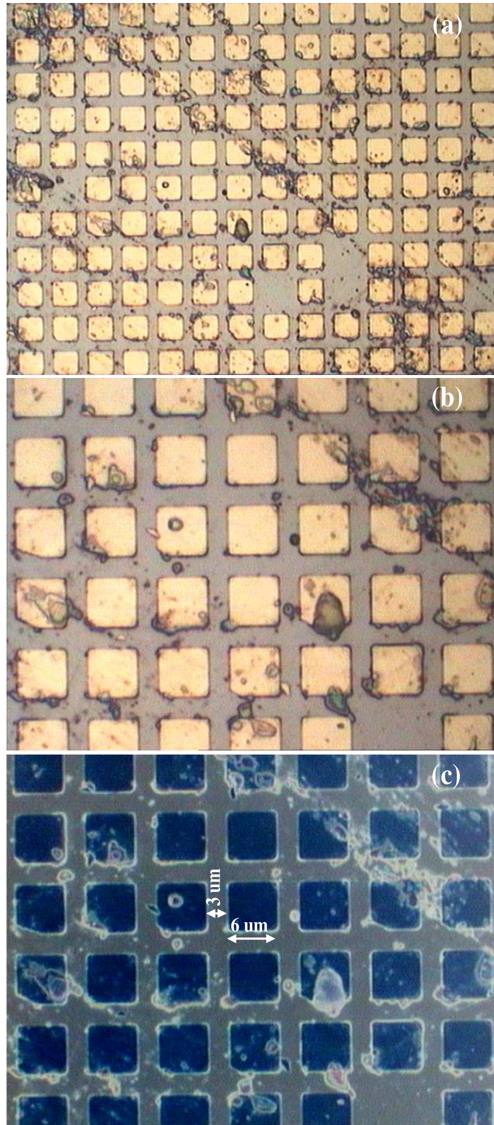

Figure 6.58: Optical micrographs of a scratched square-patterned GaAs substrate at ×50 magnification in (a) and ×100 magnification in (b) and (c).

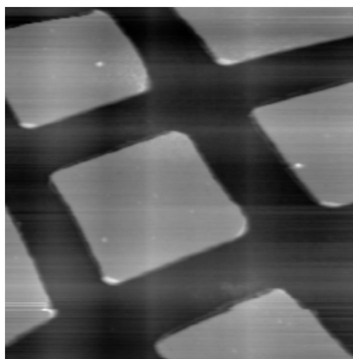

Figure 6.59: Previously taken topography image of the square-patterned GaAs substrate.

Figure 6.62 shows the line [indicated in Fig. 6.60 (b)] profiles of the topography, third harmonic amplitude, and the error. We see that the average value of the third harmonic does not change. On the other hand, it shows a great response for the small changes in the topography. It is worth to compare this result with the one obtained for the first sample. In that case, the topography variation is relatively smooth and the third harmonic changes significantly only at the edges. Hence we can say that the third harmonic is very sensitive to the surface roughness.

The histograms of this sample are provided in Fig. 6.63. Note the presence of a single hump in Fig. 6.63 (c). This indicates that the material uniformity is preserved throughout the scanned area.

We were not able to perform a conventional tapping-mode experiment for this sample. The reason is that the feedback circuit could not establish a stable operating point so that we can start the experiment. On the other hand, we succeeded in making an enhanced fourth harmonic imaging experiment. The results are displayed in Figs. 6.64 and 6.65.

We found that the enhanced fourth harmonic is also dependent strongly on the surface roughness. Unfortunately, the signal level is found to be small ($\sim$0.2 Å) compared to the third harmonic. That is why we did not perform fourth harmonic

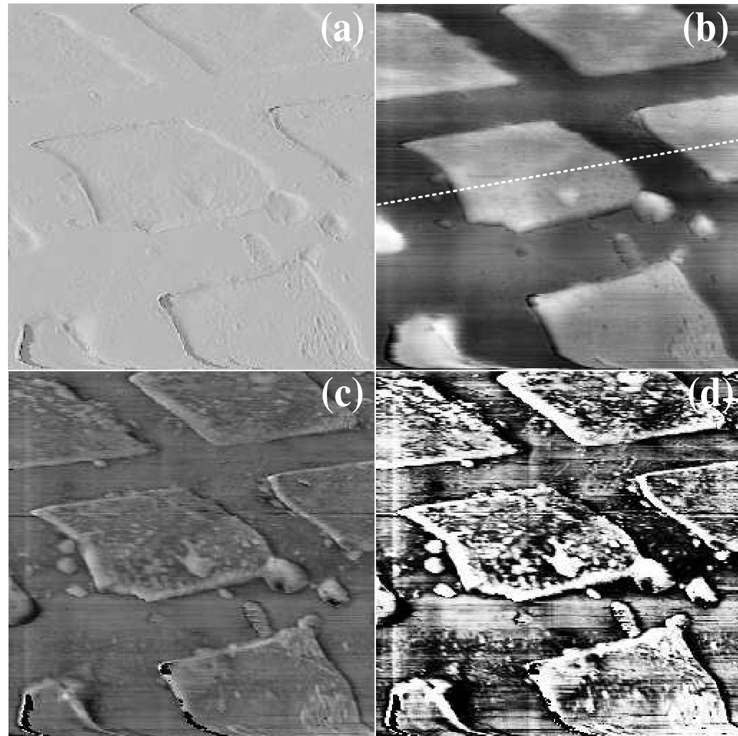

Figure 6.60: Enhanced third harmonic imaging of a scratched square-patterned GaAs substrate. (a) Error, (b) Topography, (c) Third harmonic amplitude, and (d) Third harmonic amplitude (image contrast is enhanced). The variation from black to white is 0.36 nm in (a), 320 nm in (b), and 0.91 nm in (c). Image parameters: Scan size = 15×15 μm, Pixel size = 256×256, Scan speed = 0.4 μm/s. Operating parameters: $A_0 \approx 2.1$ nm, $A_1/A_0 = 1.03$, $w = 0.97 w_{13}$.

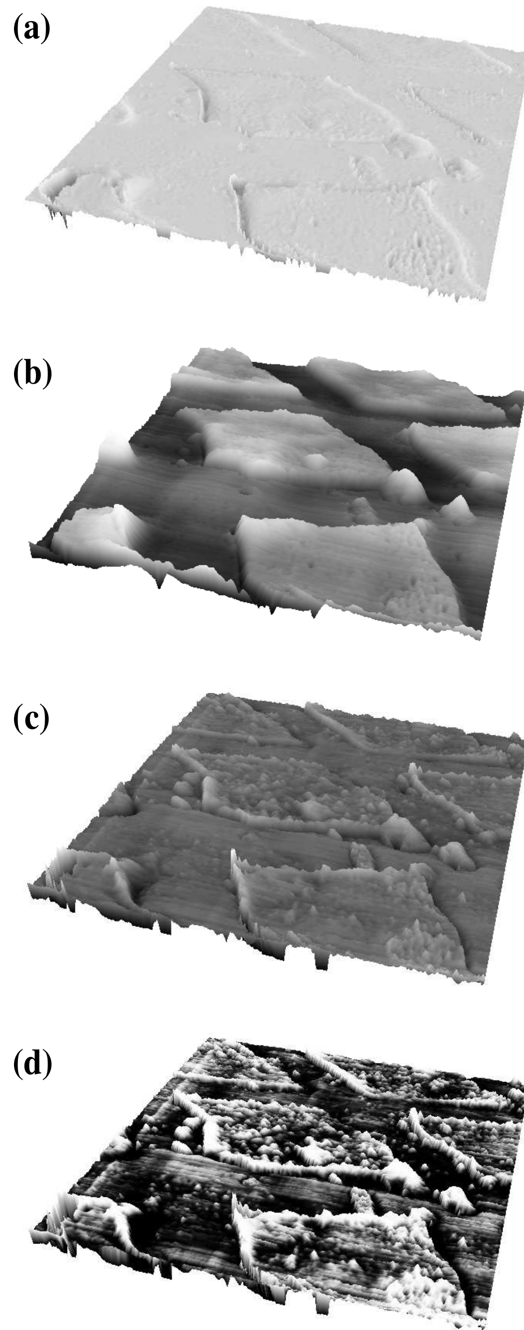

Figure 6.61: Three-dimensional views of the sample in Fig. 6.59. (a) Error, (b) Topography, (c) Third harmonic amplitude, and (d) Third harmonic amplitude (enhanced contrast).

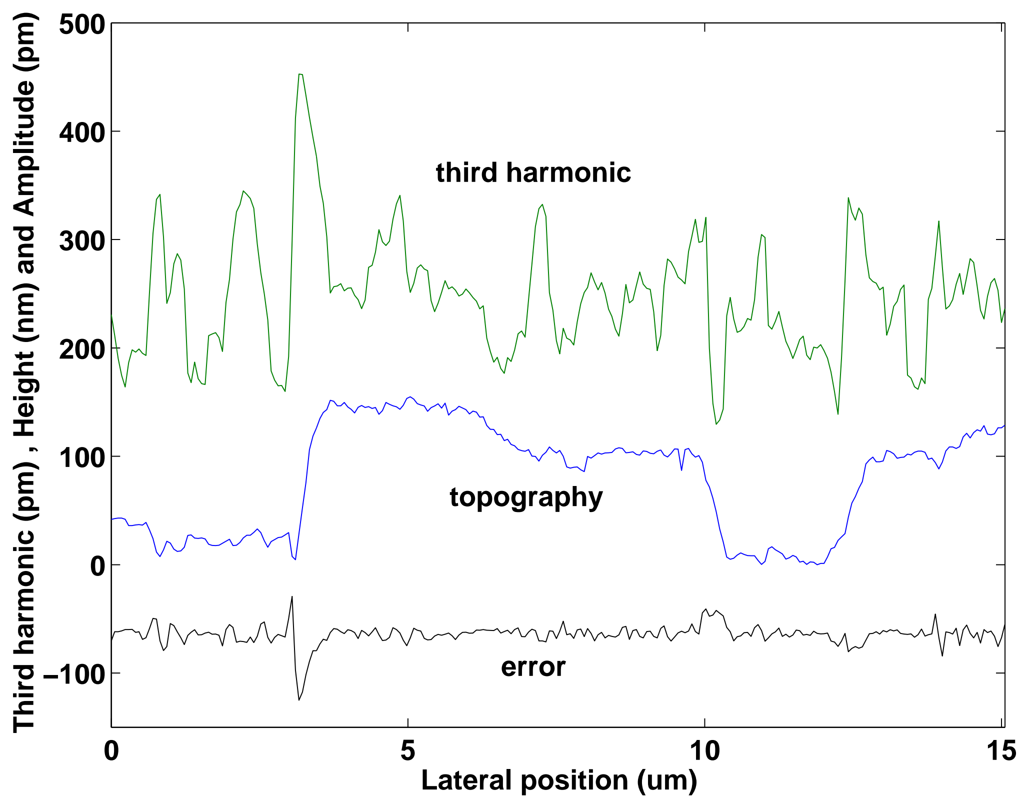

Figure 6.62: Third harmonic amplitude (green), surface topography (blue), and error amplitude (reversed) (black) variations across the line indicated in Fig. 6.59 (b).

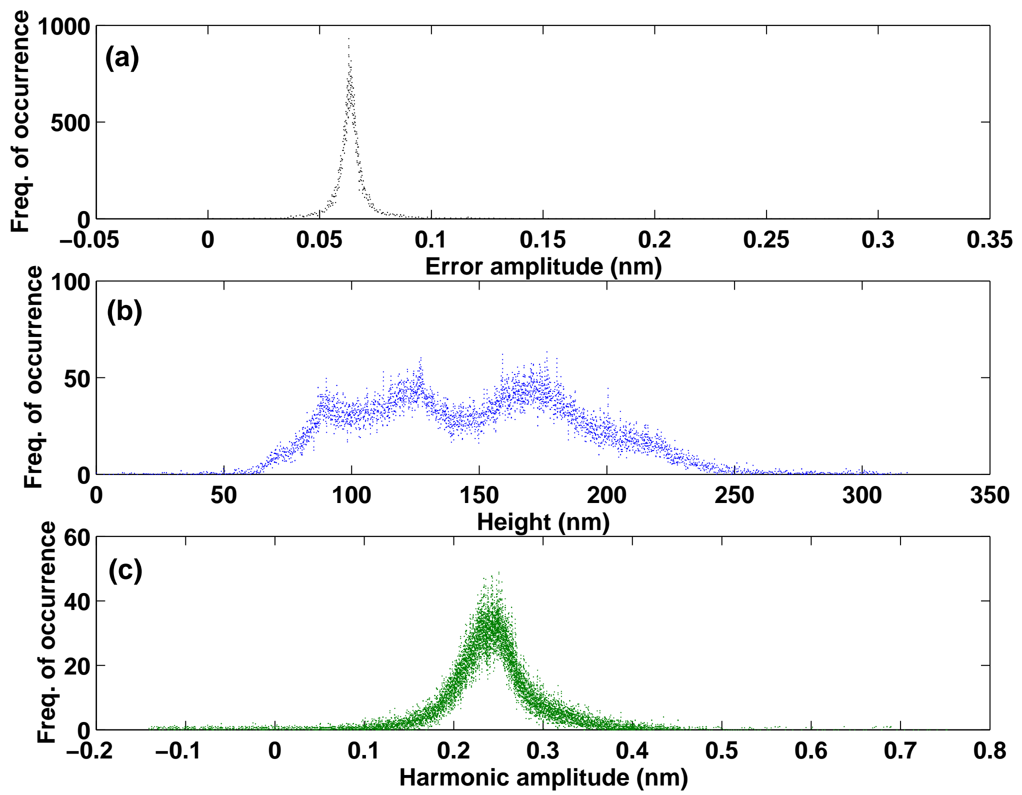

Figure 6.63: Histograms of (a) Error, (b) Surface height, and (c) Third harmonic.

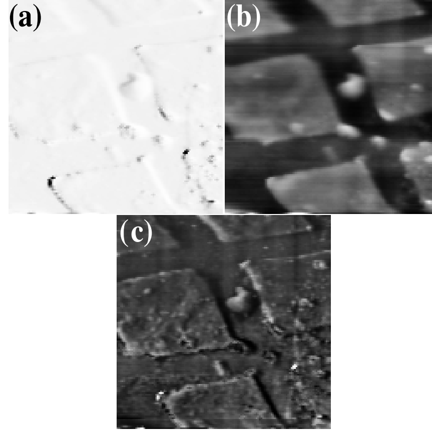

Figure 6.64: Enhanced fourth harmonic imaging of a scratched square-patterned GaAs substrate. (a) Error (low pass filtered), (b) Topography, and (c) Fourth harmonic amplitude (low pass filtered). The variation from black to white is 1.1 nm in (a), 340 nm in (b), and 0.09 nm in (c). Image parameters: Scan size = 15×15 μm, Pixel size = 128×128, Scan speed = 0.4 μm/s. Operating parameters: $A_0 \approx 3.8$ nm, $A_1/A_0 = 0.9$, $w = 0.97w_{14}$.

imaging experiments for the other samples.

6.4 Summary and Discussion

In this chapter, we tested our method on a variety of samples. We chose to utilize the third harmonic to characterize the samples. Because, signal levels of the fourth and fifth harmonics are found to be relatively small. For the second harmonic, we could not excite the cantilever at a reasonable oscillation amplitude. Probably, there is a dip in the transfer function of the cantilever around one half of its resonance frequency. We did not consider the harmonics higher than the fifth harmonic.

In the enhanced harmonic imaging experiments, the set point amplitudes (A_1) are found to be larger than the free oscillation amplitudes (A_0) except for the fourth harmonic imaging experiment of the last sample. Note that we drive the

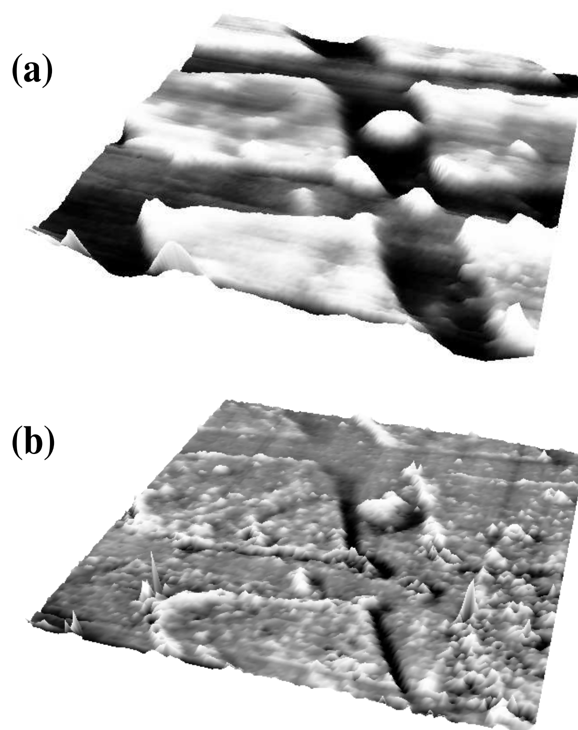

Figure 6.65: Three-dimensional views of the sample in Fig. 6.64. (a) Topography and (b) Fourth harmonic amplitude. The contrast in the images is enhanced.

cantilever below its resonance frequency. When the cantilever is excited below the resonance, its amplitude can increase [110] if the fundamental component of the tip-sample force is in-phase with the tip oscillation assuming that only conservative forces take place in the interaction. To explain it more clearly, assume that the oscillation amplitude is so small that the interaction force can be approximated with a linear spring which shifts the resonance frequency by an amount that is proportional to the negative gradient of the interaction force [32]. If the force gradient is positive (as in the case of attractive van der Waals forces), then there will be a decrease in the resonance frequency. But, if the force gradient is negative (as in the case of repulsive contact forces), then there will be an increase in the resonance frequency. Hence, by assuming a Lorentzian form of the cantilever transfer gain around the resonance, the attractive surface forces can result in an increase in the oscillation amplitude if the excitation is below the resonance. Note that the increase in the oscillation amplitude does not mean that the tip-sample contact does not occur. It means that the interaction is dominated by the attractive surface forces.

Suppose that the tip stayed in purely attractive regime like the one seen in Fig. 2 of chapter 3. Let us further assume that only the vdW forces act on the tip. The strength of the vdW forces decays with the square of the distance. The nonlinearity (the slope of the forces) decays with the cube of the distance. By utilizing the relation between the fundamental component of the interaction force and the third harmonic amplitude (third harmonic of the interaction force multiplied by the transfer gain) one can obtain the mean tip-sample distance. From this mean distance and measured amplitude one can determine the Hamaker constant. By using this simple and unrealistic approach we obtained very high Hamaker constants which are around two orders of magnitude larger than the typical values.

We know that the tip-sample interaction in our experiments is not dominated by an elastic force since the oscillation amplitudes are relatively low and it is found that there is an increase in the oscillation amplitude. Furthermore, the above approach which takes only the vdW forces into account does not yield realistic results. Therefore, we should consider other forces, e.g., the capillary

forces, which may have a strong effect on the obtained results. Viscous forces should also be considered for the polymer samples. These forces result in energy dissipation. The capillary forces show hysteretic behavior. For these reasons, the analytical analysis may not be done. The numerical approach, on the other hand, can be very time-consuming since there will be many sample parameters that must be included in the model. Hence, at this point it is not possible to explain the contrast observed in the above experiments in a simple manner.

Nevertheless, we can comment on the obtained experimental results by making a comparison between them. Let us first consider the heterogeneous polymer samples. The determination of the surface morphology and mechanical/chemical heterogeneity of the polymer films have been addressed widely in the literature [16, 111–119]. One can obtain the surface structure of the heterogeneous polymers easily by conventional tapping-mode imaging. On the other hand, the determination of the regions corresponding to the different polymers may not be easily done by using the phase images. For this reason, additional measurements, like the force curve, contact angle, are required [114,116,120]. In our conventional tapping-mode experiments, the phase is found to be dominated by the feedback error signal. In enhanced harmonic imaging experiments, on the other hand, we found that the regions of the higher third harmonic amplitude correspond to the lower surface height regions. The results of 80:20 PS/PI blend show that the third harmonic does not change too much and its amplitude is around 0.27 nm. Since this mixture contains a mass fraction of PS of 80%, one can infer that the sample characteristics are mostly dominated by the properties of PS. Then, for the other polymer samples we argue that the regions of PS should have a third harmonic amplitude close to 0.27 nm by assuming that the properties of polymers remain unchanged in the mixtures. Note that we used the same operating parameters for the polymer samples. The conclusion of our argument is that the lower regions in the topography images correspond to polystyrene and the higher regions correspond to polyisoprene. Note that we were able to come up with this statement by ignoring the presence of PI in the 80:20 PS/PI blend. A more healthy conclusion can be drawn by finding the third harmonic response for the samples containing 100% of PS and 100% of PI.

Considering the photoresist on GaAs test sample, the third harmonic amplitude on GaAs region is found to be larger. The GaAs is much stiffer than the photoresist, but we think that the image contrast does not come from the stiffness difference because of the reasons explained above.

Chapter 7

Conclusions

In this dissertation, we discussed how the higher harmonics created in tapping-mode atomic force microscopy can be utilized to characterize the materials' mechanical properties at the nanoscale.

We found analytically that the higher harmonics increase monotonically for a range of sample stiffness in the case of a purely elastic interaction. Each harmonic gives an optimum response in a different region of sample compliance for the same operating parameter set. The amplitudes of the higher harmonics saturate for increasing sample stiffness. There is a lower limit of sample elasticity in which the tip stays in contact with the sample less than a half of its oscillation period. These two factors constrain the measurements in a limited region. The operating region can be adjusted by a suitable selection of cantilever stiffness.

Conventionally, the cantilever is oscillated at its fundamental resonant frequency, and the high Q-factor damps the amplitudes of the higher harmonics to negligible levels, unless the higher flexural eigenmodes are coincident with those harmonics. In order to increase the signal-to-noise ratio of the harmonic measurements we proposed a new method which can be applied easily to the commercial tapping-mode imaging setups by an additional lock-in amplifier. In this method, the most sensitive portion of the cantilever transfer function is utilized for the detection of harmonic amplitudes.

To test our method, we performed numerical simulations. The simulation results showed that the higher harmonics can be enhanced significantly by the proposed method. We found that the analytical solution is valid only for low harmonic distortion case. A nonmonotonic and chaotic behaviors were observed in the case of high harmonic distortion. These behaviors are observed since the enhanced higher harmonic and the interaction force depend on each other. To eliminate these problems we modified our method by slightly changing the driving frequency. For the modified method, the harmonic amplitudes are found to be varying monotonically in a region where the contact time is less than a half of the oscillation period. In this region, the lateral forces are reduced significantly and therefore harmonic imaging offers a higher image resolution compared to the previously developed surface characterization methods that require a static tip-sample contact.

We carried out several experiments for the proposed method and compared the results to the results of conventional tapping-mode experiments. We obtained very high signal-to-noise ratios for the third harmonic measurements. The results of the square-patterned test samples pointed out that the amplitude of enhanced third harmonic changes if there is a material difference on the sample surface. If the material uniformity does not change through the surface then the amplitude of enhanced third harmonic is found to be constant. We investigated the heterogeneity of blended films of polystyrene (PS) and polyisoprene (PI) and polystyrene-*block*-polyisoprene-*block*-polystyrene (SIS) copolymer on silicon substrates. The surface morphologies obtained with both methods are found to be very similar. The phase signal in the conventional operation was found to be dependent mostly on the error signal. The enhanced third harmonic, on the other hand, clearly differentiated the regions of PS and PI. Hence, one can utilize the the enhanced harmonic imaging technique to map mechanically heterogeneous regions in multicomponent polymer systems. We were not able to interpret the contrast obtained in the third harmonic images. However, we gained some idea about the composition of the features observed in topography and third harmonic images by comparing the results of different experiments. Experimental results also showed that the enhanced harmonic signal depends strongly on the small

features in the topography. Therefore the enhanced harmonic imaging could be very effective in the analysis of surface roughness.

In the light of analytical, numerical, and experimental findings, we conclude that the enhanced higher harmonic imaging has a great potential in nanoscale imaging and it can be utilized effectively in nanomaterial research.

A possible future research direction could be the reconstruction of the tip-sample force from the measurement of several enhanced higher harmonics. In such a way, the quantitative analysis of surface forces and sample viscoelastic properties can be done. But, this may not be suitable for imaging applications since we are required to measure both amplitude and phase of enough number of higher harmonics.

Bibliography

[1] G. Binning, C. F. Quate, and C. Gerber, “Atomic force microscope,” *Phys. Rev. Lett.*, vol. 56, p. 930, 1986.

[2] S. A. C. Gould, B. Drake, C. B. Prater, A. L. Weisenhorn, S. Manne, H. G. Hansma, P. K. Hansma, J. Massie, M. Longmire, V. Elings, B. D. Northern, B. Mukergee, C. M. Peterson, W. Stoeckenius, T. R. Albrecht, and C. F. Quate, “From atoms to integrated circuit chips, blood cells, and bacteria with the atomic force microscope,” *J. Vac. Sci. Technol. A*, vol. 8, p. 369, 1990.

[3] A. L. Weisenhorn, J. E. M. Dougall, S. A. C. Gould, S. D. Cox, W. S. Wise, J. Massie, P. Maivald, V. B. Elings, G. D. Stucky, and P. K. Hansma, “Imaging and manipulating molecules on a zeolite surface with an atomic force microscope,” *Science*, vol. 247, p. 1330, 1990.

[4] S. Manne, H. J. Butt, S. A. C. Gould, and P. K. Hansma, “Imaging metal atoms in air and water using the atomic force microscope,” *Appl. Phys. Lett.*, vol. 56, p. 1758, 1990.

[5] D. Fotiadis, S. Scheuring, S. A. Muller, A. Engel, and D. J. Muller, “Imaging and manipulation of biological structures with the afm,” *Micron*, vol. 33, p. 385, 2002.

[6] N. Oyabu, O. Custance, I. Yi, Y. Sugawara, and S. Morita, “Mechanical vertical manipulation of selected single atoms by soft nanoindentation using near contact atomic force microscopy,” *Phys. Rev. Lett.*, vol. 90, p. 176102, 2003.

[7] R. Garcia and R. Perez, "Dynamic atomic force microscopy methods," *Surf. Sci. Rep.*, vol. 47, p. 197, 2002.

[8] F. J. Giessibl, "Advances in atomic force microscopy," *Rev. Mod. Phys.*, vol. 75, p. 949, 2003.

[9] K. D. Jandt, "Atomic force microscopy of biomaterials surfaces and interfaces," *Surf. Sci.*, vol. 491, p. 303, 2001.

[10] N. Ahmed, D. F. Nino, and V. T. Moy, "Measurement of solution viscosity by atomic force microscopy," *Rev. Sci. Instrum.*, vol. 72, p. 2731, 2001.

[11] S. Cuenot, C. Fretigny, S. D. Champagne, and B. Nysten, "Measurement of elastic modulus of nanotubes by resonant contact atomic force microscopy," *J. Appl. Phys.*, vol. 93, p. 5650, 2003.

[12] J. Tamayo, "Structure of human chromosomes studied by atomic force microscopy," *J. Struct. Biol.*, vol. 141, p. 189, 2003.

[13] K. B. Crozier, G. G. Yaralioglu, F. L. Degertekin, J. D. Adams, S. C. Minne, and C. F. Quate, "Thin film characterization by atomic force microscopy at ultrasonic frequencies," *Appl. Phys. Lett.*, vol. 76, p. 1950, 2000.

[14] D. L. Malotky and M. K. Chaudhury, "Investigation of capillary forces using atomic force microscopy," *Langmuir*, vol. 17, p. 7823, 2001.

[15] H. X. You, J. M. Lau, S. Zhang, and L. Yu, "Atomic force microscopy imaging of living cells: A preliminary study of the disruptive effect of the cantilever tip on cell morphology," *Ultramicroscopy*, vol. 82, p. 297, 2000.

[16] D. Raghavan, M. VanLandingham, X. Gu, and T. Nguyen, "Characterization of heterogeneous regions in polymer systems using tapping mode and force mode atomic force microscopy," *Langmuir*, vol. 16, p. 9448, 2000.

[17] H. Sugimura, T. Hanji, K. Hayashi, and O. Takai, "Surface modification of an organosilane self-assembled monolayer on silicon substrates using atomic force microscopy: Scanning probe electrochemistry toward nanolithography," *Ultramicroscopy*, vol. 91, p. 221, 2002.

[18] P. Vettiger, J. Brugger, M. Despont, U. Drechsler, U. Durig, W. Haberle, M. Lutwyche, H. Rothuizen, R. Stutz, R. Widmer, and G. Binnig, “Ultra-high density, high-data-rate nems-based afm data storage system,” *Microelectronic Engineering*, vol. 46, p. 11, 1999.

[19] F. Oulevey, G. Gremaud, A. Semoroz, A. J. Kulik, N. A. Burnham, E. Dupas, and D. Gourdon, “Local mechanical spectroscopy with nanometer-scale lateral resolution,” *Rev. Sci. Instrum.*, vol. 69, p. 2085, 1998.

[20] T. R. Albrecht, S. Akamine, T. E. Carver, and C. F. Quate, “Microfabrication of cantilever styli for the atomic force microscope,” *J. Vac. Sci. Technol. A*, vol. 8, p. 3386, 1990.

[21] G. Meyer and N. M. Amer, “Novel optical approach to atomic force microscopy,” *Appl. Phys. Lett.*, vol. 53, p. 1045, 1988.

[22] S. Alexander, L. Hellemans, O. Marti, J. Schneir, V. Elings, P. K. Hansma, M. Longmire, and J. Gurley, “An atomic-resolution atomic-force microscope implemented using an optical lever,” *J. Appl. Phys.*, vol. 65, p. 164, 1989.

[23] R. Erlandsson, G. M. McClelland, C. M. Mate, and S. Chiang, “Atomic force microscopy using optical interferometry,” *J. Vac. Sci. Technol. A*, vol. 6, p. 266, 1988.

[24] A. J. den Boef, “Scanning force microscopy using a simple low-noise interferometer,” *Appl. Phys. Lett.*, vol. 55, p. 439, 1989.

[25] M. Tortonese, R. C. Barrett, and C. F. Quate, “Atomic resolution with an atomic force microscope using piezoresistive detection,” *Appl. Phys. Lett.*, vol. 62, p. 834, 1993.

[26] P. Kielczynski, W. Pajewski, and M. Szalewski, “Piezoelectric sensors for investigations of microstructures,” *Sens. Actuators, A*, vol. 65, pp. 13–18, 1998.

[27] T. R. Albrecht and C. F. Quate, “Atomic resolution imaging of a nonconductor by atomic force microscopy,” *J. Appl. Phys.*, vol. 62, p. 2599, 1987.

[28] T. R. Albrecht and C. F. Quate, “Atomic resolution with the atomic force microscope on conductors and nonconductors,” *J. Vac. Sci. Technol. A*, vol. 6, p. 271, 1988.

[29] H. Kado, S. Yamamoto, K. Yokoyama, T. Tohda, and Y. Umetani, “Observation of contact holes by atomic force microscopy with a zno whisker tip,” *J. Appl. Phys.*, vol. 74, p. 4354, 1993.

[30] F. M. Herrero, P. J. de Pablo, R. F. Sanchez, J. Colchero, J. G. Herrero, and A. M. Baro, “Scanning force microscopy jumping and tapping modes in liquids,” *Appl. Phys. Lett.*, vol. 81, p. 2620, 2002.

[31] S. Hosaka, T. Morimoto, K. Kuroda, H. Kunitomo, T. Hiroki, T. Kitsukawa, S. Miwa, H. Yanagimoto, and K. Murayama, “Proposal for new atomic force microscopy (afm) imaging for a high aspect structure (digital probing mode afm),” *Microelectronic Engineering*, vol. 57-58, p. 651, 2001.

[32] Y. Martin, C. C. Williams, and H. K. Wickramasinghe, “Atomic force microscope-force mapping and profiling on a sub 100-å scale,” *J. Appl. Phys.*, vol. 61, p. 4723, 1987.

[33] F. J. Giessibl, “Atomic resolution of the silicon (111)-(7x7) surface by atomic force microscopy,” *Science*, vol. 267, p. 68, 1995.

[34] T. R. Albrecht, P. Grutter, D. Horne, and D. Rugar, “Frequency modulation detection using high-q cantilevers for enhanced force microscope sensitivity,” *J. Appl. Phys.*, vol. 69, p. 668, 1991.

[35] H. Ueyama, Y. Sugawara, and S. Morita, “Stable operation mode for dynamic noncontact atomic force microscopy,” *Appl. Phys. A: Mater. Sci. Process.*, vol. 66, p. S295, 1998.

[36] N. A. Burnham and R. J. Colton, “Measuring the nanomechanical properties and surface forces of materials using an atomic force microscope,” *J. Vac. Sci. Technol. A*, vol. 7, p. 2906, 1989.

[37] R. W. Stark, T. Drobek, M. Weth, J. Fricke, and W. M. Heckl, "Determination of elastic properties of single aerogel powder particles with the afm," *Ultramicroscopy*, vol. 75, p. 161, 1998.

[38] A. Vinckier and G. Semenza, "Measuring elasticity of biological materials by atomic force microscopy," *FEBS Lett.*, vol. 430, p. 12, 1998.

[39] A. Touhami, B. Nysten, and Y. F. Dufrene, "Nanoscale mapping of the elasticity of microbial cells by atomic force microscopy," *Langmuir*, vol. 19, p. 4539, 2003.

[40] T. R. Matzelle, G. Geuskens, and N. Kruse, "Elastic properties of poly(n-isopropylacrylamide) and poly(acrylamide) hydrogels studied by scanning force microscopy," *Macromolecules*, vol. 36, p. 2926, 2003.

[41] B. Du, O. K. C. Tsui, Q. Zhang, and T. He, "Study of elastic modulus and yield strength of polymer thin films using atomic force microscopy," *Langmuir*, vol. 17, p. 3286, 2001.

[42] C. Reynaud, F. Sommer, C. Quet, N. E. Bounia, and T. M. Duc, "Quantitative determination of young's modulus on a biphase polymer system using atomic force microscopy," *Surf. Interface Anal.*, vol. 30, p. 185, 2000.

[43] Y. Oishi, T. Umeda, M. Kuramori, and K. Suehiro, "Mechanical properties of a langmuir-blodgett film measured by atomic force microscopy," *Langmuir*, vol. 18, p. 945, 2002.

[44] P. Maivald, H. J. Butt, S. A. C. Gould, C. B. Prater, B. Drake, J. A. Gurley, V. B. Elings, and P. K. Hansma, "Using force modulation to image surface elasticities with the atomic force microscope," *Nanotechnology*, vol. 2, p. 103, 1991.

[45] W. Kiridena, V. Jain, P. K. Kuo, and G. Liu, "Nanometer-scale elasticity measurements on organic monolayers using scanning force microscopy," *Surf. Interface Anal.*, vol. 25, p. 383, 1997.

[46] U. Rabe, K. Janser, and W. Arnold, “Vibrations of free and surface-coupled atomic force microscope cantilevers: Theory and experiment,” *Rev. Sci. Instrum.*, vol. 67, p. 3281, 1996.

[47] K. Yamanaka and S. Nakano, “Ultrasonic atomic force microscope with overtone excitation of cantilever,” *Jpn. J. Appl. Phys.*, vol. 35, p. 3787, 1996.

[48] E. Kester, U. Rabe, L. Presmanes, P. Tailhades, and W. Arnold, “Measurement of young’s modulus of nanocrystalline ferrites with spinel structures by atomic force acoustic microscopy,” *J. Phys. Chem. Solids*, vol. 61, p. 1275, 2000.

[49] S. Amelio, A. V. Goldade, U. Rabe, V. Scherer, B. Bhushan, and W. Arnold, “Measurements of elastic properties of ultra-thin diamond-like carbon coatings using atomic force acoustic microscopy,” *Thin Solid Films*, vol. 392, p. 75, 2001.

[50] K. Yamanaka, T. Tsuji, A. Noguchi, T. Koike, and T. Mihara, “Nanoscale elasticity measurement with *in situ* tip shape estimation in atomic force microscopy,” *Rev. Sci. Instrum.*, vol. 71, p. 2403, 2000.

[51] A. R. Zeiser, E. Weilandt, S. Hild, and O. Marti, “The simultaneous measurement of elastic, electrostatic, and adhesive properties by scanning force microscopy: Pulsed-force mode operation,” *Meas. Sci. Technol.*, vol. 8, p. 1333, 1997.

[52] K. O. van der Werf, C. A. J. Putman, B. G. de Grooth, and J. Greve, “Adhesion force imaging in air and liquid by adhesion mode atomic force microscopy,” *Appl. Phys. Lett.*, vol. 65, p. 1195, 1994.

[53] X. Chen, M. C. Davies, C. J. Roberts, S. J. B. Tendler, and P. M. Williams, “Hydrodynamic damping of tip oscillation in pulsed-force atomic force microscopy,” *Appl. Phys. Lett.*, vol. 77, p. 3462, 2000.

[54] B. Gotsmann, B. Anczykowski, C. Seidel, and H. Fuchs, “Determination of tip-sample interaction forces from measured dynamic force spectroscopy curves,” *Appl. Surf. Sci.*, vol. 140, p. 314, 1999.

[55] B. Gotsmann, C. Seidel, B. Anczykowski, and H. Fuchs, "Conservative and dissipative tip-sample interaction forces probed with dynamic afm," *Phys. Rev. B*, vol. 60, p. 11051, 1999.

[56] H. Holscher, W. Allers, U. D. Schwarz, A. Schwarz, , and R. Wiesendanger, "Determination of tip-sample interaction potentials by dynamic force spectroscopy," *Phys. Rev. Lett.*, vol. 83, p. 4780, 1999.

[57] F. J. Giessibl, "A direct method to calculate tip-sample forces from frequency shifts in frequency-modulation atomic force microscopy," *Appl. Phys. Lett.*, vol. 78, p. 123, 2001.

[58] J. E. Sader and S. P. Jarvis, "Accurate formulas for interaction force and energy in frequency modulation force spectroscopy," *Appl. Phys. Lett.*, vol. 84, p. 1801, 2004.

[59] J. Tamayo and R. Garcia, "Relationship between phase shift and energy dissipation in tapping-mode scanning force microscopy," *Appl. Phys. Lett.*, vol. 73, p. 2926, 1998.

[60] J. P. Cleveland, B. Anczykowski, A. E. Schmid, and V. B. Elings, "Energy dissipation in tapping-mode atomic force microscopy," *Appl. Phys. Lett.*, vol. 72, p. 2613, 1998.

[61] B. Anczykowski, B. Gotsmann, H. Fuchs, J. P. Cleveland, and V. B. Elings, "How to measure energy dissipation in dynamic mode atomic force microscopy," *Appl. Surf. Sci.*, vol. 140, p. 376, 1999.

[62] X. Chen, C. J. Roberts, J. Zhang, M. C. Davies, and S. J. B. Tendler, "Phase contrast and attraction-repulsion transition in tapping mode atomic force microscopy," *Surf. Sci.*, vol. 519, p. L593, 2002.

[63] M. S. Marcus, R. W. Caprick, D. Y. Sasaki, and M. A. Eriksson, "Material anisotropy revealed by phase contrast in intermittent contact atomic force microscopy," *Phys. Rev. Lett.*, vol. 88, p. 226103, 2002.

[64] J. Tamayo and R. Garcia, "Deformation, contact time, and phase contrast in tapping mode scanning force microscopy," *Langmuir*, vol. 12, p. 4430, 1996.

[65] J. Tamayo and R. Garcia, "Effects of elastic and inelastic interactions on phase contrast images in tapping-mode scanning force microscopy," *Appl. Phys. Lett.*, vol. 71, p. 2394, 1997.

[66] R. W. Stark and W. M. Heckl, "Fourier transformed atomic force microscopy: Tapping mode atomic force microscopy beyond the hookian approximation," *Surf. Sci.*, vol. 457, p. 219, 2000.

[67] R. Hillenbrand, M. Stark, and R. Guckenberger, "Higher-harmonics generation in tapping-mode atomic-force microscopy: Insights into the tip-sample interaction," *Appl. Phys. Lett.*, vol. 76, p. 3478, 2000.

[68] M. Stark, R. W. Stark, W. M. Heckl, and R. Guckenberger, "Spectroscopy of the anharmonic cantilever oscillations in tapping-mode atomic-force microscopy," *Appl. Phys. Lett.*, vol. 77, p. 3293, 2000.

[69] O. Sahin and A. Atalar, "Simulation of higher harmonics generation in tapping-mode atomic force microscopy," *Appl. Phys. Lett.*, vol. 79, p. 4455, 2001.

[70] S. J. T. van Noort, O. H. Willemsen, K. O. van der Werf, B. G. de Grooth, and J. Greve, "Mapping electrostatic forces using higher harmonics tapping mode atomic force microscopy in liquid," *Langmuir*, vol. 15, p. 7101, 1999.

[71] U. Durig, "Interaction sensing in dynamic force microscopy," *New J. Phys.*, vol. 2, p. 5.1, 2000.

[72] T. R. Rodriguez and R. Garcia, "Compositional mapping of surfaces in atomic force microscopy by excitation of the second normal mode of the microcantilever," *Appl. Phys. Lett.*, vol. 84, p. 449, 2004.

[73] J. Tamayo, "Energy dissipation in tapping-mode scanning force microscopy with low quality factors," *Appl. Phys. Lett.*, vol. 75, p. 3569, 1999.

[74] T. R. Rodriguez and R. Garcia, “Tip motion in amplitude modulation (tapping-mode) atomic-force microscopy: Comparison between continuous and point-mass models,” *Appl. Phys. Lett.*, vol. 80, p. 1646, 2002.

[75] U. Rabe, J. Turner, and W. Arnold, “Analysis of the high-frequency response of atomic force microscope cantilevers,” *Appl. Phys. A: Mater. Sci. Process.*, vol. 66, p. S277, 1998.

[76] C. Argento and R. H. French, “Parametric tip model and force-distance relation for hamaker constant determination from atomic force microscopy,” *J. Appl. Phys.*, vol. 80, p. 6081, 1996.

[77] U. Hartmann, “van der waals interactions between sharp probes and flat sample surfaces,” *Phys. Rev. B*, vol. 43, p. 2404, 1991.

[78] R. Garcia and A. S. Paulo, “Dynamics of a vibrating tip near or in intermittent contact with a surface,” *Phys. Rev. B*, vol. 61, p. 13381, 2000.

[79] S. I. Lee, S. W. Howell, A. Raman, and R. Reifenberger, “Nonlinear dynamics of microcantilevers in tapping mode atomic force microscopy: A comparison between theory and experiment,” *Phys. Rev. B*, vol. 66, p. 115409, 2002.

[80] R. W. Stark, G. Schitter, M. Stark, R. Guckenberger, and A. Stemmer, “State-space model of freely vibrating and surface-coupled cantilever dynamics in atomic force microscopy,” *Phys. Rev. B*, vol. 69, p. 85412, 2004.

[81] W. N. Unertl, “Implications of contact mechanics models for mechanical properties measurements using scanning force microscopy,” *J. Vac. Sci. Technol. A*, vol. 17, p. 1779, 1999.

[82] N. A. Burnham, O. P. Behrend, F. Oulevey, G. Gremaud, P. J. Gallo, D. Gourdon, E. Dupas, A. J. Kulik, H. M. Pollock, and G. A. D. Briggs, “How does a tip tap?,” *Nanotechnology*, vol. 8, p. 67, 1997.

[83] L. Zitzler, S. Herminghaus, and F. Mugele, “Capillary forces in tapping mode atomic force microscopy,” *Phys. Rev. B*, vol. 66, p. 155436, 2002.

[84] I. M. Ward, *Mechanical properties of solid polymers.* John Wiley & Sons, 1983.

[85] F. Dubourg, S. Kopp-Marsaudon, P. Leclere, R. Lazzaroni, and J. P. Aime, "Experimental determination of the viscosity at the nanometer scale on a block copolymer with an oscillating nanotip," *Eur. Phys. J. E*, vol. 6, p. 387, 2001.

[86] M. Balantekin and A. Atalar, "Power dissipation analysis in tapping-mode atomic force microscopy," *Phys. Rev. B*, vol. 67, p. 193404, 2003.

[87] M. Balantekin and A. Atalar, "Simulations of switching vibrating cantilever in atomic force microscopy," *Appl. Surf. Sci.*, vol. 205, p. 86, 2003.

[88] M. Stark, R. W. Stark, W. M. Heckl, and R. Guckenberger, "Inverting dynamic force microscopy: From signals to time-resolved interaction forces," *Proc. Natl. Acad. Sci. U.S.A.*, vol. 99, p. 8473, 2002.

[89] A. S. Paulo and R. Garcia, "Amplitude, deformation and phase shift in amplitude modulation atomic force microscopy: a numerical study for compliant materials," *Surf. Sci.*, vol. 471, p. 71, 2001.

[90] R. W. Stark and W. M. Heckl, "Higher harmonics imaging in tapping-mode atomic-force microscopy," *Rev. Sci. Instrum.*, vol. 74, p. 5111, 2003.

[91] O. Sahin, G. Yaralioglu, R. Grow, S. F. Zappe, A. Atalar, C. F. Quate, and O. Solgaard, "High-resolution imaging of elastic properties using harmonic cantilevers," *Sens. Actuators, A*, vol. 114, p. 183, 2004.

[92] O. Sahin, C. F. Quate, O. Solgaard, and A. Atalar, "Resonant harmonic response in tapping-mode atomic force microscopy," *Phys. Rev. B*, vol. 69, p. 165416, 2004.

[93] O. Sahin and A. Atalar, "Analysis of tip-sample interaction in tapping-mode atomic force microscope using an electrical circuit simulator," *Appl. Phys. Lett.*, vol. 78, p. 2973, 2001.

[94] R. Hegger, H. Kantz, and T. Schreiber, "Practical implementation of nonlinear time series methods: The tisean package," *Chaos*, vol. 9, p. 413, 1999.

[95] M. Sano and Y. Sawada, "Measurement of the lyapunov spectrum from a chaotic time series," *Phys. Rev. Lett.*, vol. 55, p. 1082, 1985.

[96] J. P. Hunt and D. Sarid, "Kinetics of lossy grazing impact oscillators," *Appl. Phys. Lett.*, vol. 72, p. 2969, 1998.

[97] R. W. Stark, "Spectroscopy of higher harmonics in dynamic atomic force microscopy," *Nanotechnology*, vol. 15, p. 347, 2004.

[98] J. P. Spatz, S. Sheiko, M. Moller, R. G. Winkler, P. Reineker, and O. Marti, "Forces affecting the substrate in resonant tapping force microscopy," *Nanotechnology*, vol. 6, p. 40, 1995.

[99] H. Bielefeldt and F. J. Giessibl, "A simplified but intuitive analytical model for intermittent-contact-mode force microscopy based on hertzian mechanics," *Surf. Sci.*, vol. 440, p. L863, 1999.

[100] A. Mendez-Vilas, M. L. Gonzalez-Martin, and M. J. Nuevo, "Optical interference artifacts in contact atomic force microscopy images," *Ultramicroscopy*, vol. 92, p. 243, 2002.

[101] R. Kassies, K. O. van der Werf, M. L. Bennink, and C. Otto, "Removing interference and optical feedback artifacts in atomic force microscopy measurements by application of high frequency laser current modulation," *Rev. Sci. Instrum.*, vol. 75, p. 689, 2004.

[102] T. Sulchek, R. Hsieh, J. D. Adams, G. G. Yaralioglu, S. C. Minne, C. F. Quate, J. P. Cleveland, A. Atalar, and D. M. Adderton, "High-speed tapping mode imaging with active q control for atomic force microscopy," *Appl. Phys. Lett.*, vol. 76, p. 1473, 2000.

[103] H. Jinnai, Y. Nishikawa, R. J. Spontak, S. D. Smith, D. A. Agard, and T. Hashimoto, "Direct measurement of interfacial curvature distributions

in a bicontinuous block copolymer morphology," *Phys. Rev. Lett.*, vol. 84, p. 518, 2000.

[104] P. Simon, R. Adhikari, H. Lichte, G. H. Michler, and M. Langela, "Electron holography and afm studies on styrenic block copolymers and a high impact polystyrene," *J. Appl. Polym. Sci.*, vol. 96, p. 1573, 2004.

[105] C. D. Han, D. M. Baek, J. K. Kim, T. Hashimoto, and S. Okamoto, "Viscoelastic behavior of a homogeneous polystyrene-block-polyisoprene-block-polystyrene copolymer," *Macromolecules*, vol. 24, p. 5408, 1991.

[106] N. Sakamoto, T. Hashimoto, C. D. Han, D. Kim, and N. Y. Vaidya, "Order-order and order-disorder transitions in a polystyrene-block-polyisoprene-block-polystyrene copolymer," *Macromolecules*, vol. 30, p. 1621, 1997.

[107] K. C. Daoulas, D. N. Theodorou, A. Roos, and C. Creton, "Experimental and self-consistent-field theoretical study of styrene block copolymer self-adhesive materials," *Macromolecules*, vol. 37, p. 5093, 2004.

[108] J. Brandrup and E. H. Immergut, *Polymer Handbook*. John Wiley & Sons, 1989.

[109] U. Landman and W. D. Luedtke, "Small is different: energetic, structural, thermal, and mechanical properties of passivated nanocluster assemblies," *Faraday Discuss.*, vol. 125, p. 1, 2004.

[110] A. Kuhle, A. H. Sorensen, and J. Bohr, "Role of attractive forces in tapping tip force microscopy," *J. Appl. Phys.*, vol. 81, p. 6562, 1997.

[111] R. Viswanathan, J. Tian, and D. W. M. Marr, "Morphology characterization in multicomponent macromolecular systems using scanning probe phase microscopy," *Langmuir*, vol. 13, p. 1840, 1997.

[112] M. Boltau, S. Walheim, J. Mlynek, G. Krausch, and U. Steiner, "Surface-induced structure formation of polymer blends on patterned substrates," *Nature*, vol. 391, p. 877, 1998.

[113] S. N. Magonov, V. Elings, and V. S. Papkov, "Afm study of thermotropic structural transitions in poly(diethylsiloxane)," *Polymer*, vol. 38, p. 297, 1997.

[114] D. Raghavan, X. Gu, T. Nguyen, and M. VanLandingham, "Characterization of chemical heterogeneity in polymer systems using hydrolysis and tapping-mode atomic force microscopy," *J. Polym. Sci.: Part B: Polym. Phys.*, vol. 39, p. 1460, 2001.

[115] G. Bar, Y. Thomann, and M. H. Whangbo, "Characterization of the morphologies and nanostructures of blends of poly(styrene)-block-poly(ethene-co-but-1-ene)-block-poly(styrene) with isotactic and atactic polypropylenes by tapping-mode atomic force microscopy," *Langmuir*, vol. 14, p. 1219, 1998.

[116] D. Raghavan, X. Gu, T. Nguyen, M. VanLandingham, and A. Karim, "Mapping polymer heterogeneity using atomic force microscopy phase imaging and nanoscale indentation," *Macromolecules*, vol. 33, p. 2573, 2000.

[117] S. N. Magonov, J. Cleveland, V. Elings, D. Denley, and M. H. Whangbo, "Tapping-mode atomic force microscopy study of the near-surface composition of a styrene-butadiene-styrene triblock copolymer film," *Surf. Sci.*, vol. 389, p. 201, 1997.

[118] K. D. Veress, B. G. Nickel, and J. R. Dutcher, "Dispersion-driven morphology of mechanically confined polymer films," *Phys. Rev. Lett.*, vol. 82, p. 1486, 1999.

[119] S. N. Magonov, V. Elings, and M. H. Whangbo, "Phase imaging and stiffness in tapping-mode atomic force microscopy," *Surf. Sci.*, vol. 375, p. L385, 1997.

[120] G. Bar, Y. Thomann, R. Brandsch, H. J. Cantow, and M. H. Whangbo, "Factors affecting the height and phase images in tapping mode atomic force microscopy. study of phase-separated polymer blends of poly(ethene-co-styrene) and poly(2,6-dimethyl-1,4-phenylene oxide)," *Langmuir*, vol. 13, p. 3807, 1997.

[121] B. Rogers, D. York, N. Whisman, M. Jones, K. Murray, J. D. Adams, T. Sulchek, and S. C. Minne, "Tapping mode atomic force microscopy in liquid with an insulated piezoelectric microactuator," *Rev. Sci. Instrum.*, vol. 73, p. 3242, 2002.

[122] B. Rogers, L. Manning, T. Sulchek, and J. D. Adams, "Improving tapping mode atomic force microscopy with piezoelectric cantilevers," *Ultramicroscopy*, vol. 100, p. 267, 2004.

[123] J. L. Hutter and J. Bechhoefer, "Calibration of atomic-force microscope tips," *Rev. Sci. Instrum.*, vol. 64, p. 1868, 1993.

[124] H. J. Butt and M. Jaschke, "Calculation of thermal noise in atomic force microscopy," *Nanotechnology*, vol. 6, p. 1, 1995.

[125] R. W. Stark, T. Drobek, and W. M. Heckl, "Thermomechanical noise of a free v-shaped cantilever for atomic-force microscopy," *Ultramicroscopy*, vol. 86, p. 207, 2001.

[126] C. P. Green, H. Lioe, J. P. Cleveland, R. Proksch, P. Mulvaney, and J. E. Sader, "Normal and torsional spring constants of atomic force microscope cantilevers," *Rev. Sci. Instrum.*, vol. 75, p. 1988, 2004.

[127] J. P. Cleveland, S. Manne, D. Bocek, and P. K. Hansma, "A nondestructive method for determining the spring constant of cantilevers for scanning force microscopy," *Rev. Sci. Instrum.*, vol. 64, p. 403, 1993.

[128] J. E. Sader, J. W. M. Chon, and P. Mulvaney, "Calibration of rectangular atomic force microscope cantilevers," *Rev. Sci. Instrum.*, vol. 70, p. 3967, 1999.

[129] J. E. Sader, "Frequency response of cantilever beams immersed in viscous fluids with applications to the atomic force microscope," *J. Appl. Phys.*, vol. 84, p. 64, 1998.

[130] K. Y. Yasumura, T. D. Stowe, E. M. Chow, T. Pfafman, T. W. Kenny, B. C. Stipe, and D. Rugar, "Quality factors in micron- and submicron-thick cantilevers," *J. Microelectromech. Syst.*, vol. 9, p. 117, 2000.

Appendix A

Experimental Setup

The complete setup, the instruments used in the experiments and the AFM head are shown below.

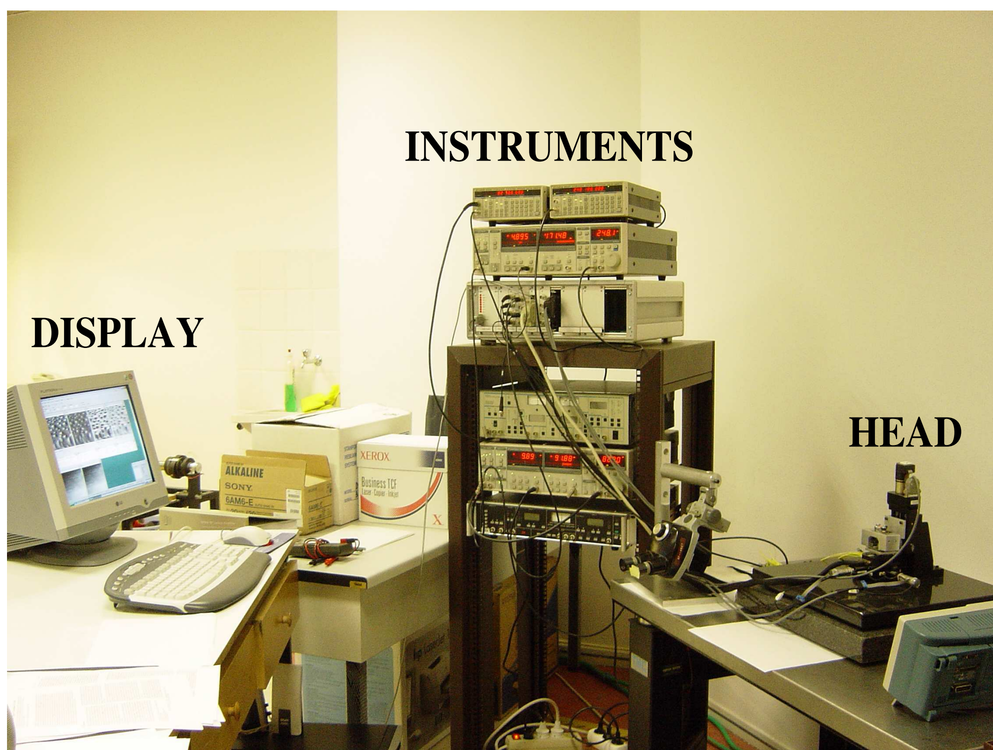

Figure A.1: The experimental setup.

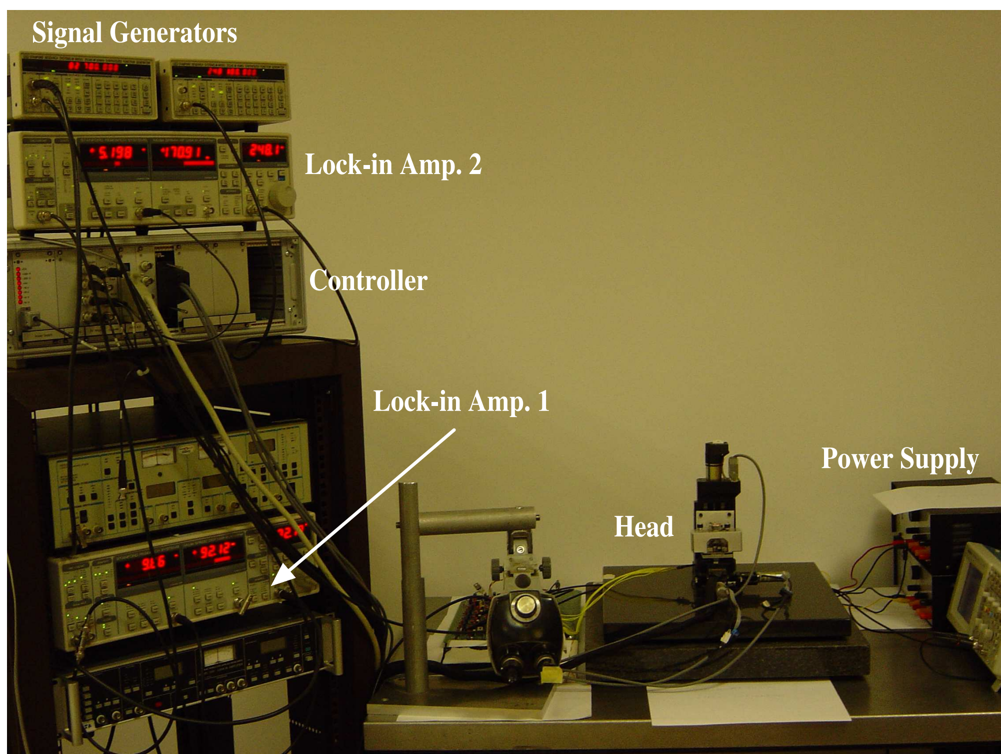

Figure A.2: Instruments in the setup.

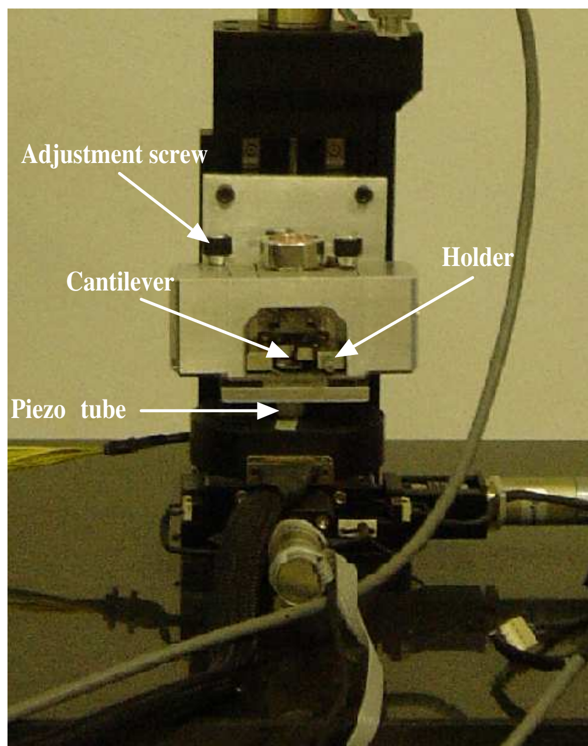

Figure A.3: Optical AFM head.

Appendix B

Cantilever Specifications

We used a single cantilever (Model No. MPA-11100, NanoDevices, Santa Barbara, CA) [also available from Veeco Instruments (Model No. DMASP)] throughout the experiments. This cantilever (see Fig. B.1) combines the functions of both sensor and actuator by using an integrated ZnO piezoelectric microactuator (yellow region). The actuator part is useful in that it eliminates the spurious resonances when vibrating the cantilever in liquid environment [121]. This cantilever is also used in self-sensing configuration which eliminates the laser and the photodetector and in high-speed imaging applications [122]. The nominal cantilever dimensions of the manufacturer and the ones obtained from our measurements are collected in Table B.1.

The spring constant of a cantilever can be determined by measuring the amplitude of thermal noise [123]. If an optical-lever method is employed in the detection system then one requires the knowledge of the shapes of the bending modes [124, 125]. We could not use this method because of two reasons. First, the frequency spectrum of the detector output is found to be flat. Second, the detector is not calibrated.

There are two other widely used spring constant determination methods [126]. These are the added mass method of Cleveland *et al.* [127] and the unloaded resonance technique of Sader *et al.* [128]. The former method requires an addition

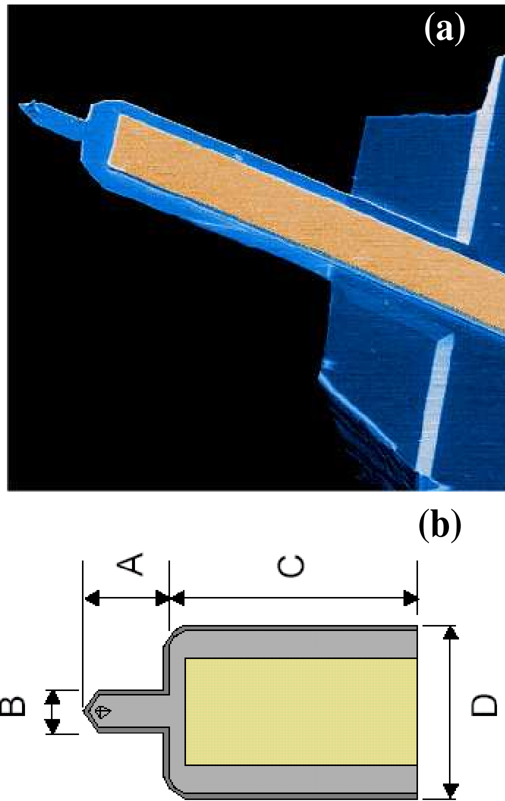

Figure B.1: (a) SEM micrograph of the cantilever. (b) Probe dimensions.

Table B.1: Cantilever specifications.

	Manufacturer's value	Measured value
Sensor length (A)	125 μm	105 μm
Sensor width (B)	55 μm	60 μm
Actuator length (C)	375 μm	380 μm
Actuator width (D)	250 μm	210 μm
Thickness	3-5 μm †	7 μm
Tip height	15-20 μm †	20 μm
Tip radius	$<$ 10 nm †	$\leq$100 nm
Fundamental resonance frequency	50 kHz	50.9 kHz
Operating resonance frequency	200 kHz	254.4 kHz
Spring constant	1-5 N/m	$\approx$ 3 N/m

† Obtained from Veeco Instruments.

of known masses onto the cantilever. The latter determines the spring constant from the measurement of the unloaded resonant frequency and quality factor of the flexural mode. The knowledge of plan view dimensions of the cantilever and properties of the fluid (air) are also required.

To determine the cantilever spring constant we utilized the unloaded resonance technique. If the quality factor is much larger than unity then the normal spring constant of a rectangular cantilever is given by [128]

$$k = 0.1906 \rho b^2 L Q {w_f}^2 {\Gamma_i}^f \ , \tag{B.1}$$

where ρ is the density of the air, b and L are the width and length of the cantilever, Q is the quality factor, w_f is the resonant frequency and ${\Gamma_i}^f$ is the imaginary component of the hydrodynamic function Γ given in Ref. [129]. Γ depends on the Reynolds number Re, which is equal to $\rho b^2 {w_f}^2/(4\eta)$, where η is the viscosity of the surrounding medium. The real and imaginary components of Γ as a function of Re are plotted in Ref. [128]. The density and viscosity of air are $\rho = 1.18$ kgm^{-3} and $\eta = 1.86 \times 10^{-5}$ kgm^{-1}s^{-1}, respectively.

Note that our cantilever is not rectangular. One can find the spring constant of a non-rectangular cantilever if the cantilever chip contains multiple cantilevers and at least one of these cantilevers has a rectangular geometry [126].

Therefore we simplify the problem as follows. Our cantilever has two resonances at 50.9 kHz and at 254.4 kHz. The quality factors of these resonances are found to be 40 and 420, respectively. We think that the first resonance is due to the larger actuator part and the second resonance is due the smaller sensor part. We found two spring constants for each resonance by neglecting their effects on each other. Namely, we considered one small cantilever (sensor region) attached to a bigger one (actuator region). Then the spring constants for these two cantilevers (although not exactly rectangular in shape) are estimated to be ~ 3 N/m (for the first resonance) and ~ 28 N/m (for the second resonance).

Note that the estimation is very crude. Since the spring constant determines the force applied to the surface, it should be determined more precisely if required.

Appendix C

Detector Calibration

The detector is calibrated generally by doing an amplitude versus distance measurement on a very stiff sample. By using the slope of the obtained curve, one can convert the oscillation voltage into meter by noting the fact that the tip does not indent too much into the sample in such a case. However, our setup is not suitable for this measurement.

One can also calibrate the detector by equating the theoretical and measurement values of the thermomechanical fluctuation of the cantilever if the spring constant is known. The mean square vibration amplitude $< z^2 >$ associated with a mode of oscillation is given by

$$\frac{1}{2}k < z^2 >= \frac{1}{2}k_B T \ , \tag{C.1}$$

where k_B is the Boltzmann constant and T is the temperature of the surrounding medium. $< z^2 >$ is obtained by taking the integral of the multiplication of the force noise spectral density S_F and the square of the magnitude of mechanical transfer function $H(w)$ in a given bandwidth B. By assuming a white noise spectrum, S_F is found to be $4kk_BT/(w_fQ)$ [130]. If we choose the measurement bandwidth much smaller than the bandwidth of the cantilever resonance, then $|H(w)|$ can be considered as a constant (Q/k) at the resonance. Therefore the

rms value of vibration amplitude due to thermomechanical noise is given by

$$\sqrt{< z^2 >} = \sqrt{\frac{4Qk_BTB}{w_f k}} \ . \tag{C.2}$$

Recall that we were not able to measure the thermal noise of our cantilever. For this reason, we measured the noise spectrum of another cantilever (calibration cantilever) which has a lower spring constant to find the driving force of the tapping piezo. Afterwards, this driving force is used to make a calibration. This indirect approach can be stated as follows: First, we measured the thermomechanical noise of the calibration cantilever (Model DNP-S, Veeco Instruments, Santa Barbara, CA) at its resonance frequency (45.6 kHz) by a spectrum analyzer (HP 4195A) in a resolution bandwidth of 30 Hz. The average of 10 measurements is found to be 12.6 μV_{rms}, where the noise floor is 2 μV_{rms}. This value is multiplied by 100 (since there is a 5 kΩ resistor at the output of the preamplifier) to find the noise at the output of the preamplifier. By using Eq. (C.2) and the spring constant ($k_{clb} = 0.58$ N/m, nominal value of the manufacturer) and quality factor ($Q_{clb} = 45$) of the calibration cantilever we obtained a thermal noise of ≈ 12 pm. We also excited both of the cantilevers at the resonance frequency of calibration cantilever. For a 0.3 V_{p-p} excitation voltage, we obtained responses of 1.7 mV_{rms} and 390 mV_{rms} for the measurement and calibration cantilevers, respectively. We divided 390 mV_{rms} by the noise at the output of preamplifier and multiplied the resultant value with ≈ 12 pm to find the oscillation amplitude A_{clb} in meters. A_{clb} is multiplied by k_{clb}/Q_{clb} to find the corresponding driving force F_d. F_d is multiplied by the transfer gain of the measurement cantilever (≈ 1.7) at 45.6 kHz to find the oscillation amplitude of the measurement cantilever in meters. Here, we assumed that the same driving force is applied to both cantilevers. We note that this is not a good assumption since the driving force depends on the interface between the tapping piezo and cantilever substrate. We also note that the substrates of the cantilevers are not the same. Finally, the obtained oscillation amplitude of the measurement cantilever is divided by 1.7 mV_{rms}. Hence we end up with a calibration constant of ~ 47 pm/mV for the measurement cantilever.

Once again, we should point out that the applied procedure gives just a very rough estimate (order of the magnitude at least). We note that the obtained

signal-to-noise ratios are independent of this calibration.